

**WL-TR-96-4117**

**HIGH-RESOLUTION THREE-DIMENSIONAL  
COMPUTED TOMOGRAPHY**



**PERCEPTICS CORPORATION  
725 PELLISSIPPI PARKWAY  
KNOXVILLE, TN 37922**

**OCTOBER 1996**

**FINAL REPORT FOR PERIOD JUNE 1993 - DECEMBER 1995**

**APPROVED FOR PUBLIC RELEASE; DISTRIBUTION IS UNLIMITED.**

*UNCLASSIFIED*

**MATERIALS DIRECTORATE  
WRIGHT LABORATORY  
AIR FORCE MATERIEL COMMAND  
WRIGHT-PATTERSON AIR FORCE BASE, OHIO 45433-7734**

**19970903 130**

## NOTICE

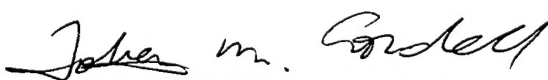
WHEN GOVERNMENT DRAWINGS, SPECIFICATIONS, OR OTHER DATA ARE USED FOR ANY PURPOSE OTHER THAN IN CONNECTION WITH A DEFINITELY GOVERNMENT-RELATED PROCUREMENT, THE UNITED STATES GOVERNMENT INCURS NO RESPONSIBILITY OR ANY OBLIGATION WHATSOEVER. THE FACT THAT THE GOVERNMENT MAY HAVE FORMULATED OR IN ANY WAY SUPPLIED THE SAID DRAWINGS, SPECIFICATIONS, OR OTHER DATA, IS NOT TO BE REGARDED BY IMPLICATION OR OTHERWISE IN ANY MANNER CONSTRUED, AS LICENSING THE HOLDER OR ANY OTHER PERSON OR CORPORATION, OR AS CONVEYING ANY RIGHTS OR PERMISSION TO MANUFACTURE, USE, OR SELL ANY PATENTED INVENTION THAT MAY IN ANY WAY BE RELATED THERETO.

THIS REPORT IS RELEASABLE TO THE NATIONAL TECHNICAL INFORMATION SERVICE (NTIS). AT NTIS, IT WILL BE AVAILABLE TO THE GENERAL PUBLIC, INCLUDING FOREIGN NATIONS.

THIS TECHNICAL REPORT HAS BEEN REVIEWED AND IS APPROVED FOR PUBLICATION.



CHARLES F. BUYNAK, Project Engineer  
Nondestructive Evaluation Branch  
Metals and Ceramics Division



TOBEY M. CORDELL, Chief  
Nondestructive Evaluation Branch  
Metals and Ceramics Division



WALTER M. GRIFFITH, Actg Chief  
Metals, Ceramics & Nondestructive Evaluation Division  
Materials Directorate

IF YOUR ADDRESS HAS CHANGED, IF YOU WISH TO BE REMOVED FROM OUR MAILING LIST, OR IF THE ADDRESSEE IS NO LONGER EMPLOYED BY YOUR ORGANIZATION, PLEASE NOTIFY, WL/MLLP, WRIGHT-PATTERSON AFB OH 45433-7817 TO HELP US MAINTAIN A CURRENT MAILING LIST.

COPIES OF THIS REPORT SHOULD NOT BE RETURNED UNLESS RETURN IS REQUIRED BY SECURITY CONSIDERATIONS, CONTRACTUAL OBLIGATIONS, OR NOTICE ON A SPECIFIC DOCUMENT.

# REPORT DOCUMENTATION PAGE

FORM APPROVED  
OMB NO. 0704-0188

Public reporting burden for this collection of information is estimated to average 1 hour per response, including the time for reviewing instructions, searching existing data sources, gathering and maintaining the data needed, and completing and reviewing the collection of information. Send comments regarding this burden estimate or any other aspect of this collection of information, including suggestions for reducing this burden, to Washington Headquarters Services, Directorate for Information Operations and Reports, 1215 Jefferson Davis Highway, Suite 1204, Arlington, VA 22202-4302 and to the Office of Management and Budget, Paperwork Reduction Project (0704-0188), Washington, DC 20503.

1. AGENCY USE ONLY (Leave blank)

2. REPORT DATE  
October 1996

3. REPORT TYPE AND DATES COVERED  
Final Report June 1993 - December 1995

4. TITLE AND SUBTITLE

High-Resolution Three-Dimensional Computed Tomography

5. FUNDING NUMBERS

F33615-93-C-5327  
PE 63112F  
PR 2865  
TA 07  
WU 10

6. AUTHOR(S)

Perceptics Corporation

7. PERFORMING ORGANIZATION NAMES(S) AND ADDRESS(ES)

Perceptics Corporation  
725 Pellissippi Parkway  
Knoxville TN 37922

8. PERFORMING ORGANIZATION  
REPORT NUMBER

9. SPONSORING/MONITORING AGENCY NAMES(ES) AND ADDRESS(ES)

Materials Directorate  
Wright Laboratory  
Air Force Materiel Command  
Wright-Patterson AFB OH 45433-7734  
POC: Charles Buynak, WL/MLLP, 937-255-9807

10. SPONSORING/MONITOR-  
ING AGENCY REPORT NUMBER

WL-TR-96-4117

11. SUPPLEMENTARY NOTES

12a. DISTRIBUTION/AVAILABILITY STATEMENT

Approved for public release; distribution is unlimited

12b. DISTRIBUTION CODE

13. ABSTRACT (Maximum 200 words)

In the High-Resolution Three-Dimensional Computed Tomography (HR3DCT) program, a team comprised of Perceptics, Skiametrics, Alliant Techsystems, Lockheed Martin, and Tufts University demonstrated that HR3DCT is a viable and valuable technology for large (SRM) bondline inspection. The approach used a specially built test apparatus, the HR3DCT breadboard, to test underlying assumptions and to apply the HR3DCT algorithm to a variety of test objects. At the completion of this effort, HR3DCT's few limitations and its remarkable potential were better-understood. The bondlines of a Titan SRM segment and a simulated Titan IV segment (both three meters in diameter), a 1.8-m diameter strategic SRM, and a Minuteman third-stage dome. In each case, the reconstructed data exhibited sensitivity comparable to conventional (CT). Bondline resolution was superior to conventional CT. Reconstructions were three-dimensional, facilitating immediate apprehension of bondline condition.

14. SUBJECT TERMS

aircraft component, solid rocket motor (SRM), nondestructive inspection, nondestructive evaluation, computed tomography, bondline inspection

15. NUMBER OF PAGES

83

16. PRICE CODE

17. SECURITY  
CLASSIFICATION OF REPORT

UNCLASSIFIED

18. SECURITY CLASSIFICATION  
OF THIS PAGE

UNCLASSIFIED

19. SECURITY  
CLASSIFICATION OF ABSTRACT

UNCLASSIFIED

20. LIMITATION OF ABSTRACT

SAR

NSN 7540-01-280-5500

COMPUTER GENERATED

STANDARD FORM 298 (Rev. 2-89)  
Prescribed by ANSI Std. Z39-18  
298-102

## TABLE OF CONTENTS

|   |           |
|---|-----------|
| <b>1. EXECUTIVE SUMMARY</b>   | <b>1</b>  |
| <b>2. INTRODUCTION</b>  | <b>4</b>  |
| 2.1 Report organization   | 4         |
| 2.2 Program objectives  | 5         |
| <b>3. BACKGROUND</b>  | <b>7</b>  |
| 3.1 Why bondline inspection demands a new NDE tool                              | 7         |
| 3.2 The CT-based solution   | 11        |
| 3.3 Prior results   | 16        |
| <b>4. PROGRAM APPROACH</b>  | <b>21</b> |
| 4.1 Task 1 Preliminary assessment   | 21        |
| 4.2 Task 2 Specify, design, build and validate a breadboard system              | 23        |
| 4.3 Task 3 Analyze HR3DCT performance based on production-scale scan results    | 24        |
| 4.4 Facilities and equipment  | 25        |
| 4.5 Test samples  | 32        |
| <b>5. EQUIPMENT CHARACTERIZATION RESULTS</b>                                    | <b>34</b> |
| 5.1 Imaging issues  | 34        |
| 5.2 Radiometric issues  | 39        |
| 5.3 Suitability of test objects   | 42        |
| 5.4 Acquisition   | 43        |
| 5.5 Preprocessing computations  | 43        |
| <b>6. HR3DCT RESULTS</b>  | <b>46</b> |
| 6.1 C4 phantom  | 46        |
| 6.2 Graphite Titan  | 47        |
| 6.3 Steel-case Titan phantoms   | 48        |
| 6.4 Overall conclusions   | 52        |
| 6.5 Cost/benefit analysis   | 54        |
| <b>7. ALTERNATIVE RECONSTRUCTION ALGORITHMS AND RESULTS</b>                     | <b>57</b> |
| 7.1 Overview.   | 58        |
| 7.2 Analysis.   | 59        |
| <b>8. APPLICATION GUIDE</b>   | <b>65</b> |
| 8.1 Determining whether an application is feasible                              | 65        |
| 8.2 Equipment and software requirements   | 67        |
| 8.3 Application optimization  | 71        |
| 8.4 Projecting performance  | 76        |
| <b>9. CONCEPTUAL DESIGN EXAMPLES</b>  | <b>79</b> |
| 9.1 The generic HR3DCT system   | 79        |
| 9.2 A dedicated HR3DCT system for a 12" diameter sample                         | 84        |
| 9.3 A seldom used HR3DCT system for inspecting a very large solid rocket motor. | 85        |



## LIST OF FIGURES

|  |    |
|--|----|
| Figure 1. Titan tangent X-ray transmission is too small for practical X-ray sources..... | 9  |
| Figure 2. Hard physical limitations result in CT tradeoffs.....                          | 10 |
| Figure 3. Signal fraction due to small separations. ....                                 | 12 |
| Figure 4. Simple limited-angle CT diagram.....   | 14 |
| Figure 5. PACT experiment equipment and phantom.....                                     | 17 |
| Figure 6. PACT BAM-0 reconstruction.....   | 18 |
| Figure 7. PACT Lucite phantom reconstruction from synthetic data.....                    | 19 |
| Figure 8. The RTIS platform.....   | 25 |
| Figure 9. The program's Lockheed SSXI imager and Isocon platforms.....                   | 26 |
| Figure 10. The Lockheed SSXI imager's LKH-5 X-ray converter efficiency.....              | 28 |
| Figure 11. The LKH-5 X-ray converter resolution.....                                     | 28 |
| Figure 12. General radiographic layout used in experiments.....                          | 29 |
| Figure 13. Artifact sources in the HR3DCT imaging chain.....                             | 31 |
| Figure 14. Test articles.....  | 33 |
| Figure 15. A bar pattern device used to measure spatial resolution.....                  | 36 |
| Figure 16. Stepped absorbers used to measure composite linearity.....                    | 37 |
| Figure 17. The SSXI imager as set up for various experiments.....                        | 39 |
| Figure 18. One of the 3-m diameter steel phantoms. ....                                  | 43 |
| Figure 19. Polar sampling of transaxial section of C4 phantom reconstruction .....       | 46 |
| Figure 20. Composite Titan reconstruction.....   | 48 |
| Figure 21. Constant-radius section of steel Titan reconstruction.....                    | 49 |
| Figure 22. Minuteman dome reconstruction. ....   | 50 |
| Figure 23. Reconstructions through nozzle throat.....                                    | 51 |
| Figure 24. ERA reconstructions. ....   | 60 |
| Figure 25. ERA reconstructions. ....   | 62 |

## LIST OF TABLES

|   |    |
|---|----|
| Table 1 Strengths and weaknesses of ultrasonic and radiographic SRM NDE.....          | 8  |
| Table 2 Candidate HR3DCT reconstruction approaches. ....                              | 14 |
| Table 3 Characteristics of the program's test platform imagers.....                   | 27 |
| Table 4 Approach to design of radiographic elements.....                              | 30 |
| Table 5 Assessment of fundamental RTR imager limitations.....                         | 34 |
| Table 6 Assessment of reversible RTR imager limitations.....                          | 35 |
| Table 7 Dynamic range of a 1.5-m steel SRM projection.....                            | 36 |
| Table 8 Determination of fixed radiographic parameters.....                           | 40 |
| Table 9 Approach to optimization of radiographic configuration.....                   | 40 |
| Table 10 Imaging chain artifacts, observations and approaches.....                    | 44 |
| Table 11 Validation results in terms of standard measures.....                        | 53 |
| Table 12 Relationships among tunable parameters and performance characteristics. .... | 72 |
| Table 13 Generic HR3DCT system requirements.....                                      | 79 |
| Table 14 Generic HR3DCT system performance parameters.....                            | 82 |

## ABBREVIATIONS

|        |   |
|--------|---|
| AFB    | Air Force Base  |
| ART    | Algebraic Reconstruction Technique                    |
| AVS    | Advanced Visualization Systems (AVS is a trademark)   |
| COTS   | Commercial Off-The-Shelf                              |
| CT     | Computed Tomography                                   |
| EFIRT  | Extended Field Reconstruction Technique               |
| ERA    | Exterior Reconstruction Algorithm                     |
| HERTIS | High-Energy Real-Time Imaging System                  |
| HR3DCT | High-Resolution Three-Dimensional Computed Tomography |
| HVL    | Half Value Layers                                     |
| NDE    | Non-Destructive Evaluation                            |
| PACT   | Partial Angle Computed Tomography                     |
| RTIS   | Real Time Inspection System                           |
| RTR    | Real-Time Radiography                                 |
| SDD    | Source-to-Detector Distance                           |
| SIT    | Silicon Intensified Target                            |
| SOD    | Source-to-Object Distance                             |
| SPIP   | Solid Propulsion Integrity Program                    |
| SRM    | Solid Rocket Motor                                    |
| SRMU   | Solid Rocket Motor Upgrade                            |
| SSXI   | Solid State X-ray Imager                              |
| UIS    | Ultrasonic Inspection System                          |

## FOREWORD

This final report was prepared by Perceptics Corporation, Sandy, Utah, for the Wright Laboratory / Materials Directorate. It documents work performed under Air Force Contract F33615-93-C-5327, "High-Resolution Three-Dimensional Computed Tomography (HR3DCT)," during the period from August 1993 through February 1996. The focus of the program was to demonstrate the value and viability of HR3DCT technology in large solid rocket motor (SRM) non-destructive evaluation (NDE) applications.

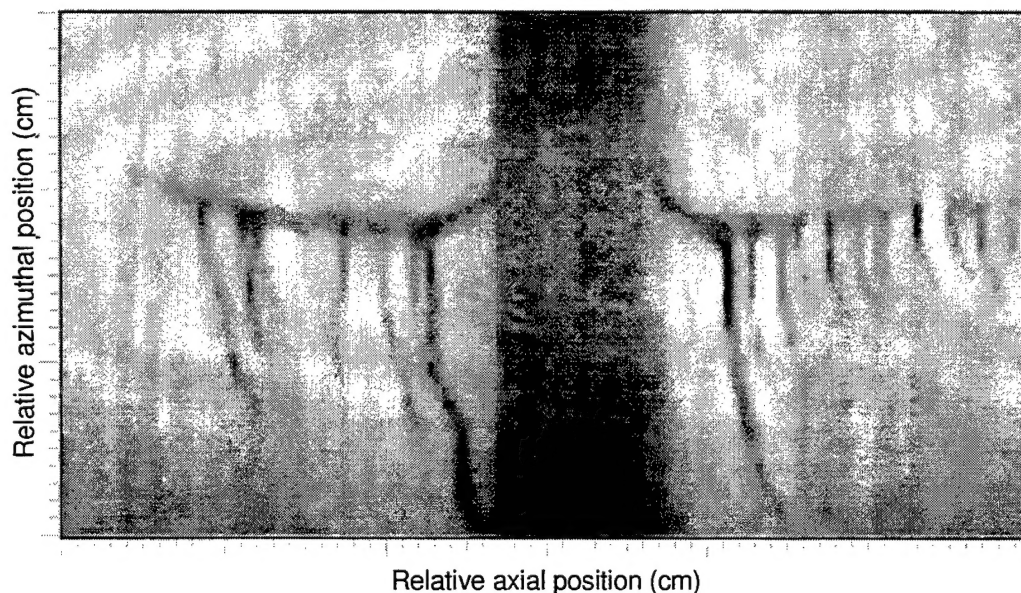
The Project Manager is Mr. Charles Buynak of the Wright Laboratory / Materials Directorate, WL/MLLP, Wright-Patterson AFB, OH, 45433. The Principal Investigator for Perceptics is Dr. Jim Youngberg. Principals among the project team were Dr. Marion Barker (Lockheed Martin), Dr. Paul Burstein (Skiametrics, Inc.), Mr. Fred Prater (Alliant Techsystems), and Dr. Todd Quinto (Tufts University).

## 1. EXECUTIVE SUMMARY

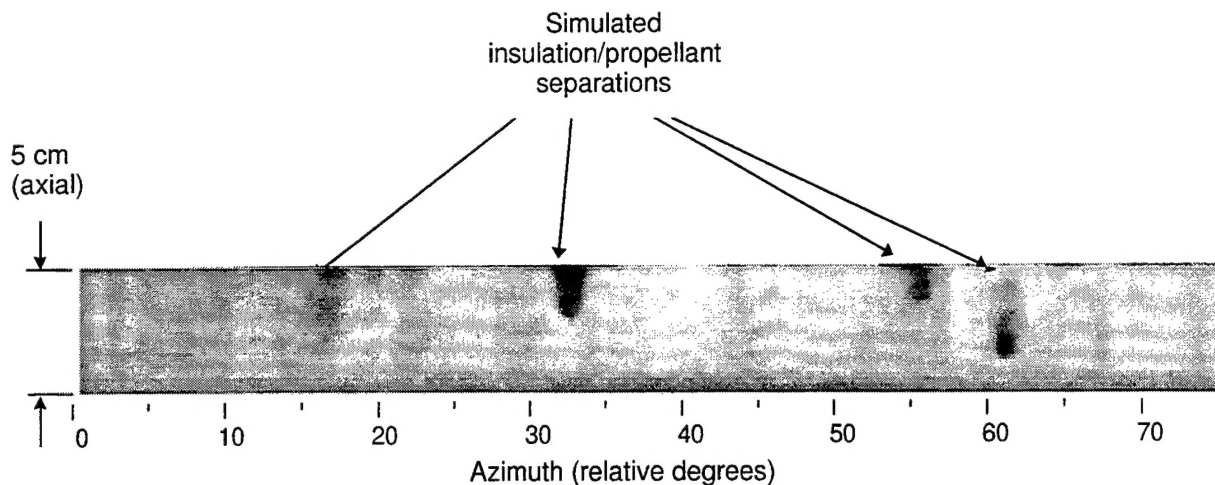
In the High-Resolution Three-Dimensional Computed Tomography (HR3DCT) program, a team comprised of Perceptics, Skiametrics, Alliant Techsystems, Lockheed Martin, and Tufts University set out to “demonstrate that HR3DCT is a viable and valuable technology for large SRM bondline inspection.” Our approach used a program-built test apparatus — the HR3DCT breadboard — to test underlying assumptions and, ultimately, to apply the HR3DCT algorithm to a variety of test objects. At the completion of this effort, HR3DCT’s few limitations and its remarkable potential are better-understood. We summarize its limitations and potential in the form of answers to our driving questions:

*Is HR3DCT viable for large SRM bondline inspection?*

An almost-unqualified yes. During the project we successfully imaged the bondlines of a Titan SRMU segment and a simulated Titan IV segment (both three-meters in diameter), a 1.8-m diameter strategic SRM, and a Minuteman third-stage dome. In each case, the reconstructed data exhibited sensitivity comparable to conventional CT. Bondline resolution was superior to conventional CT. Reconstructions were three-dimensional, facilitating immediate apprehension of bondline condition. The constant-radius images below, from reconstructions of the Titan SRMU and the Titan test objects, could not have been made with any other existing CT technology.



**Titan SRMU segment bondline.** This image represents the 0.5-mm thick region surrounding the segment’s insulator/propellant bondline. The vertical bar down the center of the image is an insulator lap joint. The large dark features on either side, with the associated downward-headed “runs,” reflect a slight thickening of a barrier coat. This image was an important confirmation of less-direct diagnostic evidence gathered concerning this anomaly using ultrasound and real-time radiography. (Scale is approximate)



**Titan IV segment bondline.** This image represents the 0.5-mm thick region encompassing the insulator/propellant bondline in a Titan IV simulator. The simulator had an insulated 9-mm thick steel case. The four dark elliptical areas represent unbonds intentionally inserted between the simulator's insulation and propellant.

The only qualification concerns a second Titan IV segment simulator with a steel case thickness of 19 mm (3/4 inch). Scatter swamped the deeply-attenuated inner-tangent signal, spoiling reconstructions of this object.

*Is HR3DCT valuable for large SRM bondline inspection?*

It can be cost effective as a diagnostic technology. HR3DCT's principal economic advantage is its ability to be implemented using existing radiographic facilities and equipment. Our analysis shows that a general-purpose diagnostic HR3DCT could be implemented in many existing radiographic facilities for about 10 percent of the cost of the most recent conventional CT instruments. Recurring per-inspection costs would be somewhat more than the costs associated with conventional CT systems, but insignificant when used on a diagnostic basis.

Alliant Techsystems offered this assessment following their evaluation of the cost-effectiveness of project results:

"Estimates show that implementation of HR3DCT on the Titan IV SRMU would offer a positive return on investment within 2 years."

"We feel that HR3DCT shows promise in each [of three considered] cost/benefit analysis methods and we are currently evaluating insertion of this technology into a number of programs."

"The following conclusions can be drawn from Alliant Techsystems' experience in examination of HR3DCT in the inspection environment:

- HR3DCT is an effective engineering diagnostic tool

- HR3DCT is cost-effective in replacing film inspections
- HR3DCT provides quantitative data in an orientation that the analyst can use in analysis
- HR3DCT is cost competitive with high energy RTR in a new program implementation
- HR3DCT provides data to the inspector in an unambiguous mode for interpretation”

*One final point...*

During the project, it became apparent that HR3DCT's high-resolution 3-D capability can be valuable in a variety of small component NDE problems. Thus, it was used to produce some spectacular images of a gas paths in a nozzle throat, and it is currently being seriously evaluated as a production and/or diagnostic NDE tool for aircraft components.

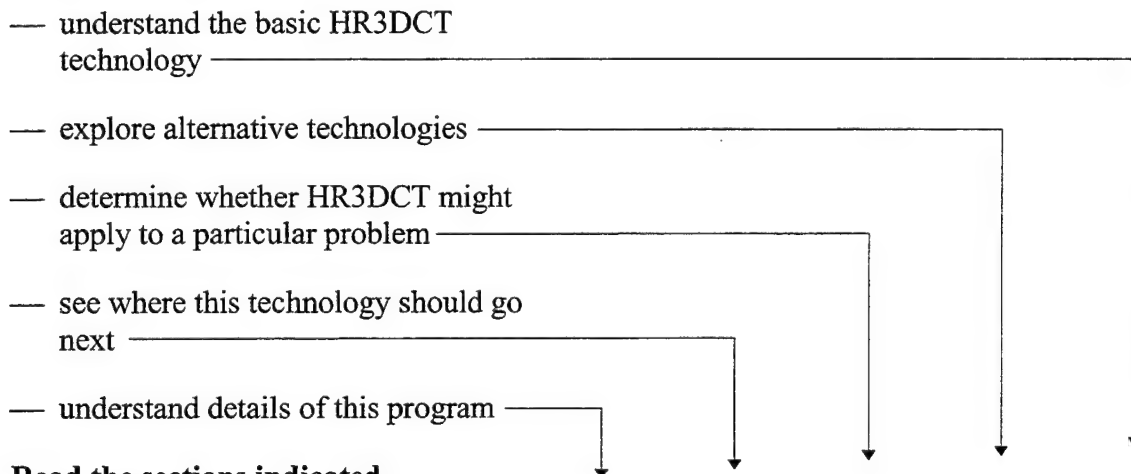
## 2. INTRODUCTION

### 2.1 Report organization

This report comprises eight sections. The present section introduces the program's objectives. Section 3 describes the conditions that motivated the program. Section 4 describes the project's technical approach and the set of facilities and equipment used for characterization. Component characterization results are described in Section 5. Experiment results appear in Sections 6 (HR3DCT) and 6.5.1 (ERA). Finally, information relating to future application of HR3DCT technology is presented in Sections 8 and 9.

Not all the above sections will be useful for every reader. To quickly determine what material will best suit your purposes, refer to the road map below.

#### If you want to —



#### Read the sections indicated —

|   |                                       |   |   |   |   |   |
|---|---------------------------------------|---|---|---|---|---|
| 2 | Introduction                          | ✓ |   |   |   |   |
| 3 | Background                            | ✓ |   | ✓ |   | ✓ |
| 4 | Program Approach                      | ✓ |   |   |   |   |
| 5 | Equipment Characterization Results    |   |   |   |   | ✓ |
| 6 | HR3DCT Results                        | ✓ |   |   |   | ✓ |
| 7 | Alternative Reconstruction Algorithms |   |   |   | ✓ |   |
| 8 | Application Guide                     |   |   | ✓ |   | ✓ |
| 9 | Conceptual Design Examples            | ✓ | ✓ | ✓ |   |   |



Finally, we note that not all project information that might useful to others is contained in this report. The following project documents provide additional material and are referred to herein:

- Youngberg, J.E., and Burstein, P., *High-Resolution Three-Dimensional Computed Tomography Interim Report*, submitted to Wright Laboratory, Wright-Patterson AFB under Air Force contract F33615-93-C-5327, January 1995.
- Youngberg, J.E., and Burstein, P., *High-Resolution Three-Dimensional Computed Tomography Breadboard Specification, Design, and Validation Plan*, submitted to Wright Laboratory, Wright-Patterson AFB under Air Force contract F33615-93-C-5327, March 1995.
- Quinto, E.T., *HR3DCT Project Final Report*, submitted to Perceptics Corporation under Air Force contract F33615-93-C-5327 (copy submitted to Wright Laboratory, Wright-Patterson AFB under Air Force contract F33615-93-C-5327, Nov 1995).

## **2.2 Program objectives**

The overall objective of this program was to demonstrate via breadboard testing HR3DCT technology's viability and value for large SRM bondline inspection. Each of the following paragraphs explains a supporting objective.

### **2.2.1 Incorporate existing 3-D and limited data CT technology**

In the course of this and prior projects, Perceptics and Skiametrics reviewed and experimented with both published and unpublished research in the areas of 3-D CT and limited data reconstruction (sampled in Section 3.2.2 and 7). We found that much of this work does not lend itself to practical application; other technology cannot be extended to large SRM bondline inspection. Nevertheless, some work — such as that by Feldkamp — has contributed ideas important to HR3DCT. Another alternative to the Feldkamp algorithm, the Exterior Reconstruction Algorithm (ERA), is a promising 2-D reconstruction which is logical for implementation on existing CT machines. The ERA was investigated as part of this project, with results as reported in Section 7.2. Other relevant work was reviewed as part of this program to ensure that our results reflect the best available technology.

### **2.2.2 Determine whether HR3DCT is practical for large SRM NDE**

This objective was intended to avoid an eventual disparity between laboratory feasibility demonstration and realizable production performance. A breadboard system was used to characterize HR3DCT over a range of potential use scenarios. The tests performed using the breadboard included:

- tests using article sizes and materials representative of a range of applications, including Minuteman, Titan IV, and Titan SRMU, and a nozzle,
- tests involving various component geometries, including the cylindrical, and dome regions of SRMs, and the throat region of a nozzle, and

- tests of usage tradeoffs (throughput vs. resolution vs. artifacts).

#### 2.2.3 Determine whether HR3DCT works with existing RTR and CT systems

An advantage of HR3DCT technology is the prospect of implementation with little or no hardware development, allowing it to be added to existing RTR or CT systems at a fraction of the cost of a new system. This advantage flows from the fact that HR3DCT's X-ray source and subject manipulation requirements are similar to (or less demanding than) the requirements for RTR and CT. An important objective of this project, therefore, was to verify that specific existing RTR and CT systems and hardware are suitable platforms for HR3DCT implementation.

#### 2.2.4 Determine cost and technical benefits to Air Force large SRM programs

The project was intended as a step toward full-scale implementation of HR3DCT technology. To help establish the crucial link between technology and real programs, we identified specific program needs addressed by the technology and forecast the one-time and recurring costs associated with implementing HR3DCT in these programs.

To ensure the correctness and completeness of our assessment, cost and throughput information was made available to Alliant Techsystems for evaluation by experienced NDE and program staff who evaluated this information in terms of immediate and potential benefits to specific production programs.

### 3. BACKGROUND

Bondlines remain one of the most pressing inspection issues for aircraft and solid rocket motors (SRM). Much effort has been expended in the investigation of bondline manufacturing and characterization by many companies and federal agencies, including the Air Force, the Navy, and NASA. Consequences of bondline failures include catastrophic failure in a variety of mission scenarios.

Existing inspection technologies, ranging from relatively simple ultrasonic and radiographic techniques to advanced ultrasonic and computed tomography (CT) approaches, have been applied to nondestructive testing and evaluation of bondlines. In several applications, the best overall radiographic inspection solution to date appears to be computed tomography. However, that technology — as expressed in "traditional" guise (e.g., the HECT, AFACTS, ARNIS) — falls far short of delivering adequate spatial resolution in the regions near the bondline. Small unbonds are completely unseen. Because the state of the art for spatial resolution is far coarser than the thinnest bondline components (0.1- 0.2 mm), it can be difficult even to locate the interface on which a suspected anomaly exists.

To address CT's inadequacy in large SRM NDE, Perceptics and Skiametrics have developed technology that extends the ideas of traditional CT so that large SRM components and some other axisymmetric object types can be inspected in a CT mode with much higher spatial resolution than that afforded by current techniques. This technology, which we have called High Resolution Three-Dimensional Computed Tomography (HR3DCT), requires no new hardware development — either X-ray source or detectors. HR3DCT can be implemented on existing instruments at existing facilities with a minimum of reconfiguration.

In this section, we (1) review why bondline NDE needs a new inspection tool, (2) show why our HR3DCT addresses this need in many applications, and (3) describe the results achieved prior to this project with HR3DCT precursor technology. While our discussion emphasizes SRM bondline applications, it can be applied to many non-SRM problems.

#### 3.1 Why bondline inspection demands a new NDE tool

This major section takes, as an example, large SRM bondline NDE needs, and details the shortfalls of existing technologies used to inspect bondlines. The section's message is simple: No existing combination of NDE techniques adequately characterizes bondlines over the range of geometries existing in current Air Force SRMs.

##### 3.1.1 Air Force program perspective of bondline problems

Bondlines provide critical structural integrity between materials. In SRMs, adhesive bondlines provide integrity between the case and the insulation and the insulation and the propellant. Although the criticality of unbonds varies as a function of location in the motor, and though criteria vary from program to program, most programs suffer from inadequate bondline NDE.

### 3.1.2 Why conventional methods are inadequate

Bondline NDE methods include ultrasonic techniques, thermography, and radiography. Each method has strengths and weaknesses, but individually and in combination they fall short of really solving the bondline NDE problem for large SRMs. Table 1 shows that the strengths and weaknesses of various NDE methods are often closely related to the geometry of the SRM and are thus regional.

**Table 1**  
**Strengths and weaknesses of ultrasonic and radiographic SRM NDE.**

| Material & Region        | Technique   | Characteristics  |
|--------------------------|-------------|--|
| Steel cylinder           | Ultrasound  | Large reflection coefficient between the steel and insulator causes large multiple reflections that mask the smaller unbond signature reflected from second- or deeper bondlines |
|                          | Radiography | Long chord lengths result in large absorptions; scatter drives the signal-to-noise ratio down, making bondlines involving steel difficult to interpret                           |
| Composite cylinder       | Ultrasound  | Non-critical delaminations or other scattering features within the case can mask signals originating in deeper bondlines   |
|                          | Radiography | Long chord lengths result in large absorptions; superposition of inherent material variations may mask bondline indications.   |
| Steel and composite dome | Ultrasound  | Complex geometries and/or accessibility problems in addition to the problems mentioned in connection with ultrasonic inspection of steel or composite cylindrical regions        |
|                          | Radiography | Design geometry leads to projection ambiguities; long chord lengths result in large absorptions; radial bondline resolution is inadequate  |

Ultrasonic techniques typically fail for large steel-cased specimens with several bondline layers of greatly-varied acoustic impedance. Tangential X-ray imaging examination, whether by film or by real-time radiography, fails for all but the largest separations (e.g., those 0.4 mm or thicker, over regions of at least several cm<sup>2</sup>). The net result is that current large SRM bondline NDE methods are inadequate.

### 3.1.3 Why conventional CT won't work

Conventional CT performs some SRM NDE tasks extremely well, such as imaging subtle density variations within homogeneous components throughout small- and medium-sized SRMs. This technique is arguably the best all-around NDE tool for SRMs in this size range. However, in large SRMs — those with diameters larger than 2.5 m — traditional CT encounters practical difficulties. These difficulties involve the X-ray source requirements, demands on mechanical systems, and impossible tradeoffs between resolution and acquisition time.

### 3.1.3.1 Practical X-ray sources are inadequate for conventional large-SRM CT

The rules of traditional CT require that X-ray absorption measurements be made at every angle and through every point in a test specimen slice. The largest currently-available X-ray sources have energies generated by 15 MeV electron linear accelerators and yield a radiation dose rate of 10-15 kRad per minute at 1 meter. As shown in Figure 1, this output is insufficient to penetrate the largest SRMs. For example, the radiation transmitted through the nearly-ten-foot chord tangent to Titan's inside bore, and through the inside tangent to the steel case wall near the segment ends is less than  $10^{-5}$  times the incident radiation.

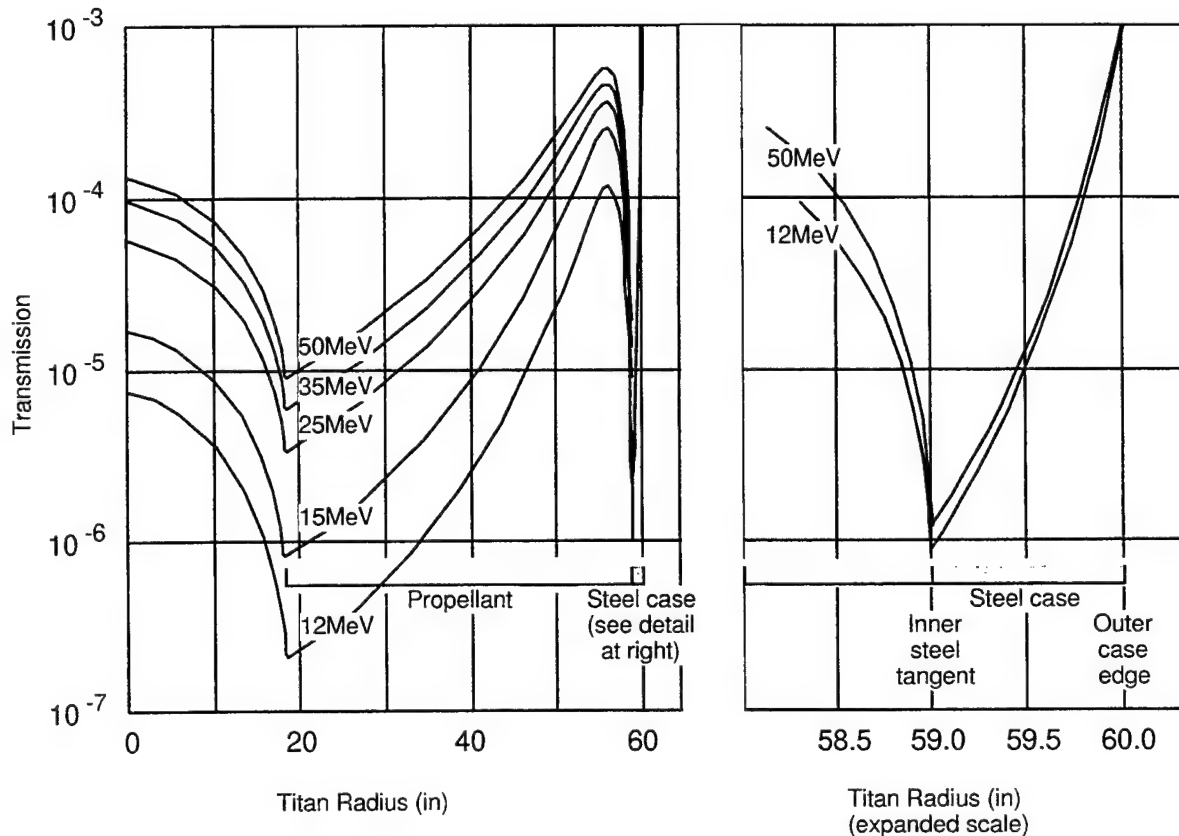


**Figure 1. Titan tangent X-ray transmission is too small for practical X-ray sources.**

Utilizing a higher energy (e.g., 30 or 40 MeV) results in neutron generation and the consequent residual radioactivity. A higher energy X-ray system also requires a greater physical length — typically 4 or 5 meters would be required at these energies for this microwave tuning band. X-ray source development would be prohibitively expensive, the facility would require significantly more shielding, and entrance to the bay after data acquisition would be delayed to allow the room to "cool" from the residual radiation. In addition, the available energy cone, i.e., the angle over which data can be acquired, from the higher energy X-ray beam would be reduced, since its width is inversely proportional to the energy. Thus, an effective 15 degree cone at 15 MeV becomes a 7.5 degree cone at 30 MeV. The number of traverses of the CT system to acquire the same data would be doubled over that of the lower energy source. Thus, the data acquisition time would be doubled. Figure 2 shows the results of a relatively conventional approach in terms of data acquisition time.

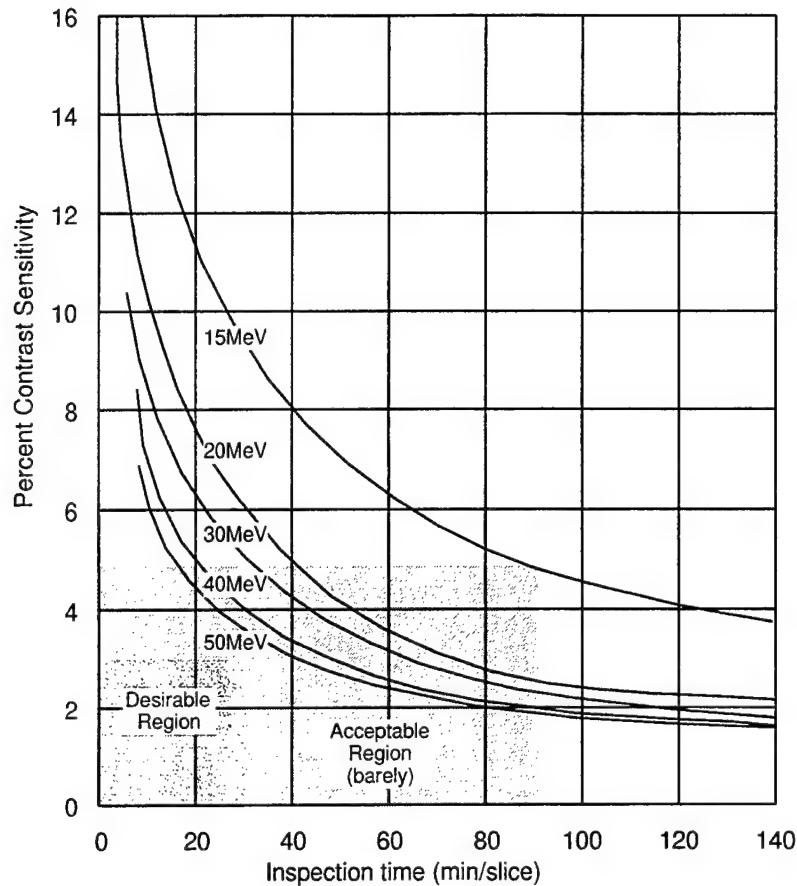


**Figure 2. Hard physical limitations result in CT tradeoffs.**

Tradeoffs among CT source energy, inspection time, and contrast sensitivity render conventional CT useless for large SRMs (we assume a  $1024^2 \times 5$ -cm thick slice).

### 3.1.3.2 Precision requirements drive conventional CT hardware costs impracticably high

One of the rules of traditional CT relates to mechanical tolerances and spatial resolution: The combined tolerances of all spatial uncertainties should not exceed one-third of the spatial resolution. This stringent requirement makes mechanical hardware approaches for conventional CT very expensive. In the large rocket motor CT systems in use today, two very different (and expensive) hardware approaches are invoked to meet this requirement of correlating in space the measurements made over the body of the large rocket motor. Ultimately, the uncertainties in these systems amount to approximately 0.5 mm in the AFACTS II system and 0.2 mm in the HECT systems. These absolute tolerances are required over distances of approximately 3 m. In conventional CT, these extreme requirements are unavoidable and very expensive.

### 3.1.3.3 Resolution trades unfavorably with inspection time in conventional CT

A basic rule from conventional CT dooms its use for large SRMs. This rule states that if reconstruction sensitivity and the X-ray source (and geometry) remain constant, the time spent acquiring data varies inversely with the *cube* of the resolution. A practical example shows what this means:

For a standard 1024 resolution elements on a Titan rocket motor, the minimum data acquisition time for a single CT slice is *90 minutes* using a conventional 15 MeV X-ray source, resulting in a relatively poor contrast of 5 percent, and an almost-useless resolution of 3 mm. By the above rule, if we double the resolution — achieving only 1.5-mm resolution — data acquisition time would increase to 12 hours per slice. Our experience in the analysis of data from AFACTS II and from HECT systems shows that 1.5-mm resolution is simply insufficient for bondlines. For bondline NDE, spatial resolution element sizes on the order of 0.2 mm to 0.5 mm are necessary to provide adequate sensitivity to the presence of anomalies. *Unfortunately, by the rule, the time to acquire a single slice at 0.5-mm resolution would be 324 hours!* Conventional CT is impractical for large SRM bondline inspection.

#### 3.1.4 Conclusion: A new NDE technology is needed

Despite pressing program needs, no existing combination of NDE techniques adequately characterizes bondlines over the range of geometries existing in current Air Force SRMs. While conventional CT offers the best all-around technique for small- to mid-sized SRMs, it is not applicable to large rocket motor inspections because an effective application would require

- new X-ray source development,
- an expensive, precise mechanical handling system,
- an expensive facility to provide for X-ray shielding, and
- an inordinate amount of inspection time to make reasonable images.

Even with these problems solved, the spatial resolution achievable in such a conventional CT system would be insufficient to detect, identify, and measure small bondline anomalies.

### 3.2 The CT-based solution

In this major section we shift our focus to a novel solution to the large SRM bondline NDE problem. We first explain the key insights which lead to our solution, then discuss HR3DCT's central technology: the reconstruction algorithm.

#### 3.2.1 Key insights

Our HR3DCT solution is based on the recognition that

- bondline anomalies are oriented along tangential directions,
- to image the important features of a bondline problem, we require good spatial resolution *in the radial direction only*, and
- the interior of the large SRM need not be reconstructed.

While these insights seem simple and obvious, their implications are powerful, as discussed in the paragraphs below.

#### 3.2.1.1 Implication 1: For bondline CT, only tangent projections are needed.

Consider a 0.2-mm separation between insulation and propellant. Figure 3 shows, as a function of distance inward from such a separation, the change in the transmitted signal which is attributable to the separation. Where the effect on the transmitted signal is less than the imager's detection threshold, the separation is not represented by the measurement. The graph with the expanded horizontal scale (right) shows that this condition dominates the entire view except for the 5-cm-wide portion just inboard from the tangent. In this narrow part of each view, useful bondline information can be measured.

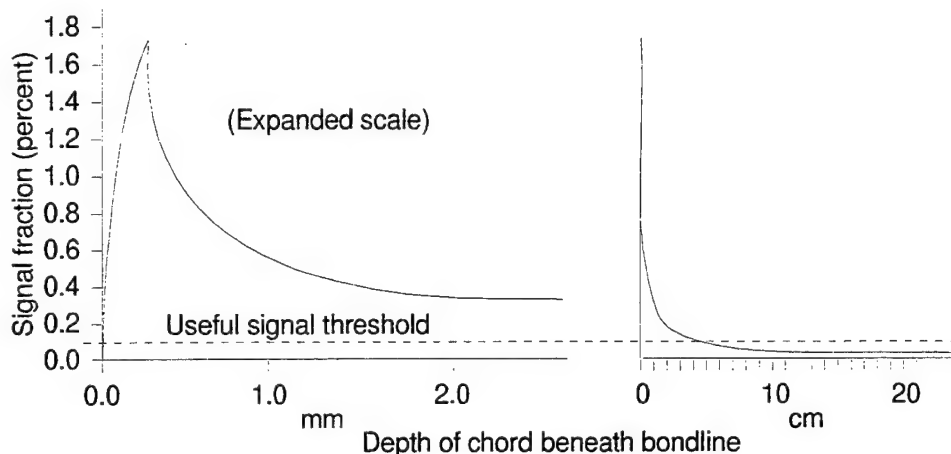


**Figure 3. Signal fraction due to small separations.**

A 0.2-mm separation produces a measurable signal contribution within only the first 5 cm of the tangent. This assumes a 3-m SRM with a 25-mm steel case.

#### 3.2.1.2 Implication 2: For bondline CT, an area (RTR) detector is best.

The second insight, that good spatial resolution is required only in the radial direction, is consistent with the scale of detail shown in Figure 1. Clearly, to image features this small, we require a detector resolution on the order of 0.2 mm. Discrete detectors common in most CT systems cannot achieve this resolution without resorting to complex motion and data pre-processing. Even then, acquisition times are unacceptably high. We therefore choose a detection scheme employing a high-energy area imager such as is used in large SRM RTR. Tangential X-ray measurements can be made with relatively good spatial resolution (down to 0.25 mm) as long as an imaging detector is used to acquire the data. This use of an RTR imager to produce quantitative results is unconventional, but central to our approach.

#### 3.2.1.3 Implication 3: For bondline CT, a simple mechanical handling system will do.

The third insight, about not having to reconstruct the interior of the motor, leads us to two conclusions and a corollary. The first conclusion is that we need not acquire the portion of each view that penetrates deeply through the rocket motor, a conclusion consistent with the fact that we need only tangential data. The second conclusion is that, unlike conventional



CT, we can decouple the measurements that are made on one side of the motor from those that are made on the other. The logical corollary is that, with the proper algorithm, a mechanical handling system can be utilized that does not provide high absolute accuracy over large distances (e.g., 0.1 mm over 3 m). Only local accuracy over the range that a given point to be imaged stays in the field of view is important. Indeed, the obvious motion device is a rotary table of the type and accuracy utilized in normal tangential X-ray imaging.

#### 3.2.1.4 *The bottom line for imaging requirements*

The insights mentioned at the start of this section lead to a remarkable set of imaging requirements. We have shown why, for bondline CT, (1) only tangential projections are needed, (2) an area (RTR) detector is best, and (3) a simple mechanical handling system is adequate. The success of this approach depends on having a reconstruction algorithm that can deal with the fact that over ninety-five percent of each conventional CT view will be missing. Perceptics and Skiametrics have developed such an algorithm. Our algorithm allows us to use a standard rotator, a standard RTR imaging system, and a standard X-ray source to produce high resolution images of the outside periphery of test articles. This new technology involves no new hardware development, only a configuration change (e.g., collimators and precision position encoders) to existing X-ray generation and detection equipment.

#### 3.2.2 A crucial component of HR3DCT is the algorithm

The HR3DCT reconstruction algorithm solves an easily-described problem. In this problem, we acquire at high radial resolution a small portion of one edge of each view normally measured. As shown in Figure 4, this arrangement interrogates just the outer annulus of the object. The problem is to invert the projection transform, reconstructing the material of this interrogated annulus.

Although a large fraction of the information normally measured in CT is missing, we actually have all that we need. Our ultimate goal is the detection of circumferentially-oriented features such as intercomponent separations and intracomponent delaminations. Such features produce measurable modulations in the detected signal *only* when they are in close alignment with the X-ray beam. This occurs precisely in the tangent view depicted in Figure 4. Moreover, since important details are measured only in the tangent view, we may assume that the information borne by the remainder of the view results only from the general structure of the motor. Such information is known *a priori* to an accuracy that is acceptable for bondline reconstructions. The challenge is to find a reconstruction algorithm which optimally utilizes both the measured data and the prior knowledge which we have in this problem.

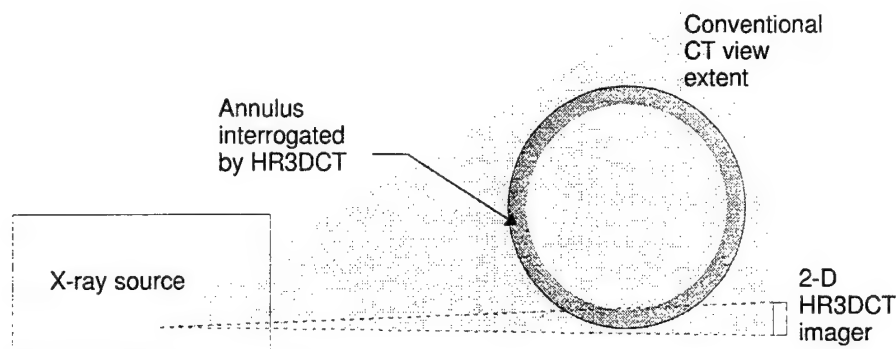


**Figure 4. Simple limited-angle CT diagram.**

The limited angle CT problem involves reconstruction of material within the narrow annulus that is interrogated by tangent projections.

In projects extending over the past several years, Perceptics and Skiametrics have investigated several reconstruction technologies, including those summarized in Table 2 Candidate HR3DCT reconstruction approaches.. Of the algorithms investigated, a modification of the Feldkamp algorithm was finally selected.

**Table 2**  
**Candidate HR3DCT reconstruction approaches.**

| Algorithm                                   | Description  | Evaluation   |
|---|--|--|
| Filtered backprojection <sup>1</sup>        | Common in conventional 2-D CT. Successfully and practically inverts the Radon transform when sampling issues are properly addressed. Requires modifications to address limited angle reconstruction. | The algorithm provides multiple opportunities for introduction of prior knowledge.           |
| Fourier reconstruction <sup>2</sup>         | 2-D algorithm which arises from efforts to analytically invert the Radon transform. Occasionally used in conventional CT.  | Not easily adapted to partial reconstruction using prior knowledge.                          |
| Algebraic Reconstruction (ART) <sup>3</sup> | Iterative technique which is robust, different from deterministic algorithms, easy to implement. Probably adaptable for 3-D reconstruction.  | This is a general technique which has been strengthened by various enhancements, e.g. EFIRT. |

<sup>1</sup>Kak, A.C., and Slaney, M., *Principles of Computerized Tomographic Imaging*, IEEE Press, New York, 1988, pp. 77-86.

<sup>2</sup>Bracewell, R.N., and Riddle, A.C., *Inversion of Fan-Beam Scans in Radio Astronomy*, The Astrophysical Journal, Vol. 150, Nov 1967.

<sup>3</sup>Oppenheim, B.E., *More Accurate Algorithms for Iterative 3-Dimensional Reconstruction*, IEEE Trans. Nucl. Sci., Vol. NS-21, Jun 1974.

|  |   |   |
|--|---|---|
| Extended Field Iterative Reconstruction Technique (EFIRT) <sup>4</sup> | An ART variant which attempts to force the effects arising from noisy view data into an annulus which is outside the circle of reconstruction. Probably adaptable for 3-D reconstruction. | Proved to be unworkably slow (even to the point of never converging). This was due to the fact that when available views are incomplete, portions of the reconstruction estimate are updated only occasionally.                           |
| Exterior Reconstruction Algorithm (ERA) <sup>5</sup>                   | An approach adapted from Perry <sup>6</sup> which explicitly ignores missing data, relying on a set of boundary condition assumptions. Not adaptable for 3-D reconstruction.              | This technique was selected for additional investigation as part of this program. Reconstructions and related discussion appear in Section 7.1.   |
| Maximum entropy methods <sup>7</sup>                                   | A 2-D approach based on the assumption that a good estimate of the reconstructed image maximizes its entropy, subject to known constraints.   | Within each projection, unless all measurements are available, severe artifacts result.   |
| Extended maximum entropy <sup>8</sup>                                  | 2-D algorithm that substitutes the "discriminatory function" (related to cross entropy) for entropy.  | Noisy in high density, high absorption; reconstructs badly along large gradients (e.g. bondlines)   |
| Limited data tomography support minimization <sup>9</sup>              | Utilizes a "penalty function" that ultimately acts as a "subtraction operator" from an a priori image.  | Good for small, high-density, compact objects; likely to fail at high intrinsic gradients (e.g. interfaces where anomalous features occupy only a few pixels along the interface)   |
| Feldkamp cone-beam algorithm <sup>10</sup>                             | Computationally tractable (unlike most cone-beam algorithms). Reduces to filtered backprojection in the midplane. Admits modifications for limited angle reconstruction.                  | Artifacts are significant several degrees off the midplane. HR3DCT successfully avoids the problem by staying within a few degrees of the midplane. Our specific modifications to this algorithm are described elsewhere in this section. |

<sup>4</sup>Crowther, R.A. and Klug, A., *Three-dimensional image reconstruction on an extended field — a fast, stable algorithm*, Nature, Vol. 251, 11 Oct 1974, pp. 490-492.

<sup>5</sup>1983, J.Math.Anal.Appl. 95, 437 and 1988, Inv.Prob. 4, p. 867

<sup>6</sup>1977, J. Math. Anal. Appl. 59, p. 324

<sup>7</sup>Minerbo, G., *MENT: A Maximum Entropy Algorithm for Reconstructing a Source from Projection Data*, Computer Graphics and Image Processing, Vol. 10, pp. 48-68.

<sup>8</sup>Dusaussoy, N.J., and Abdou, I.E., *The Extended MENT Algorithm: A Maximum Entropy Type Algorithm Using Prior Knowledge for Computerized Tomography*, Submitted to IEEE Trans. Acoust., Speech and Sig. Proc.

<sup>9</sup>Roberts, R.A. (Iowa State Univ.), *Limited Data Tomography Using Support Minimization*, Rev. Prog. Quant. NDE, Vol. 11, Plenum, N.Y., 1992

<sup>10</sup>Feldkamp, L.A., and Jesion, G., *3-D X-ray Computed Tomography*, Review of Progress in Quantitative Nondestructive Evaluation, Vol. 5A, Plenum Publishing, 1986.

### 3.2.2.1 Our modified Feldkamp cone beam algorithm

The Feldkamp algorithm assumes a complete set of 2-D projections, each of which spans the object. In HR3DCT, the large attenuations which exist along all but the tangent projections make significant portions of each view unavailable. Our earlier work<sup>11</sup> developed an approach to the problem of reconstructing the portion of the object spanned by the limited measured data. The missing projection data represent the information which normally would be measured in the off-tangent portion of each view. In HR3DCT, the significance of this off-tangent information is small. In large SRMs the differential attenuation of any case or bondline irregularity contributes to the overall attenuation at a level which is beneath the inherent noise of the measurement process. The result is that the off-tangent projection data contribution is limited to a smooth, slowly-varying component which is a function of radius (and axial position in dome areas). This component can be predicted from knowledge of the general SRM geometry. On this basis, we might ignore the missing data entirely, were it not for a detail of the reconstruction process: An artificial truncation of the tangent portion of the projection can cause finite filter ringing effects which produce severe distortions in the reconstruction. To prevent this edge from distorting the results of each view's convolution, we synthesize projection data inward from the inner edge of the intended reconstruction for a distance of at least one half the convolution filter width. This approach demands easily-achieved value- and slope-continuity between our *a priori* data and the measured data.

## 3.3 Prior results

The results which lead to this program come from a number of separate programs that Perceptics and Skiametrics have pursued together over the past several years. Exploration of the possibility of using limited data CT with large SRMs began in 1986 with a program to examine methods for inspecting Titan 34D segments, particularly the areas near the joints. That study identified several promising technologies including 2-D limited data computed tomography, and several high-energy X-ray scatter-based approaches. In the end it was clear that the limited data X-ray transmission approach offered the best hope for optimizing contrast, spatial resolution, and inspection times. Projects and results which followed this beginning are presented in the following subsections in approximate chronological order.

### 3.3.1 PACT program

Perceptics and Skiametrics, working with Alliant and with Tufts University, investigated a number of algorithms for reconstructing a 2-D annulus from tangent data. Under this high-energy Partial Angle CT (PACT) program, we accomplished two major goals: (1) We made experimental measurements at the Alliant Titan facility that gave us confidence that the approach would work, and (2) we developed an algorithm that would work with conventionally acquired RTR data.

---

<sup>11</sup>J.E. Youngberg, P. Burstein, F.M. Prater, "Reconstruction of Annular Cross-sections of Rocket Motors Using Incomplete Data Sets Generated From Real Time Radiography", (Proceedings of the May 1991 JANNAF NDE Subcommittee meeting)

A low-energy experimental verification of PACT funded by NASA through the SPIP (Solid Propulsion Integrity Program) Bondlines program was also conducted. In this project, projections from one of the SPIP program's Ballistic Analog Motor (BAM-0) test objects were reconstructed. In conjunction with this effort, HR3DCT data were taken on a Lucite test article intended to probe detection limitations. The experimental setup and phantom geometry are shown in Figure 5. PACT experiment equipment and phantom.

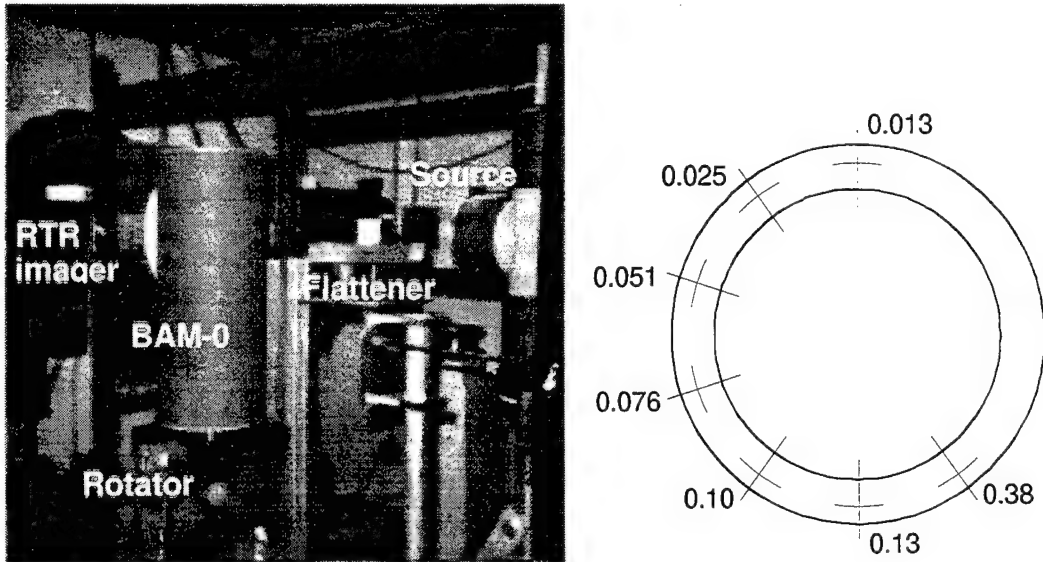


**Figure 5. PACT experiment equipment and phantom.**

Our PACT BAM-0 experiment utilized conventional radiographic and RTR hardware. The diagram at right shows the layout of the Lucite phantom — an annular plastic phantom with high-density inclusions (widths in mm) located every 36 degrees.

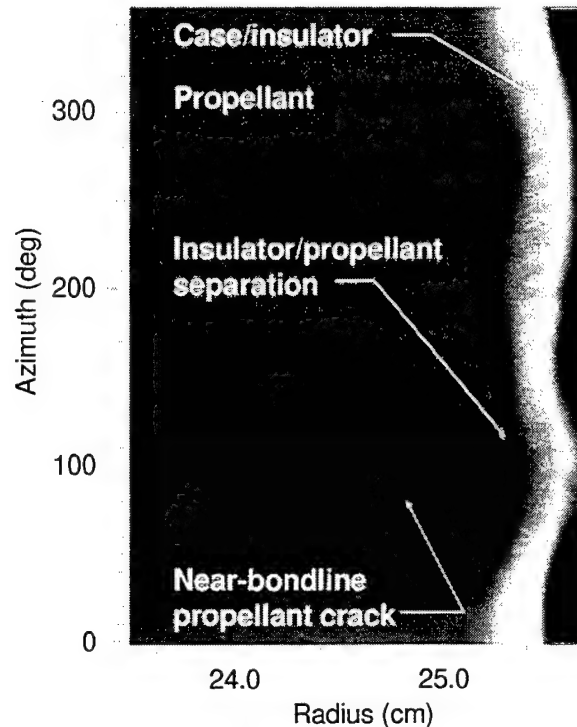


**Figure 6. PACT BAM-0 reconstruction.**

Initial PACT results, using laboratory data, match predicted performance. The BAM-0 reconstruction clearly shows deformation of the case which resulted in the easily-detected insulator/propellant separation. A 70-degree-long near-bondline crack is clearly imaged as it wanders over a 13-mm radial range. The scale is approximate.

Preliminary reconstruction results are displayed in Figure 6. The reconstructions clearly show the imperfect roundness and concentricity of the respective test articles. The BAM-0 reconstruction also shows a large near-bondline propellant crack which wanders radially over an azimuthal range of about 80 degrees. A large insulator/propellant separation is also indicated in this same azimuthal region. The BAM-0 case is 2-mm steel, with a 6-mm insulator. The Lucite test article reconstruction easily imaged four laminar inclusions ranging from 0.05 to 0.13 mm in thickness, as shown in Figure 7.

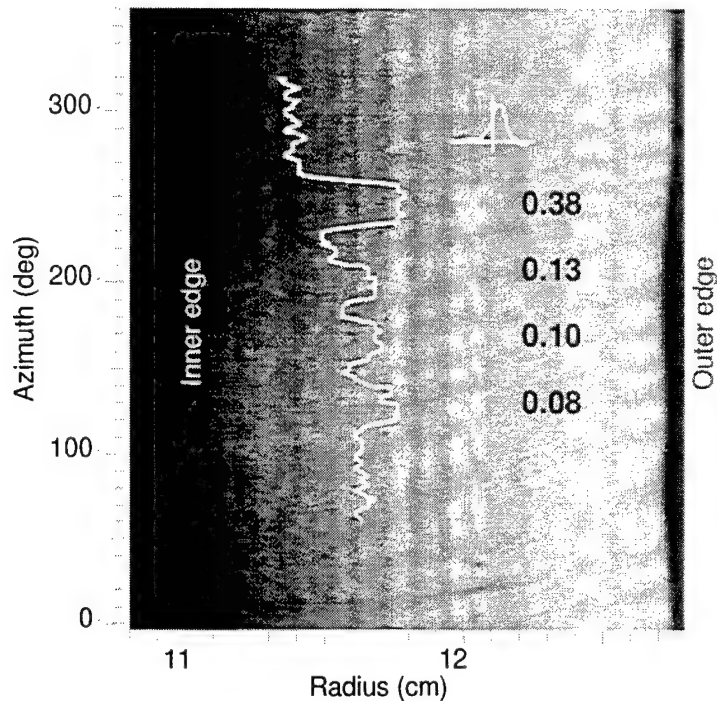


**Figure 7. PACT Lucite phantom reconstruction from synthetic data.**

The homogeneous Lucite phantom's four largest inclusions (measuring 2.5 cm azimuthally by 0.08 to 0.38 mm radially) are detected, as shown by the superimposed profile. The scale is approximate.

### 3.3.2 The initial HR3DCT program

The initial High Resolution Three-Dimensional Computed Tomography (HR3DCT) program had its genesis in the realization that certain cone-beam reconstruction algorithms for volume CT had become computationally tractable. Perceptics and Skiametrics experimented with available algorithms, adding *a priori* information about expected anomalies, resulting in an algorithm designed to work well on large SRMs in three dimensions. This algorithm was a true 3-D approach, and as such, would provide the combination of good data acquisition times (because multiple slice data are acquired simultaneously), good axial resolution (particularly important in domes, and an area where conventional single-slice CT is deficient), and could be implemented in relatively inexpensive dedicated computers.

Our initial funded work was through NASA: The goal was to (1) demonstrate the technical feasibility of combining high-resolution limited-data set CT with three-dimensional CT, (2) predict performance limitations resulting from the implementation of this approach using real-world RTR systems as the X-ray detection elements, and (3) identify beneficial applications of this approach. The results confirmed the feasibility of the new technology. A detailed simulation of the RTR data acquisition process was constructed for use in testing the HR3DCT process. This simulation provided means to assess the impact of variations in radiographic geometry, object configuration, mechanical error, radiographic artifacts, and imaging artifacts. A prototype HR3DCT reconstructor was also developed and tested. It was used with simulated data in a series of experiments designed to test the mathematical validity

of the reconstruction approach and to study the consequences of different data acquisition geometries.

The results of these experiments were evaluated to discover potential problems with the HR3DCT approach and to develop a basis for predicting the capabilities and limitations of a production implementation. After determining that realistic data acquisition methods could result in high-quality reconstructions with the chosen algorithm, we performed a test of the detectability of specific manufacturing defects in a simulated SRM assuming that the data acquisition system was designed around readily-available RTR X-ray detection systems. The result was a prediction that 0.1-mm chamber-insulator separations could be easily detected under the most difficult circumstances, and that 0.05-mm separations would often be detectable.



## 4. PROGRAM APPROACH

This section details our approach and the rationale behind it. This section has five major subsections. The first three — corresponding to the project's three major tasks — describe the reason for, technical background, and the relationships among the tasks. The final two subsections describe the facilities, equipment, and test objects used in the project.

### 4.1 Task 1 Preliminary assessment

This was a preparation task. The goal in this task was to examine relevant previous work for applicability, to gather design-influencing experimental data, and to reduce risk by testing crucial breadboard elements.

Before designing the project's breadboard hardware and software, we gathered specific information about several full-scale HR3DCT technical issues. This effort was primarily experimental. We assessed

- previous related work in the areas of 3-D and limited data CT reconstruction,
- capability of conventional RTR imagers as HR3DCT components, and
- physical characteristics of full-scale HR3DCT implementation, such as scatter, collimation, geometric tradeoffs, and direct/indirect signal effects.

Details of these activities are described in the following subsections.

#### 4.1.1 Evaluation of previous related algorithm work

High-resolution 3-D CT algorithms are not found in the literature. However, work has been published on *pieces* of the HR3DCT problem. For example, reconstruction from a limited data set is a broad and frequently-considered topic. Likewise, reconstruction of a solid volume from cone-beam projections has been studied. Two principal study tasks were undertaken to insure that useful contributing HR3DCT technologies were taken into account.

First, an implementation of Tufts University's ERA method of limited data reconstruction was prepared for direct evaluation with data that was acquired during Task 1. Previous studies had suggested that this algorithm had potential for implementation on existing CT hardware. The algorithm had performed well in tests using simulated data, but had never reconstructed actual RTR data. During this task we also prepared a test object from which preliminary data could be measured. This preliminary data enabled a first evaluation of ERA reconstruction.

Second, Tufts University independently examined current work in the field to find, evaluate, and summarize alternatives to portions of the HR3DCT reconstruction algorithm. We

reviewed work pertaining to data completion algorithms, singularity detection<sup>12</sup>, Lambda tomography<sup>13</sup>, work from Iowa State University Center for NDE, recent QNDE papers, and the general literature in the areas of limited data CT and cone-beam algorithms.

Results of this activity are described in Section 7.

#### 4.1.2 Evaluation of RTR imager technology for HR3DCT application

During Task 1 we experimentally explored non-ideal characteristics of RTR imagers as they pertain to HR3DCT data acquisition (initial consideration was undertaken in previous work<sup>14</sup>). Two categories of measurement were made: measurements of fundamental imager limitations, and measurements of reversible distortions. The imagers used in our work are described in Section 4.4.2. Methods and results of our characterization work are described in Section 5.1. These results were taken into account in the breadboard design and in performance projections and concept design work reported in Section 9.

#### 4.1.3 Evaluation of the radiographic characteristics of full-scale HR3DCT implementation

During Task 1 we experimentally quantified various radiographic factors which affect HR3DCT data acquisition (initial consideration was undertaken in previous work<sup>15</sup>). Variables that affect the quality of radiographic images fall into two groups: those which are beyond our control (to which must simply adapt) and those that we can control. The first group includes X-ray beam focal spot size and shape, the beam profile within the detector's solid angle, and the nominal geometry and materials comprising the test article. The second group, includes the X-ray energy, the source to object distance (SOD), the source to detector distance (SDD), X-ray scatter, and the specific controlling factors (e.g., compensator/flatteners and collimators) that can be customized to the needs of each facility. The methods and results of this investigation are described in Section 5.2.

---

<sup>12</sup>This algorithm is well suited for region of interest tomography. It utilizes a projection subset to reconstruct a neighborhood. Preliminary tests on mathematical phantoms are promising. This method is suitable for 2- and 3-D reconstruction. It will provide images much more quickly than even a local inversion method.

<sup>13</sup>Mathematicians Kennan Smith, et al., and Alfred Louis have developed Lambda tomography, another algorithm useful for region of interest tomography. This method does not reconstruct exact densities but a picture that corresponds to the object and its singularities. This method can be adapted to 3D volume CT.

<sup>14</sup>Youngberg, J.E., and Burstein, P., *High Spatial Resolution Three-Dimensional Imaging of Critical Regions*, final report submitted to NASA/MSFC under contract NAS8-38241, May 1991, pp. 33.

<sup>15</sup>Youngberg, pp. 31-32.

## **4.2 Task 2 Specify, design, build and validate a breadboard system**

In this task we used the information obtained in Task 1 to build and characterize a breadboard HR3DCT system, and made measurements to enable confident predictions to be made about HR3DCT's potential for production NDE.

The are four principal outputs from this task were

- a detailed plan for validation of HR3DCT,
- a documented and reviewed breadboard specification and design,
- the completed breadboard, and
- characterization result data, which were inputs to Task 3.

Following Task 1, we undertook design and validation of a full-scale HR3DCT breadboard. Our breadboard provided, in an easily-reconfigurable form, the essential functions of a HR3DCT implementation. Its flexibility enabled ideas and approaches to be easily and inexpensively tested. Validation consisted of running the breadboard through a set of tests with appropriate test articles which enabled us to predict how HR3DCT will perform in real applications. The validation was conducted at Alliant's Magna, Utah facility.

During the validation task, we used a variety of acquisition and motion devices, including two RTR imager technologies, two manipulators (Section 4.4.3), and test article sizes and compositions spanning the range of Air Force SRM configurations (Section 4.5). This approach avoided unwarrantedly optimistic or pessimistic conclusions that might otherwise result from a more limited validation plan.

A feature of our validation plan was our conscious use of existing hardware and software, including an existing HR3DCT reconstruction code, existing phantoms where possible, and existing RTR and motion equipment rather than designing and building new equipment. This approach was consistent with the intention that HR3DCT be implementible at low cost on existing equipment. Details of the equipment used in this task are described in Section 4.4. Methods and results are described in Section 6.

The on-site validation involved scans of the test articles using a variety of equipment. This series of scans was planned so that resulting data represent the range of production-scale Air Force SRM sizes, materials, and geometries, enabling the conclusions and performance projections of Task 3.

The Validation Plan also included the measuring of data reconstructed using the ERA, enabling our conclusions about the potential of this method for use with existing RTR and CT systems.

### **4.3 Task 3    Analyze HR3DCT performance based on production-scale scan results**

In this task we used the data taken during the Task 2 validation to project HR3DCT's potential for production NDE.

Principal outputs from this analytical task include

- a conceptual design, with performance projections and costs, for a prototype HR3DCT implementation, and
- an analysis of the costs and benefits of a production HR3DCT application.

Evaluation of the HR3DCT breadboard validation was focused on two primary goals. These were to determine, first, what the breadboard revealed about the capability and applicability of HR3DCT for practical NDE, and second, how what we have learned fits into the needs of individual Air Force programs.

Once the validation experiments were completed, Perceptics and Skiametrics performed detailed analysis of the results. We first ensured that all HR3DCT and ERA reconstructions were correct. We then directly measured principal imaging parameters (basic resolution components, the 2-D modulation transfer function (MTF), sensitivity, artifact types and levels, and efficiency) for each test article type (cylindrical, Y-joint, dome) and size and location within the article. These parameters provided us with a consistent picture of HR3DCT's capabilities across its potential application domain. At this point, we identified production programs where application of HR3DCT promises the most benefit. For these programs we addressed the practical implementation issues, such as achievable throughput, and modifications needed to existing NDE facilities. This information was provided to Alliant, who assessed the validation results to determine whether HR3DCT NDE would be cost-effective in the production and maintenance of their Air Force products. During this phase of effort, product engineering and NDE personnel at Alliant evaluated the HR3DCT reconstructions of the various test articles in relation to conventional NDE results for these same articles, and relative to their knowledge of the design and practical problems encountered in their respective programs. Their objective was to determine whether HR3DCT in fact provides useful and important NDE information not available through conventional film, RTR, CT or UT NDE modalities. With this information in hand, along with the throughput, and costs (initial and recurring), Alliant performed a cost/benefit analysis for HR3DCT NDE on their Air Force programs.

The output of this effort combines the results of our own and Alliant's analysis, and a conceptual design and estimated costs for three prototype production machines, implemented on an existing RTR or CT machine, located at a SRM manufacturer or Air Force maintenance facility. These items appear in Section 9.

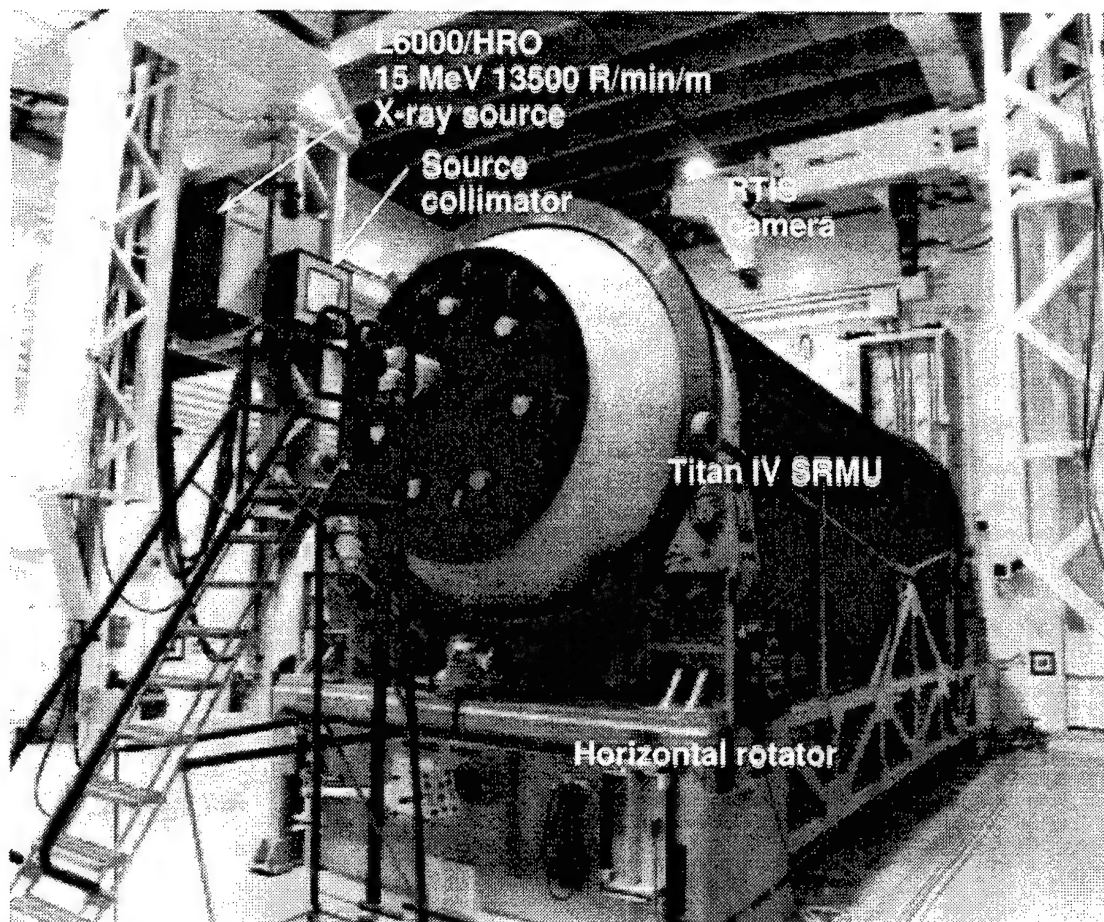


**Figure 8. The RTIS platform.**

The RTIS facility as configured for automated tangent RTR of Titan IV SRMU segments.

#### **4.4 Facilities and equipment**

The test platforms — especially their imager and the facility components — were an important part of Task 2. These items were a carefully-selected part of our approach. Consistent with the program goals described earlier, we chose test platforms that represent a range of current RTR alternatives, but which required minimal design, fabrication, or modification.

The validation was conducted in Alliant's Titan RTIS facility. It used three basic equipment arrangements or "platforms". Our principal platform comprised the Lockheed Martin SSXI imager, a custom rotator, and the HR3DCT workstation. The Lockheed Martin imager had a LKH-5 conversion screen. It is on this platform, with its well-characterized components, that the detailed experiments which establish HR3DCT's limitations and characteristics were performed. The second platform was identical to the first with the substitution of a GOS X-ray conversion screen. Our third platform used the same facility, rotator and workstation, but substituted an Isocon-based imager for the SSXI imager. Either the custom rotator or the RTIS facility rotator was used. Its digital data output was loaded onto the workstation for reconstruction and analysis. The three platforms shared a Varian L6000 15 MeV X-ray source. Together the imagers in these platforms are a cross-section of high-energy RTR

imagers in successful, current production use. These are not experimental imagers or new designs, but practical technology.

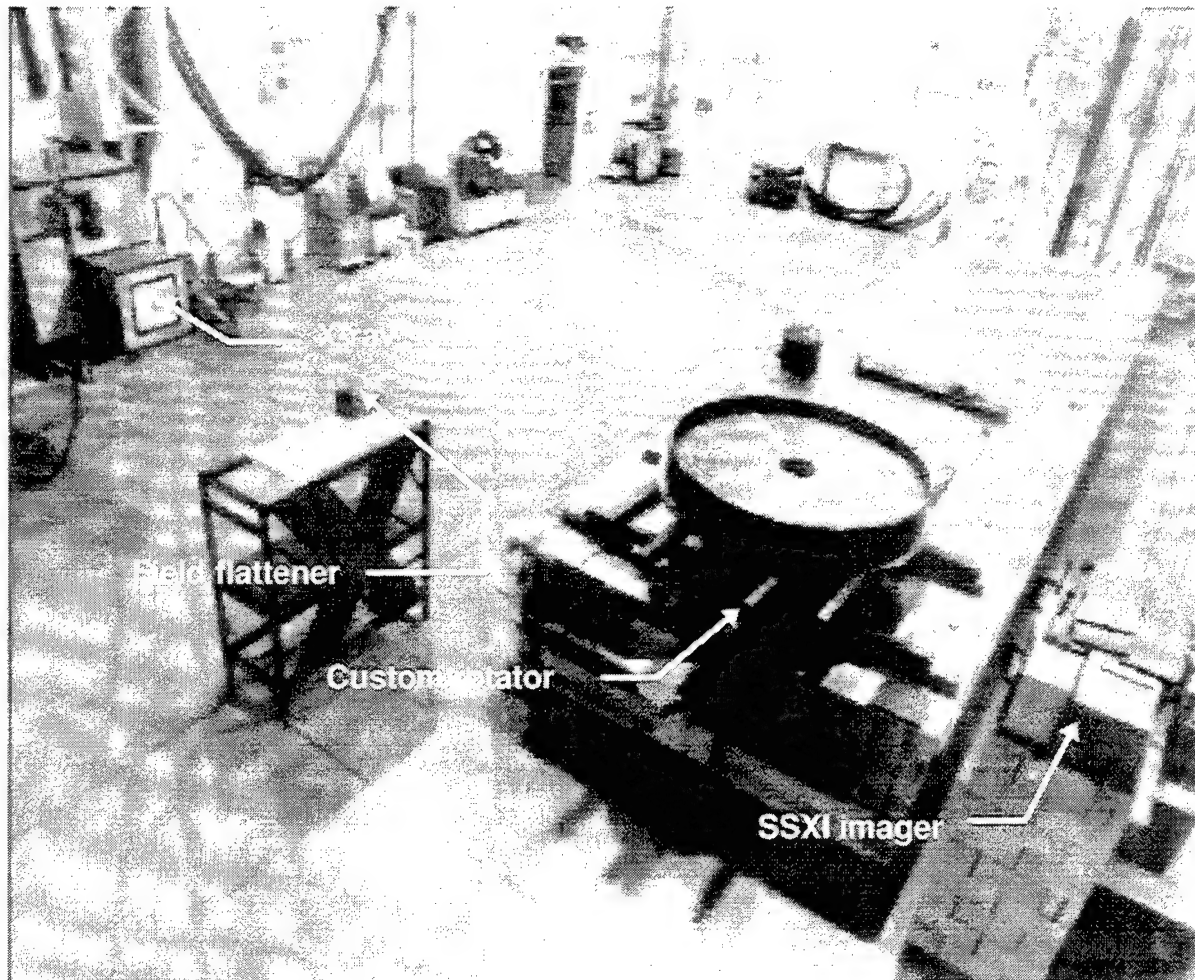


**Figure 9. The program's Lockheed SSXI imager and Isocon platforms.**  
These platforms were located in Alliant's RTIS facility and shared a common existing X-ray source and rotator mechanism.

#### 4.4.1 Experiment facility

All experiments were conducted in the RTIS facility located in Building 2492 of Alliant's Magna, Utah facility. SRMs up to 3 m in diameter by 10.5 m in length are routinely inspected in this facility for critical defects. This facility provides a Varian L-6000A HRO Linatron (15 MeV, 13,500R/min/m), a multiaxis manipulator, and two SAIC-built imagers, including a tangent imager typically used for the real-time evaluation of bondlines. The manipulator includes remote x-y-z position control for the X-ray source and the tangent camera, as well as rotation control for horizontally-mounted Titan SRMU segments. The RTIS is designed to autonomously acquire and store tangent RTR images over a pre-planned program of axial/angular/radial locations. Except for the experiment involving the SRMU segment, the SRMU rotator was not used. Rather, the project's custom rotator was employed. The facility's large air pallet system provided a convenient place to position the custom rotator, enabling it to be easily moved in and out of the X-ray beam. In this case,



either the LMSC camera was positioned on a temporary pedestal or the Isocon camera mounted on the RTIS manipulator. The facility is shown in Figure 8 and Figure 9 in its normal and SSXI configurations, respectively.

#### 4.4.2 Imagers

As part of our evaluation of RTR imager technology, and as part of the HR3DCT validation experiments, we used two existing RTR imagers. One of these is in routine production use inspecting Air Force SRMs: an Isocon-based imager, located at Alliant's Titan radiographic inspection facility. The other was built by Lockheed Martin based on a design developed previously by them for the Air Force at Wright Patterson AFB. This imager embodies the best high-energy RTR imager hardware available at the time. It too was used in Alliant's Titan radiographic inspection facility.

**Table 3**  
**Characteristics of the program's test platform imagers.**

| Imager             | Technology   | Spatial resolution | Contrast sensitivity | Dynamic range |
|--------------------|--|--------------------|----------------------|---------------|
| SSXI (primary)     | 25 cm LKH-5 radioluminescent glass optically coupled via a front-surface mirror to a CCD 1024x1024 camera  | 2 lp/mm            | 0.2%                 | 9500:1        |
| Isocon (secondary) | 25 cm GOS on tungsten substrate, optically coupled via a front-surface mirror to an Isocon 512x512 camera. | 0.7 lp/mm          | 1%                   | 200:1         |

Characteristics of the two imagers appear in Table 3. The spatial resolutions of these imagers enabled the breadboard to reconstruct with radial resolution significantly better than conventional CT. These secondary platforms provided real-world variations in HR3DCT algorithm inputs, and the opportunity to compare HR3DCT results with a variety of currently-deployed NDE techniques. We describe each imager in the following paragraphs.

##### 4.4.2.1 The Lockheed SSXI imager

The Lockheed SSXI imager was developed by Lockheed based on two Air Force contracts sponsored by the NDE branch of the Materials Directorate at the Wright Laboratory (WL/MLLP) at Wright Patterson AFB: *High Resolution Real-Time X-ray Radiography Advanced Development (HRRTR)*, contract F33615-91-C-5623, and *Solid State X-Ray Imaging Methodology (SSXI)*, contract F33615-89-C-5617. It is based on superior X-ray conversion and solid state camera technologies, as illustrated in Figure 10 and Figure 11.

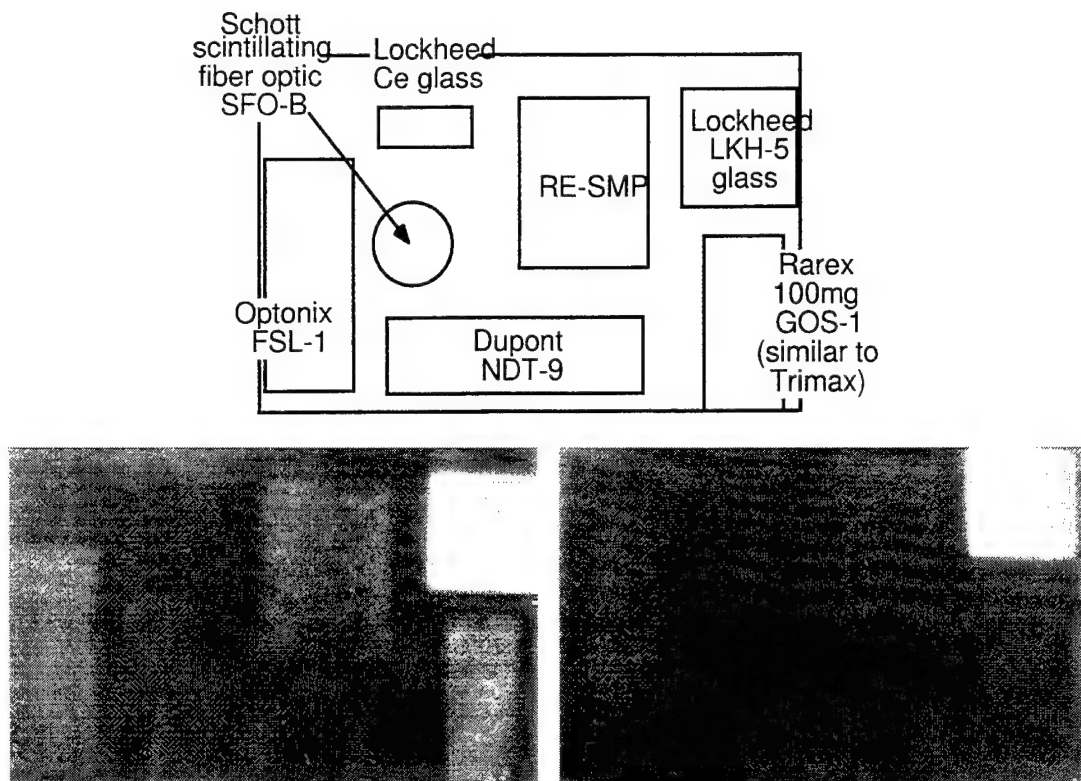


**Figure 10. The Lockheed SSXI imager's LKH-5 X-ray converter efficiency.**  
 The LKH-5 converter is much more efficient than competing technologies. A set of converter samples was arranged as shown in the upper diagram. The LKH-5 sample (the bright upper-right sample in the two images) produced much more light than competing converters, especially in the HR3DCT energy range (right).

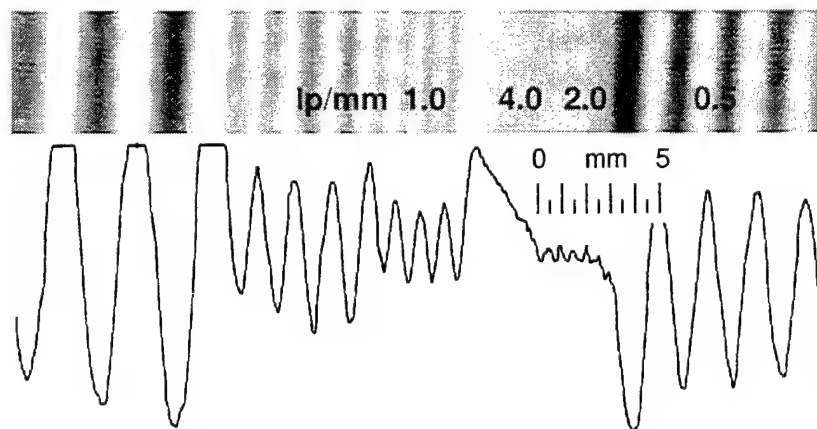


**Figure 11. The LKH-5 X-ray converter resolution.**  
 The converter's resolution approaches 2.0 lp/mm at 9 MeV, as required for HR3DCT imaging.

Results of our characterization of the SSXI imager are described in Section 5.1



#### 4.4.2.2 The Isocon imager

The Isocon imager is a 512-line system built specifically for high-energy (15 MeV) imaging of large SRMs. Although over ten years old, this design has been very successful, having been used in routine support of the C4, D5, Pershing, Peacekeeper, Delta II and Pegasus programs. The imager's X-ray converter is based on tungsten-backed GOS technology. The Isocon-camera is attached to a Penn Video controller that provides analog shading corrections. These analog corrections were used to reduce digitizer dynamic range requirements (this required careful compensation in the preprocessing). In general use, this imager is capable of resolving 0.7 lp/mm, and has a practical dynamic range of about 200. It routinely achieves penetrameter sensitivities approaching 1%-1T when imaging large SRMs. Not intended as a quantitative device, this imager's non-ideal characteristics are troublesome, but understood.

To use the Isocon imager for HR3DCT imaging, we either connected to its controller's RS-170 output signal through a video A/D incorporated in the breadboard workstation or used the RTIS image acquisition system (taking digitized files as output).

#### 4.4.3 Custom rotator hardware

A rotator was built to enable controlled manipulation of various test objects. The rotator was capable of supporting and rotating ten foot diameter loads of up to 2500 pounds in 0.1-degree ( $\pm 0.05$  degree) increments under workstation control. It is seen in Figure 9. This rotator's radial runout was less than 0.1 mm — equivalent to many RTR rotators — but its axial runout was larger than typical.

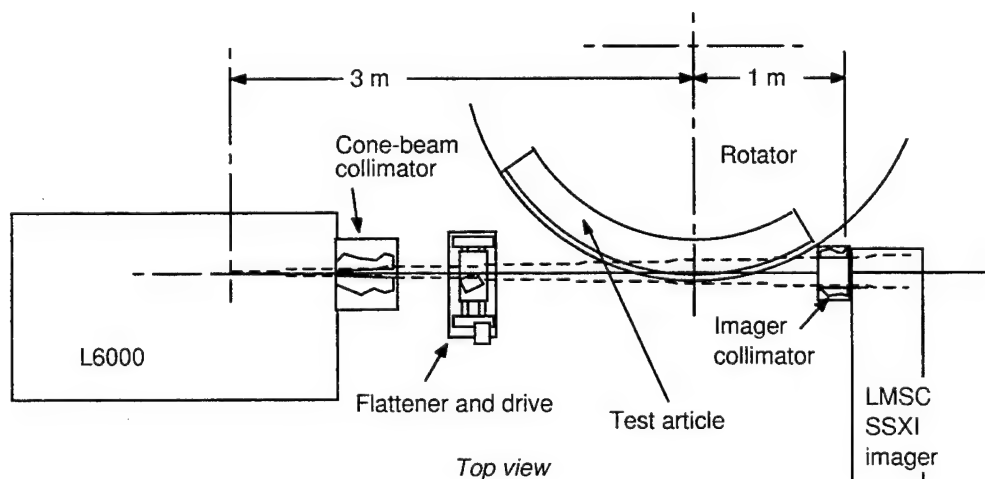


Figure 12. General radiographic layout used in experiments.

#### 4.4.4 Radiographic hardware additions to the platforms

HR3DCT imposes a few requirements not normally satisfied by most RTR or CT facilities. These requirements pertain to overall geometry, scatter control (collimation), and field flattening. The issues were quantitatively explored during Task 1. Those results were then

incorporated into the design of Task 2. This design was similar to that depicted in Figure 12. Our approach to the design of the various radiographic elements is presented in Table 4.

**Table 4**  
**Approach to design of radiographic elements.**

| Item                               | Approach   |
|------------------------------------|--|
| Geometry                           | The overall geometry was approximately that shown in <b>Error! Reference source not found..</b> The actual geometry used with each experiment was determined by Task 1 results and the constraints of the platform. Principal geometry-influencing factors included flux management, scatter management, imager dynamic range minimization, maximizing resolution, and minimizing acquisition time. Specifics of these issues are discussed in Section 5.2.  |
| Source collimator                  | Linatrons provide mounts for source collimation hardware. A source collimator absorbs incident X-rays not on a direct path to the imager's screen. This is generally necessary, since rays outside this region can perform no useful measurement function, but may scatter onto the detector, increasing measurement noise. The RTIS facility's Linatron had a remotely-adjustable source collimator.  |
| Flattener and flattener positioner | <p>A flattener inserts statically-positioned attenuative material to the beam path to make the nominal attenuation across the entire image as nearly constant as possible. Based on Task 1 results, we selected a flattener design suitable for SRM cylinder and dome use. Our flattener design accommodates typical motor component geometry variations in these areas. It is a machined shape of simple geometry (e.g., a lead prism).</p> <p>We also used a small translation table to enable remote positioning of the flattener. This unit was manually controlled from the breadboard workstation during the set up for each experiment.</p> <p>While flatteners were tried in most cases, it was concluded that flatteners are required only with SRMs having metallic cases.</p> |
| Detector scatter control hardware  | One of the goals of Task 1 was to determine whether post-collimation or another form of detector scatter control is necessary. It was determined that, because of the smallness of the scatter angle at these energies, the only real scatter control option is increase of the SID/SOD ratio. This approach was used in Task 2.   |

#### 4.4.5 Breadboard workstation details

The breadboard workstation provided capability for acquisition control, reconstruction, and data analysis. This flexibility was facilitated by our selection of AVS™ as the framework on which to build the breadboard workstation software. AVS provides a graphical user interface in which various processing modules are interactively selected and combined into more complex algorithm networks. These networks are, in essence, application programs which can do complex data analysis, processing and display. They can be saved and reused. Elements of the workstation functionality are discussed in the ensuing paragraphs.

##### 4.4.5.1 Real-time coordinated motion control and image acquisition

The breadboard required image acquisition capability so that the various imager and radiographic studies could be performed, and so that the data sets used in validation and ERA evaluation could be measured. Acquisition control differed for the two imagers used in this program, but was provided by means of a separate PC that served as an acquisition server to the workstation.

- For the Lockheed SSXI imager, an imager-specific controller plugged directly into the acquisition server's EISA bus, providing memory-mapped image acquisition control and data access. Driver software for this controller was required.
- The Isocon-based imager interfaced to the acquisition server through an EISA-based Matrox video frame grabber/processor. This unit provided real-time frame grab and integration.
- The RTIS system (of which the isocon imager is normally a part) provides its own image digitization and storage capability. Used with the SRMU experiment, it was necessary only to provide a data path to the workstation.

It was also necessary to *coordinate* test article motion with imager acquisition. The RTIS facility provided this capability in conjunction with isocon camera use for the SRMU experiment. For SSXI and Isocon experiments a custom rotator was used. This rotator was controlled by the HR3DCT workstation's acquisition server, which implemented coordination with the image acquisition process. Control of the acquisition server was accomplished through a serial connection from the workstation. Data was deposited by the acquisition server on the workstation's hard drive via an Ethernet connection.

#### 4.4.5.2 Preprocessing computations

As the diagram below depicts, the HR3DCT imaging chain introduces several artifacts of measurement which must be removed prior to reconstruction. Many of these artifacts are also present in conventional CT. A few artifacts are introduced by RTR detector technology.

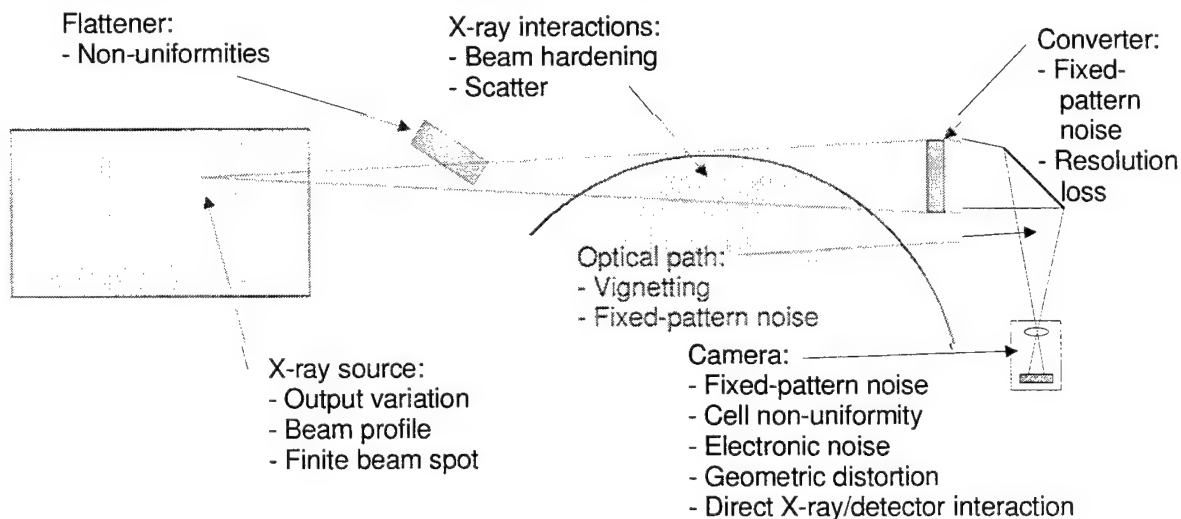


**Figure 13. Artifact sources in the HR3DCT imaging chain.**  
These artifacts must be removed during reconstruction preprocessing.

In previous work we examined these artifact processes — some theoretically, some through CT experience, and others in our HR3DCT modeling — and concluded that the important effects are reversible. Our specific approach to each imaging artifact is described in Section

5.1. In all preprocessing, raw measured data was preserved in its original (rather than transformed) state to enable modifications of correction strategies, if necessary.

#### *4.4.5.3 Reconstruction*

During Task 2, an existing HR3DCT reconstructor was implemented as a custom AVS module on the breadboard workstation. This algorithm reconstructs using the modified Feldkamp 3-D algorithm which was developed by Perceptics/Skiametrics in earlier HR3DCT work. This algorithm has several desirable properties, including good accuracy within the region around the midplane, equivalence to our PACT algorithm in the midplane case, ability to arbitrarily sample the reconstruction space, and potential for significant speedup on fast hardware in the eventual production implementation. Our AVS implementation of the reconstructor enabled its inputs and outputs to operate in concert with other existing and custom AVS tools. One key element of the modified reconstruction algorithm is its incorporation of *a priori* information that makes limited data set CT possible. The algorithm used by Perceptics in previous HR3DCT work relies on prior knowledge about the test article along a cylindrical surface. This algorithm has been very successful in both cylindrical and cone- or dome-like geometries.

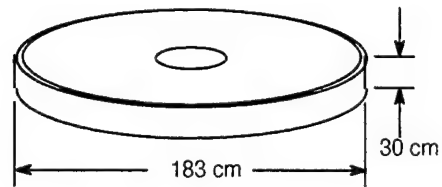
#### *4.4.5.4 Reconstructed data analysis/review operations*

The breadboard workstation's analysis and review capability was designed and built as minor extensions to AVS. AVS provides powerful capability for interactive display, manipulation, processing, and quantitative analysis of 2- and 3-D image data sets.

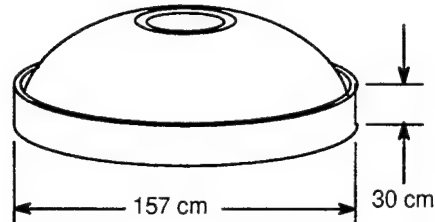
### **4.5 Test samples**

Four test articles were chosen for use in this project. Radiographic techniques, including conventional CT, behave differently when applied to objects of differing sizes, shapes and compositions. Thus, we are interested in examining HR3DCT's ability to properly image bondline defects in SRMs whose diameters range from 1.5 m to 3.0 m and whose cases may be built from composite materials or steel. The middle two test articles in Figure 14 each incorporated a series of reconfigurable artificial bondline anomalies. These anomalies were designed with widths over a range of sizes that brackets the expected detection limitations of the breadboard.

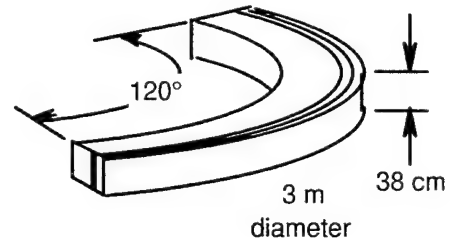
**CT phantom.** Insulated Kevlar case with inert propellant and a variety of synthetic bondline defects. Because its diameter allows conventional CT inspection comparative data are available. Used for ERA and HR3DCT comparison.



**Minuteman third stage dome.** Uninsulated section cut from a production case. Includes dome geometry. Synthetic bondline anomalies were inserted prior to filling with propellant simulant.



**Titan IV steel phantoms.** Insulated 10-mm and 20-mm thick steel cylinder sections. Synthetic bondline anomalies of various diameters and thicknesses were inserted prior to filling with propellant simulant. This article was too large for conventional CT.



**Titan SRMU graphite segment.** An insulated graphite production case. This article was too large for conventional CT.

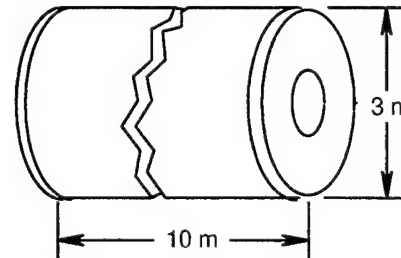


**Figure 14. Test articles.**

A range of test article sizes, shapes, and materials were used in the project for experiments and for validation.

## 5. EQUIPMENT CHARACTERIZATION RESULTS

In Task 1 of this project, several questions fundamental to the practical application of HR3DCT NDE were addressed. The results of Task 1 were reported in detail earlier<sup>16</sup> in this project, and will be summarized here along with additional information that has resulted from subsequent work. These results, together with the results reported in Section 6, form the basis for the Application Guide and the Conceptual Design of Sections 8 and 9, respectively.

### 5.1 Imaging issues

We experimentally explored non-ideal characteristics of RTR imagers as they pertain to HR3DCT data acquisition. Two categories of measurement were made: measurements of fundamental imager limitations, and measurements of reversible distortions. Measurements from the first category included X-ray conversion efficiency, resolution, dynamic range, information-destructive fixed-pattern noise, and imager-induced noise. Nothing can be done about these limitations; we must simply be aware of and design around them. These issues are presented in Table 5. Conversely, measurements from the second category facilitate compensation strategies. This category includes types of information-preserving fixed-pattern noise, and geometric distortion. These issues are presented in Table 6.

**Table 5**  
**Assessment of fundamental RTR imager limitations.**

| Item  | Description  | Discussion / measurement method  |
|---|--|--|
| Spatial resolution                          | The largest spatial frequency for which useful information can be obtained from the image.         | Expressed in terms of the modulation transfer function (MTF) of the imaging system. Measured a pair of Lockheed Martin manufactured high energy bar patterns made of alternating pieces of Lucite and tungsten of different thickness which present spatial frequencies from 0.2 lp/mm to 4.0 lp/mm. Another quantitative MTF measurement was computed by Fourier analysis of the edge response of the system.   |
| Dynamic range                               | Ratio of the maximum usable signal level to the readout noise level. Excludes fixed-pattern noise. | A sequence of image pairs is taken at gradually increasing exposure levels. The pixel noise in the difference images is the RMS combination of readout noise and quantum statistical noise. At lowest exposure levels, system noise dominates. Above that, in the camera's linear range, the quantum statistical part of the total noise grows as the square root of the exposure level. At higher exposure levels, the RMS pixel noise falls short of an extrapolation of the linear exposure data. This shortfall is due to camera saturation. It marks the practical upper limit to useful exposures. |
| Information-destructive fixed-pattern noise | Non-random intensity distortions which cannot be corrected.  | A pair of images of a relatively flat field is made with differing exposure levels near the extremes of the imager's linear range. The computed difference should be a non-zero constant to within random noise. Areas where the difference is near zero are defective, and must be dealt with either by correcting the cause or interpolating across the defective region.  |

<sup>16</sup> Youngberg, J.E., and Burstein, P., *High-Resolution Three-Dimensional Computed Tomography Interim Report*, submitted to Wright Laboratory, Wright-Patterson AFB under Air Force contract F33615-93-C-5327, January 1995.

|                      |  |  |
|----------------------|--|--|
| Imager-induced noise | Random noise introduced by the camera. | This parameter is a by-product of the dynamic range measurement procedure described above. |
|----------------------|--|--|

**Table 6**  
**Assessment of reversible RTR imager limitations.**

| Item                           | Description   | Discussion / measurement method  |                   |               |  |  |  |  |          |  |  |  |  |  |                |  |  |                                |  |  |                   |  |              |  |  |   |  |                  |  |   |   |  |                       |   |  |  |  |                          |   |  |  |   |                          |   |   |   |  |
|--------------------------------|---|--|-------------------|---------------|--|--|--|--|----------|--|--|--|--|--|----------------|--|--|--------------------------------|--|--|-------------------|--|--------------|--|--|---|--|------------------|--|---|---|--|-----------------------|---|--|--|--|--------------------------|---|--|--|---|--------------------------|---|---|---|--|
| Reversible fixed-pattern noise | Additive or multiplicative intensity field distortions, including a CCD camera dark current, X-ray converter, optical path, camera gain variations, optical aperture-induced vignetting, imager light or X-ray leaks, and fixed-pattern EMI. Linatron beam profile and flattener effects can also be considered part of this category | <p>The distortions fall into the five groups shown on the left side of the chart below. The chart shows the setup for measuring a series of images from which various distortions can be isolated.</p> <table><tr><td></td><td colspan="4">Aperture open</td></tr><tr><td></td><td colspan="4">Xrays on</td></tr><tr><td></td><td></td><td colspan="3">SRM &amp; flattner</td></tr><tr><td><u>Noise source to isolate</u></td><td></td><td></td><td colspan="2">Flat illumination</td></tr><tr><td>Dark current</td><td></td><td></td><td>✓</td><td></td></tr><tr><td>X-ray leaks, EMI</td><td></td><td>✓</td><td>✓</td><td></td></tr><tr><td>Ambient light (leaks)</td><td>✓</td><td></td><td></td><td></td></tr><tr><td>Internal gain variations</td><td>✓</td><td></td><td></td><td>✓</td></tr><tr><td>External gain variations</td><td>✓</td><td>✓</td><td>✓</td><td></td></tr></table> <p>Measurements were used in a process to minimize noise due to dark current , X-ray leaks, ambient light leaks prior to estimation of the residual effects.</p> |                   | Aperture open |  |  |  |  | Xrays on |  |  |  |  |  | SRM & flattner |  |  | <u>Noise source to isolate</u> |  |  | Flat illumination |  | Dark current |  |  | ✓ |  | X-ray leaks, EMI |  | ✓ | ✓ |  | Ambient light (leaks) | ✓ |  |  |  | Internal gain variations | ✓ |  |  | ✓ | External gain variations | ✓ | ✓ | ✓ |  |
|                                | Aperture open   |  |                   |               |  |  |  |  |          |  |  |  |  |  |                |  |  |                                |  |  |                   |  |              |  |  |   |  |                  |  |   |   |  |                       |   |  |  |  |                          |   |  |  |   |                          |   |   |   |  |
|                                | Xrays on  |  |                   |               |  |  |  |  |          |  |  |  |  |  |                |  |  |                                |  |  |                   |  |              |  |  |   |  |                  |  |   |   |  |                       |   |  |  |  |                          |   |  |  |   |                          |   |   |   |  |
|                                |   | SRM & flattner   |                   |               |  |  |  |  |          |  |  |  |  |  |                |  |  |                                |  |  |                   |  |              |  |  |   |  |                  |  |   |   |  |                       |   |  |  |  |                          |   |  |  |   |                          |   |   |   |  |
| <u>Noise source to isolate</u> |   |  | Flat illumination |               |  |  |  |  |          |  |  |  |  |  |                |  |  |                                |  |  |                   |  |              |  |  |   |  |                  |  |   |   |  |                       |   |  |  |  |                          |   |  |  |   |                          |   |   |   |  |
| Dark current                   |   |  | ✓                 |               |  |  |  |  |          |  |  |  |  |  |                |  |  |                                |  |  |                   |  |              |  |  |   |  |                  |  |   |   |  |                       |   |  |  |  |                          |   |  |  |   |                          |   |   |   |  |
| X-ray leaks, EMI               |   | ✓  | ✓                 |               |  |  |  |  |          |  |  |  |  |  |                |  |  |                                |  |  |                   |  |              |  |  |   |  |                  |  |   |   |  |                       |   |  |  |  |                          |   |  |  |   |                          |   |   |   |  |
| Ambient light (leaks)          | ✓   |  |                   |               |  |  |  |  |          |  |  |  |  |  |                |  |  |                                |  |  |                   |  |              |  |  |   |  |                  |  |   |   |  |                       |   |  |  |  |                          |   |  |  |   |                          |   |   |   |  |
| Internal gain variations       | ✓   |  |                   | ✓             |  |  |  |  |          |  |  |  |  |  |                |  |  |                                |  |  |                   |  |              |  |  |   |  |                  |  |   |   |  |                       |   |  |  |  |                          |   |  |  |   |                          |   |   |   |  |
| External gain variations       | ✓   | ✓  | ✓                 |               |  |  |  |  |          |  |  |  |  |  |                |  |  |                                |  |  |                   |  |              |  |  |   |  |                  |  |   |   |  |                       |   |  |  |  |                          |   |  |  |   |                          |   |   |   |  |
| Geometric distortions          | Mislocation of image information in the digitized image   | A plate embedded with a precision array of high-z spheres was imaged so that the distortion field could be assessed. No geometric corrections were made.   |                   |               |  |  |  |  |          |  |  |  |  |  |                |  |  |                                |  |  |                   |  |              |  |  |   |  |                  |  |   |   |  |                       |   |  |  |  |                          |   |  |  |   |                          |   |   |   |  |

Measurements were made during Task 1 and Task 3 experiments. Results of the analyses of these measurements were used as inputs to the breadboard design and, ultimately, to performance projections.

A summary of the imager experiments and results is presented in the following paragraphs. Details are reported in Appendix C of the project's Interim Report<sup>16</sup>.

#### 5.1.1 Spatial resolution

The spatial resolution measured was the composite resolution of the entire imager. This was achieved using the bar pattern shown in Figure 15. Because the pattern was carefully positioned next to the X-ray converter screen, virtually no geometric unsharpness was present. The experiment and data are described in the Interim Report. The basic result is that the 2.0 lp/mm pattern was distinguishable, but only slightly modulated. A more detailed discussion is given in the Interim Report<sup>16</sup>.



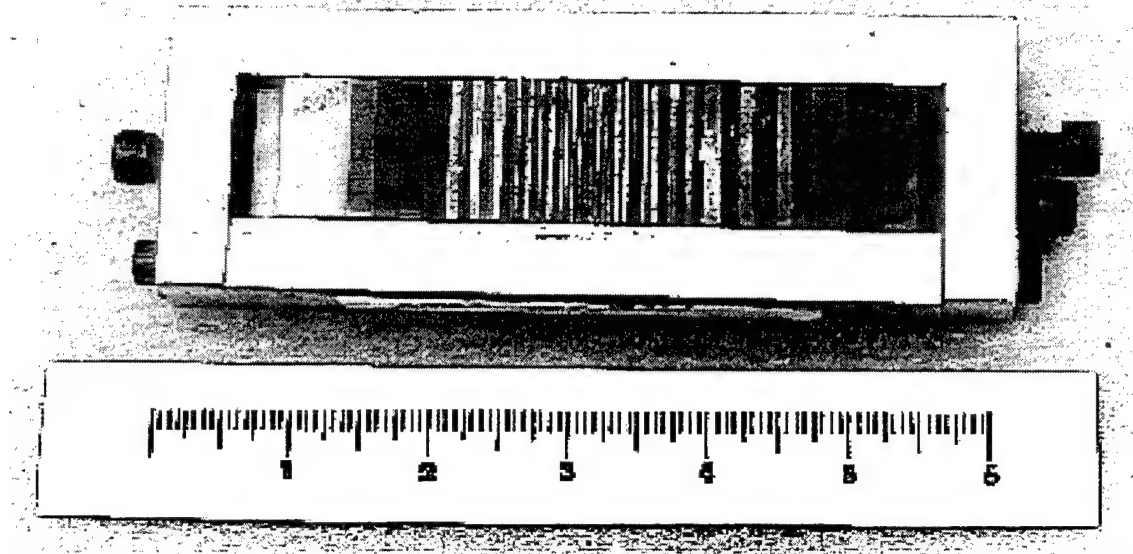


**Figure 15. A bar pattern device used to measure spatial resolution.**

The device is actually a sandwich of plastic and tungsten plates, arranged in such a way that modulation produced by spatial frequencies of 4.0, 2.0, 1.0, 0.567, 0.5, 0.33, 0.25, 0.16, 0.11, and 0.08 lp/mm can be measured.

### 5.1.2 Dynamic range

The dynamic range is defined as the ratio of the maximum usable signal level to the readout noise level. This parameter is significant due to the large absorptions associated with large SRM HR3DCT tangent projections. For example, a 0.2-mm case/insulator separation in a 3-m diameter SRM having various steel case thicknesses will produce local signal changes as shown in Table 7.

**Table 7**  
**Dynamic range of a 1.5-m steel SRM projection.**

| Steel case thickness<br>(mm) | Signal change as a fraction of<br>unattenuated signal level | Implied<br>dynamic range |
|------------------------------|---|--------------------------|
| 6.35                         | 0.01%   | 10,000                   |
| 12.7                         | 0.003%  | 30,000                   |
| 19                           | 0.0003%   | 300,000                  |
| 25.4                         | 0.00003%  | 3,000,000                |

Inadequate imager dynamic range will force either clipping of higher signal levels, or loss of the low-level signal details in which anomaly information is found. The SSXI imager was found to have a real dynamic range of about 9500. The Isocon-based camera, of course, has far less dynamic range. It is believed to be about 200, though our measurements did not permit reliable quantification. The clear implication of these experiments is that field flattening is required for HR3DCT of Titan and Space Shuttle steel segment cases. Composite cases have far less attenuation, and do not require field flattening, as demonstrated by our successful reconstruction of a composite SRMU and a C4 phantom using data from the Isocon-based camera.

### 5.1.3 Linearity

Linearity directly affects the quantitative fidelity of CT reconstruction. An imager's composite linearity can be measured using a set of known absorbers (Figure 16. Stepped absorbers used to measure composite linearity.). For an imager that performs *analog* signal integration, linearity of the imager's camera can be measured by carefully controlling integration time. Both methods were used with the SSXI imager, with the results described in the Interim Report<sup>16</sup>. We conclude that the SSXI imager is linear within the error limits of our experimental procedure, and that it is acceptable for the purposes of CT reconstruction. The isocon imager is known not to be linear.

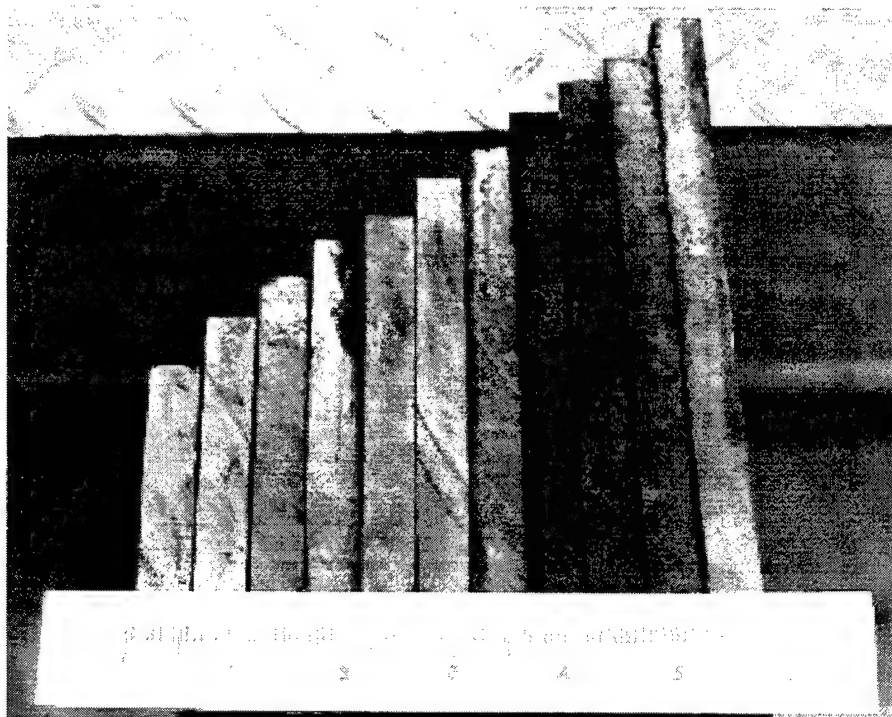


**Figure 16. Stepped absorbers used to measure composite linearity.**

### 5.1.4 Contrast sensitivity

In the context of radiographic use, an imager's contrast sensitivity is a measure of the smallest change of absorbing material that produces a measurable radiographic projection change. This parameter is typically a function of absorption. It is measured using a combination of small and large absorbers. The detailed procedure for estimating contrast sensitivity in our experiments is discussed in Appendix C of the Interim Report<sup>16</sup>. For steel absorbers 10 and 18.8 cm thick, the values measured for the SSXI imager were 0.2% to 0.4%. The overall radiographic contrast sensitivity parameter depends on many factors, some of which can be controlled. It can be traded against other performance measures, such as resolution and scatter. Similar tradeoffs are a primary design task in any HR3DCT implementation.

### 5.1.5 Imager-induced noise

Sources of noise associated with the imager itself include the imager camera's fixed CCD dark current and cell-to-cell CCD gain variations, imperfections in the imager's X-ray conversion screen, and light scattered within the imager enclosure. The first two of these are easily measured and corrected. The last two can be detected, but may not always be reversible. In addition, the camera introduces a random noise component that is always present and often reducible, but irreversible. These effects were assessed for the SSXI imager using various combinations of X-rays on/off, shutter open/closed, and absorber absent/present. These measurements lead to the following conclusions.

- The normal method for correcting dark current and fixed-pattern gain variations drives these effects beneath the random noise component.
- The inherent random noise introduced by the camera is about 0.01% of the camera's full range
- Afterglow from the X-ray conversion glass is about 0.01% — similar to inherent noise.
- No evidence of irreversible X-ray conversion screen artifacts was observed. Such effects as exist are corrected by the normal gain normalization.
- Direct X-ray hits on the camera's CCD can result in both momentary non-linear image artifacts, and temporary CCD damage (which heals over several hours).
- Visible light scatter within the imager accounts for a small, but significant, signal-dependent, long-wavelength noise component. Moving the X-ray conversion screen away from the imager's mirror reduced this problem, but additional distance would have improved results.

### 5.1.6 Imager shielding observations

A final RTR camera characteristic of interest is the imager's sensitivity to direct hits (X-rays, both direct and scattered, that unintentionally find their way to the camera's light-to-signal converter). This characteristic is of special interest in large SRM HR3DCT because the use of high-energy X-rays at maximum possible flux makes complete shielding of the camera impractical. The view artifacts that result are random events that result in information loss. While their effects can be reduced through view conditioning processing (Section 5.5), elimination of their cause is a superior approach. Our shielding strategy for the SSXI imager included the SRM itself as shielding for the imager, overlapping lead plates on the top and sides of the imager (Figure 17), a 1.9 cm sheet of lead inside the imager box on the X-ray side, a box of lead immediately surrounding the camera, and 5.1 cm leaded glass shield in the optical path.

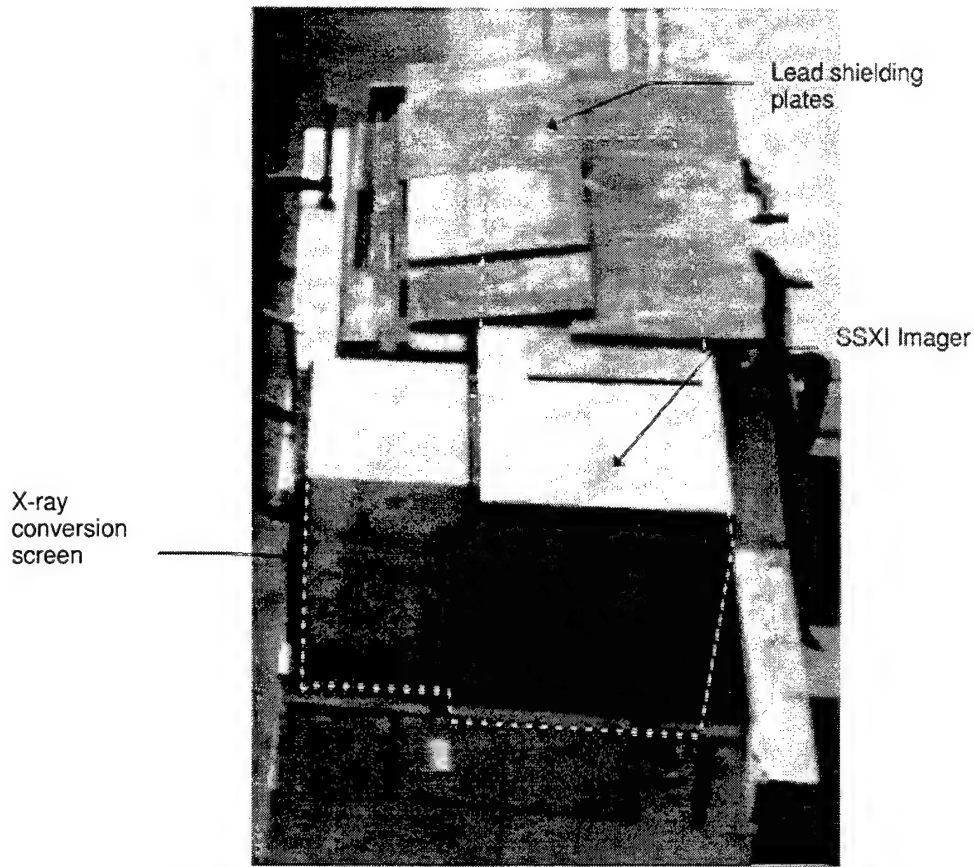


**Figure 17. The SSXI imager as set up for various experiments.**

The X-ray conversion screen is nearest, and faces left. The camera is in the section farthest away, and is shielded with carefully-overlapped lead plates on the left, top, right, and far sides.

Another important question related to shielding was the frequency and nature of direct X-ray interactions in the CCD camera. Direct hits must be minimized for two reasons. Most obviously, they increase the noise and artifact levels in reconstructed images. Secondly, they may result in permanent camera damage.

The Isocon-based camera's images seemed less affected by direct hits. This observation makes sense, since each Isocon hit effects only a single frame of the many whose average comprises each view.

## **5.2 Radiometric issues**

Another task, in addition to understanding imager characteristics, was to experimentally quantify various radiographic factors which affect HR3DCT data acquisition (initial consideration was undertaken in previous work<sup>17</sup>). Again, variables that affect the quality of radiographic images fall into two groups: those which are beyond our control (to which we must simply adapt) and those that we can control. The first group includes X-ray beam focal spot size and shape, variations of beam intensity within the detector's solid angle, and the nominal geometry and materials comprising the test article.

<sup>17</sup>Youngberg, pp. 31-32.

**Table 8**  
**Determination of fixed radiographic parameters.**

| Item                           | Description  | Discussion / measurement method   |
|--------------------------------|--|---|
| Focal beam spot size and shape | Dimensions of the elliptical X-ray origin; limits image resolution; effects can be controlled by SOD/SDD ratio | The finite beam spot casts a penumbral shadow which acts like a low-pass filter. Unfortunately, the amount of blurring which results depends on the position of the feature being imaged within the test article. Thus, correction is impossible. The beam spot size is known accurately enough to facilitate HR3DCT performance projections, so measurement was unnecessary. |
| Linatron output variation      | The total X-ray flux generated during a particular interval varies slightly.                                   | Because this is a random variable, it cannot simply be measured and corrected. Rather, the Linatron output must be measured during each view acquisition. In conventional CT a beam monitoring detector is used for this purpose. We used a subarea of the imager outside the shadow of the test object for this purpose, correcting for the additive scatter component.      |
| Beam profile                   | Monotonic decrease in X-ray beam intensity as one moves away from its centerline.                              | Measurable (once imager characteristics are known) by direct exposure of the imager to the X-ray beam. In practice, measurement of the beam profile can be combined with the flattener profile. In fact, both these measurements were combined with the imager fixed-pattern measurements discussed in the previous section.  |

The second group — factors over which we have some control — includes the X-ray energy, the source to object distance (SOD), the source to imager distance (SID), X-ray scatter, and the specific controlling factors (e.g., compensator/flatteners and collimators) that can be customized to the needs of each facility.

**Table 9**  
**Approach to optimization of radiographic configuration.**

| Item  | Description  | Discussion / results  |             |               |  |  |  |        |         |             |                  |   |   |   |                    |   |   |  |
|---|--|---|-------------|---------------|--|--|--|--------|---------|-------------|------------------|---|---|---|--------------------|---|---|--|
| X-ray energy  | Determines penetration of large SRMs                                       | Large SRM imaging generally needs all the energy and intensity available. The effects of decreased energy (and hence intensity) are well-understood. No measurement was required.   |             |               |  |  |  |        |         |             |                  |   |   |   |                    |   |   |  |
| Source-to-object distance (SOD) and source-to-imager distance (SID) | Determines magnification, available signal, scatter, and image unsharpness | <p>The objective in this area was to vary the SOD/SDD (SDD constant) and SDD (SOD/SDD constant) to quantify relationships among dependent parameters. Dependencies follow:</p> <div><div><div>More, better</div><div>↕</div><div>Less, worse</div></div><table><tr><td></td><td colspan="3">Magnification</td></tr><tr><td></td><td>Signal</td><td>Scatter</td><td>Unsharpness</td></tr><tr><td>Increase SOD/SDD</td><td>↓</td><td>↑</td><td>↓</td></tr><tr><td>Increase SOD &amp; SDD</td><td>↓</td><td>↓</td><td></td></tr></table></div> <p>Conclusions about tradeoffs among these tendencies are drawn in the remainder of this section.</p> |             | Magnification |  |  |  | Signal | Scatter | Unsharpness | Increase SOD/SDD | ↓ | ↑ | ↓ | Increase SOD & SDD | ↓ | ↓ |  |
|   | Magnification  |   |             |               |  |  |  |        |         |             |                  |   |   |   |                    |   |   |  |
|   | Signal   | Scatter   | Unsharpness |               |  |  |  |        |         |             |                  |   |   |   |                    |   |   |  |
| Increase SOD/SDD  | ↓  | ↑   | ↓           |               |  |  |  |        |         |             |                  |   |   |   |                    |   |   |  |
| Increase SOD & SDD  | ↓  | ↓   |             |               |  |  |  |        |         |             |                  |   |   |   |                    |   |   |  |

|                          |  |  |
|--------------------------|--|--|
| Anti-scatter collimators | Control indirect radiation appearing at the imager; scatter can dominate signal in highly-attenuated areas | <p>It was found that the deterministic component of scatter is not a serious problem in HR3DCT. It introduces long-wavelength artifacts that are easily corrected or ignored. The random component is a far more important problem, since it can swamp real signal in areas where attenuations are large. Scatter is primarily controlled by SOD/SID optimization, where the ratio of scatter to direct signal is:</p> $\text{SDD}^2 / (\text{SDD} - \text{SOD})^2$ <p>Beyond this, collimation is the only alternative. The fan-beam collimation that is effectively used in conventional CT cannot be used here. Schemes involving detector collimator motion are too complex for practical use. Viable alternatives are limited to tight source and imager collimation.</p> |
| Compen-sator/flatteners  | Objects inserted in the X-ray path to control dynamic range and scatter.                                   | The dynamic range in our steel-case Titan IV test objects exceeded the capability of any existing 2-D imager. Therefore we used objects of known shape (flatteners) to roughly equalize absorption across the entire tangent. It was found that flatteners having a rectangular transaxial cross-section were very effective, but difficult to compensate accurately.  |

Measurements were made as part of Tasks 1 and 2 and subsequently analyzed. These analysis results were inputs to the performance projection tasks. A summary of the radiographic experiments and results is presented in the following paragraphs. Details are reported in Appendix D of the Interim Report<sup>16</sup>.

### 5.2.1 Scatter effects

As expected, the importance of scatter varies with the attenuation of the object being inspected. Projections using the C4 phantom proved to have adequate signal quality to produce good reconstructions. In this case, the attenuated beam is strong compared to the amplitude of scattered radiation. In the case of the steel Titan phantoms, however, the attenuation through the inner tangent of the steel case is so significant that the attenuated beam was fainter than the random component of the scatter signal. While the scatter reduces the intensity range of the observed signal, the faint change due to anomalies must still be measured. In other words, the signal-to-noise requirement is not reduced, while the noise of the measurement is increased by the square root of the factor by which scatter level is increased. In this situation, the alternatives to improving the signal-to-noise ratio of view measurements include: changing the SDD, the SDD/SOD ratio, and introducing scatter reduction shielding or filtering. It was the objective of the scatter effects measurements to quantitatively explore meaningful alternatives.

Scatter was measured using the two Titan phantoms. Measurements were made to quantify dependence on geometry. The conclusions from these experiments contain a few surprises, but most results were expected. The first result is that the noise due to scatter dominates the signal at the inner tangent of the steel in both Titan phantoms. As measured at the inner case tangent, the signal-to-noise ratio is at most 0.3 in the 9-mm phantom. While the 19-mm phantom appears to have a similar signal-to-noise ratio, the no-scatter extrapolation that leads to this conclusion has obvious problems that make it clear that the ratio could easily be a factor of ten worse. The signal-to-noise ratio in both cases is inadequate for HR3DCT

reconstruction. This conclusion underscores the necessity of introducing effective field flattening in the X-ray beam.

An unexpected behavior was observed in the 9-mm Titan phantom. Although scatter is forward-peaked at 16 MeV, the object-to-imager distance for our experiments suggests that scatter from the phantom will exhibit long-wavelength behavior. Thus, the relatively short-wavelength scatter component observed in 9-mm data was a surprise. Possible explanations for the existence of this phenomenon include (1) low-energy X-ray scatter originating in the conversion screen just outside the tangent, and (2) visible light scatter inside the imager which is most intense outside and near the tangent. Flattening hardware used in Task 2 was effective in achieving a significant reduction in this observed effect.

### 5.2.2 Flattener effectiveness

Prototype flatteners were tested to determine their effectiveness in reducing the dynamic range required in the Titan phantom measurements. The advantage sought in using a flattener is achieved by sharply reducing amplitude of the maximum transmitted signal, while not changing the amplitude of the minimum transmitted signal. This is done by artificially attenuating the beam in areas outside and near-inside the outer case tangent. The attenuating material — the flattener — is in place during measurement of the normalizing view, and is mathematically removed from each measured view as part of the view normalization process. The success of this approach depends on accurate measurement of both the normal view and the much-attenuated flattened views. With adequate integration the only problems in the flattened views result from the general amplitude of scatter and from changes in the scatter due to the flattener. The dynamic range of the normal view required special piecewise integration techniques. It was determined that the flattener normal view is difficult to measure and remove (due primarily to scatter).

## 5.3 Suitability of test objects

The Task 1 utilized four phantoms — the C4 and third-stage Minuteman dome phantoms, and two Titan-diameter steel phantoms (Figure 18). All but the last phantom produced results as expected. The 19-mm steel phantom did not yield either projection or reconstruction data reflective of the artificial separations it contained. In addition, the simulated cases of these phantoms, when reconstructed, revealed significant non-circularity. This latter feature, in preliminary reconstructions, may be responsible for artifacts inboard from the reconstructed case.



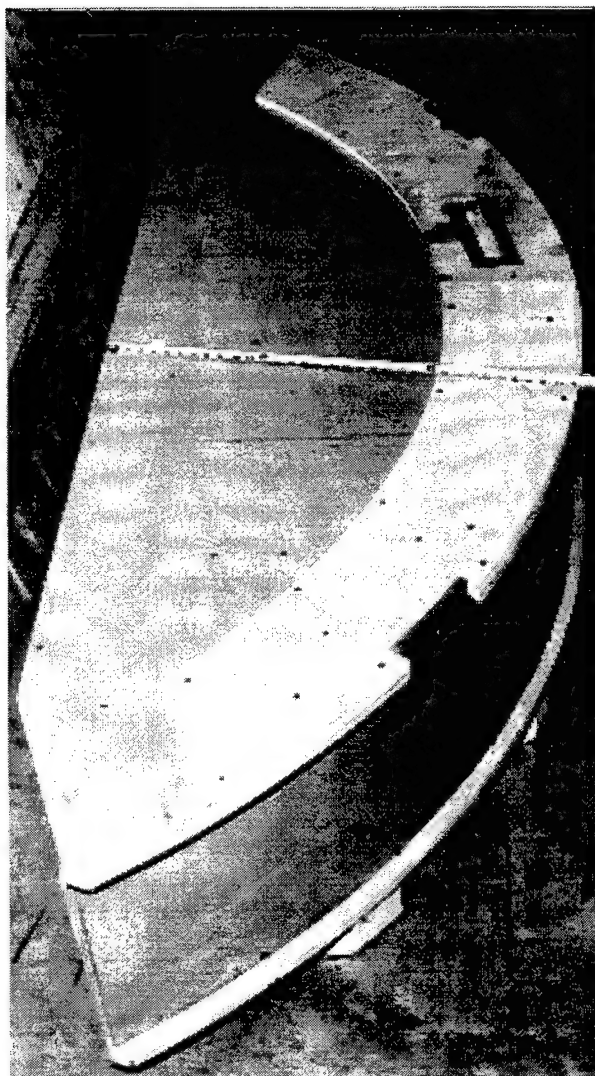


**Figure 18. One of the 3-m diameter steel phantoms.**

The design provided for reconfigurable separation simulators and replaceable propellant simulation. There were two large-diameter phantoms having 9-mm and 19-mm steel walls, respectively.

#### **5.4 Acquisition**

Acquisition time varies depending on X-ray exposure times. During these initial tests, SSXI exposure times varied from 4 to 35 sec. Image read out times were about 5 sec and disk storage time about 1 sec for a total acquisition time of 10 to 41 sec. Isocon-based exposure times were limited by a total of 16 bits of accumulation arithmetic (256 frames x 1/30 sec/frame = 8.5 sec), and required less than a second for disk storage. These acquisition times bracket the time per view required for reconstruction.

#### **5.5 Preprocessing computations**

As confirmed by our experiments, the HR3DCT imaging chain introduces several artifacts of measurement which must be removed prior to reconstruction. The source of each is depicted in Figure 13.

We previously examined these artifact processes theoretically, through CT experience, and by modeling, and concluded that the important effects are reversible. Our observations and approach relative to each imaging artifact is described in Table 10.

**Table 10**  
**Imaging chain artifacts, observations and approaches.**

| Artifact                         | Observations  | Approach   |
|----------------------------------|---|--|
| Beam hardening                   | Not directly observed in experiments. Normally introduces long wavelength components in the reconstruction.   | Not an issue for large steel SRMs, since the steel hardens the beam in the outer few tenths of tangent. Little or no effect expected for composite cases, since all projections share similar geometry.  |
| Scatter                          | See Radiographic Experiment Results, Section 5.2.1  | No compensation used, although long-wavelength rough correction is possible.   |
| Flattener nonuniformities        | No fine-scale nonuniformities detected. The shape of the flattener itself must be removed. This is complicated by the interaction of the flattener's scatter and the SRM.   | Our approach treats the flattener similar to multiplicative fixed-pattern noise. This should properly compensate any fine-scale nonuniformities, as well as the gross flattener shape, but does not accurately take into account flattener-induced scatter. Again, this is long-wavelength, and should produce minor effects.  |
| Fixed pattern converter noise    | X-ray converter noise insignificant. There were no nonlinear effects.   | Any effects should be properly compensated by treating them as multiplicative fixed-pattern noise.   |
| Linatron output variations       | A variation in Linatron output was observed over durations of seconds and of many minutes. Variations were especially evident at points where a modulator fault necessitated Linatron restart. Note that such variations comprise a few percent change in signal. | Estimation of all variations is made simple by the observation that the sum of direct and scattered radiation outside the tangent is proportional to the Linatron output (assuming little variation in SRM absorption as it is rotated). Assuming the imager is operating in its linear region, the region outside the tangent was used as a beam monitor, producing a DC component in a fixed-pattern noise correction. |
| Linatron beam profile            | The effect is large.  | Properly compensated by treating this effect as multiplicative fixed-pattern noise.  |
| Finite beam spot                 | This is a major driver of the flux/resolution vs. scatter tradeoff that is made when establishing the SID and SOD.  | As a result of measurements, the SID/SOD ratio was minimized, knowing that scatter was also greatly increased, but that its general effects were benign.   |
| Vignetting                       | The effect is significant and similar to the Linatron's beam profile.   | Properly compensated by treating this effect as multiplicative fixed-pattern noise.  |
| Fixed-pattern optical path noise | The imager was relatively free from light leaks, and all optical components were clean, with the result that optical path noise was observed only at the level of random camera noise.  | No correction was utilized.  |
| Fixed-pattern camera noise       | Efforts to estimate and correct fixed-pattern camera noise were successful to within random camera noise levels.  | The correction image was estimated with everything but the SRM in place, the shutter open, and the Linatron at operating output. The correction was applied multiplicatively after subtractively removing the bias image from both the correction image and each view.   |

|                    |   |   |
|--------------------|---|---|
| Electronic noise   | See Imager Experiment Results, Section 4.   | Reduction of electron noise in SSXI data is possible only at the expense of resolution. In some applications and geometries, axial averaging was very effective.  |
| Spatial distortion | There is no important distortion.   | No plan exists to correct distortion.   |
| Direct hits        | Frequent and occasionally producing persistent CCD damage; less destructive in isocon data. | Two approaches were undertaken. In the first, multiple images were acquired at a single view position, enabling individual pixels to "vote". In the second, constraints were enforced on single-pixel excursions. |

## 6. HR3DCT RESULTS

A significant part of Task 2 was the series of experiments involving HR3DCT imaging of our full scale test objects. The test objects were briefly described in Section 4.5 and depicted in Figure 14. In this section we describe our results, including both projection data and the associated HR3DCT reconstructions. A careful analysis is made of each result. Note that all reconstructions shown in this section are planer sections from solid volumes. Because coordinate frame conventions vary, careful attention should be given to descriptions and axis labels accompanying the figures.

### 6.1 C4 phantom

The C4 phantom was constructed as a test object for conventional SRM CT. It contains a variety of interesting objects, four of which are within several cm of the outer surface. Those close enough to the outer edge to image using HR3DCT are propellant crack simulators. The simulated cracks are about 51 mm in circumferential extent and of unknown axial extent. The cracks appear to have been created by forcing a thin chisel-like instrument into the inert propellant into the phantom's upper surface. Aluminum shim material has been forced into each crack to an unknown depth. The cracks are located roughly 15 degrees apart.

The reconstruction in Figure 19 represents a 140-degree section of a 2.5 cm wide transaxial annulus encompassing the outer diameter of the C4 phantom. The curvature in what should be the outer edge of the Kevlar case is due to the eccentricity of the phantom and the rotator. The case is roughly constant thickness, but the reconstruction clearly reveals that the insulator varies in thickness by as much as a factor of two. The simulated cracks are seen to be roughly parallel to the insulator/propellant interface about one to two mm into the propellant. Each crack is clearly seen to be open at its ends, with the middle portion obscured by the aluminum shims. Analysis suggests that the ends of the cracks, on either edge of the aluminum, are open by perhaps 0.2 mm.

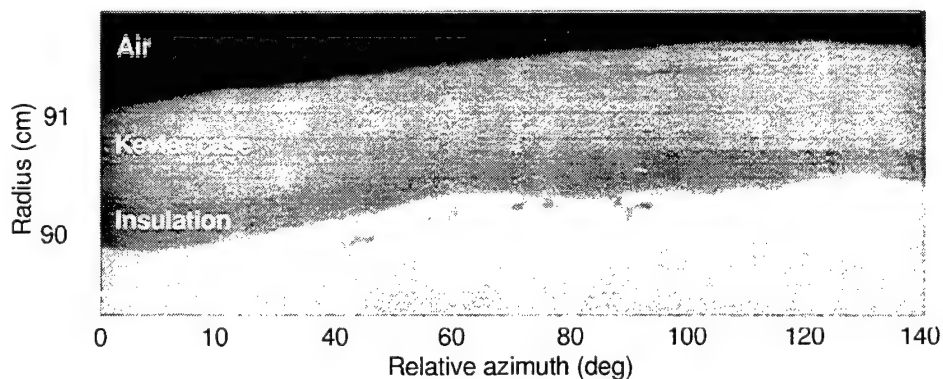


**Figure 19. Polar sampling of transaxial section of C4 phantom reconstruction**

In this radius-versus-azimuth reconstruction, each crack is circled. Each crack's opening is partially filled with aluminum, except at the ends. The scale is approximate.

In addition to imaging the synthetic cracks, the C4 reconstruction includes several classes of artifacts (some not easily observed in the reproduction of Figure 19). These are named and discussed in the following paragraphs:

- *Dark band at constant reconstruction radius.* This is almost certainly a beam hardening artifact associated with the flattener that was used in this experiment. It is believed that the position of maximum change in relative cross-section (Compton vs. pair production for carbon vs. lead) *while still maintaining reasonable transmission* results in maximum change in hardening artifact. This can be corrected by a remapping of the projection intensities as a function of both radius and initial measurement.
- *Black/white arches.* These generally are associated with sharp radial features. This is the effect of the completion algorithm; we are missing the differences in absorption due to the radial rays on the edges of sharp radial features. This is a function of the HR3DCT process, and it is something that we must live with.
- Slightly different density in the air in the region next to the case. This is probably a combination of a slight amount of hardening and an imperfect convolution; since it is in the outside air, it is of little consequence.

## 6.2 Graphite Titan

A production SRMU booster was scanned and reconstructed. This scan dramatically demonstrates the robustness of the HR3DCT algorithm. Data for this scan were acquired with no equipment beyond that already present in Alliant's Titan RTIS facility. Scatter control and collimation were not optimized. The facility's isocon camera was used in its normal RTR configuration. An incomplete set of views, sampling only 60 degrees of the case at intervals of one degree (rather than the desirable 0.2 degrees) was acquired. In spite of the non-ideal data, the reconstruction produced important results. Figure 20 is a surface of constant radius taken at the insulator/propellant interface. The dark vertical band in the image center is an insulator repair that resulted in a thicker than normal insulator over a 10 cm axial extent. The features on either side of this band are areas of unusually thick barrier coat that resulted from a power failure during barrier coat application. The oblong horizontal patches are actually puddles of the coating material which "ran" toward the bottom of the image as the case was rotated following the restoration of power to the process. The reconstruction is somewhat noisier and has less resolution than other reconstructions reported in this project, but served its diagnostic purpose well.

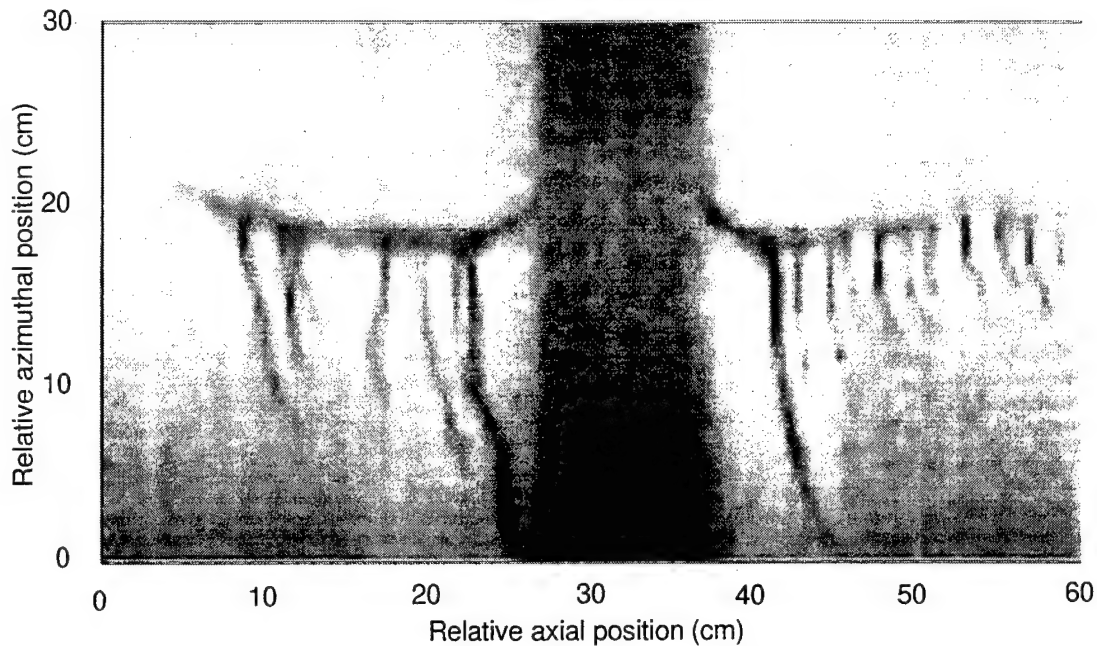


**Figure 20. Composite Titan reconstruction.**

This constant-radius section of a HR3DCT reconstruction easily detected and unambiguously defined the nature of an anomaly that existed at the insulator/propellant interface. Excess accumulation of a barrier coating material appears in two oblong areas, from which fingers of material extend toward the bottom of the imaged area. The scale is approximate.

### 6.3 Steel-case Titan phantoms

Two Titan phantoms were constructed. Each simulates a section of a 3-m diameter solid rocket motor that has a steel skin, a rubber liner, propellant, and various low-density inserts to simulate unbonds at the insulator/propellant interface.

#### 6.3.1 Thick-section Titan phantom

The 19-mm thick steel skin phantom was designed to mimic the effects of the region of a large diameter steel-cased motor in regions which have historically presented inspection difficulties. A 3-mm rubber insulation simulant was attached to the inside of the 3-m diameter steel section, and various thicknesses of very low density non-compressible shims utilized to mimic the effects of unbonds of thickness ranging from 0.1 mm to 0.5 mm and diameters 2.5 cm to 10 cm. Unfortunately, the images that were produced by this technique are not diagnostically useful. The reasons have to do with very low flux along the inside tangent line, and a large amount of scatter that overwhelmed the change in flux produced by these artificial unbonds. The only method that we believe might be helpful in acquiring good information on these particularly thick steel segments is in a combination of extended data acquisition time, slit CT radiography (to reduce the effects of scatter), a very thin (and hence, relatively inefficient) X-ray scintillating screen, and a very deep dynamic range CCD. As we discovered in the course of the experiment, the field flattener, which we used to decrease the dynamic range to a level that could be utilized by the CCD, caused at least as many problems in reconstruction as it mitigated in data acquisition.

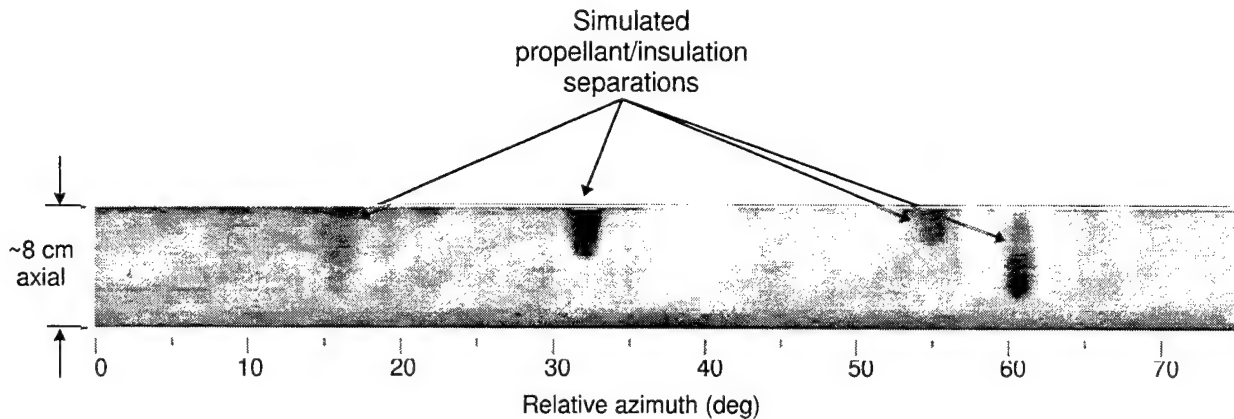


**Figure 21. Constant-radius section of steel Titan reconstruction.**

The test object simulated a 9-mm thick 3-m diameter steel-case Titan segment. The horizontal and vertical axes are respectively the azimuthal and axial locations. The dark elliptical areas image circular separations varying in thickness from 0.1 mm up to 0.5 mm. These areas appear to be elliptical due to the compression in the circumferential scale in this display. The scale is approximate.

#### 6.3.2 Thin-section phantom

The 9-mm thick steel skin Titan phantom was constructed in a similar manner to that of the 19-mm model. Data sets were acquired with different screens, with field flatteners and without field flatteners, at different distances from source to object and from source to detector, so that we might better understand the effects of these choices. For the most part, these choices made minimal differences within the confines of the experiment constraints. This is in itself reassuring -- the HR3DCT process is reasonably robust and will work in a variety of circumstances. The individual slices are not particularly interesting, because the data are difficult to sort out for the individual razor-thin unbond simulators. However, the composite image, integrated over a small thickness in radius in the region of the interface (but still at a relatively constant radius), is displayed in Figure 21. Because of physical restrictions during the data acquisition, certain of the simulated unbonds did not appear in the field of view. However, we very clearly found those of diameter 5 cm ranging in thickness from 0.1 mm to 0.5 mm. The only unbond that we did not see that *may* have been in the field of view was 0.05 mm thick and 0.08 mm in diameter. *By comparison, we note that no other CT technique could have made any images with a Titan class rocket motor.*

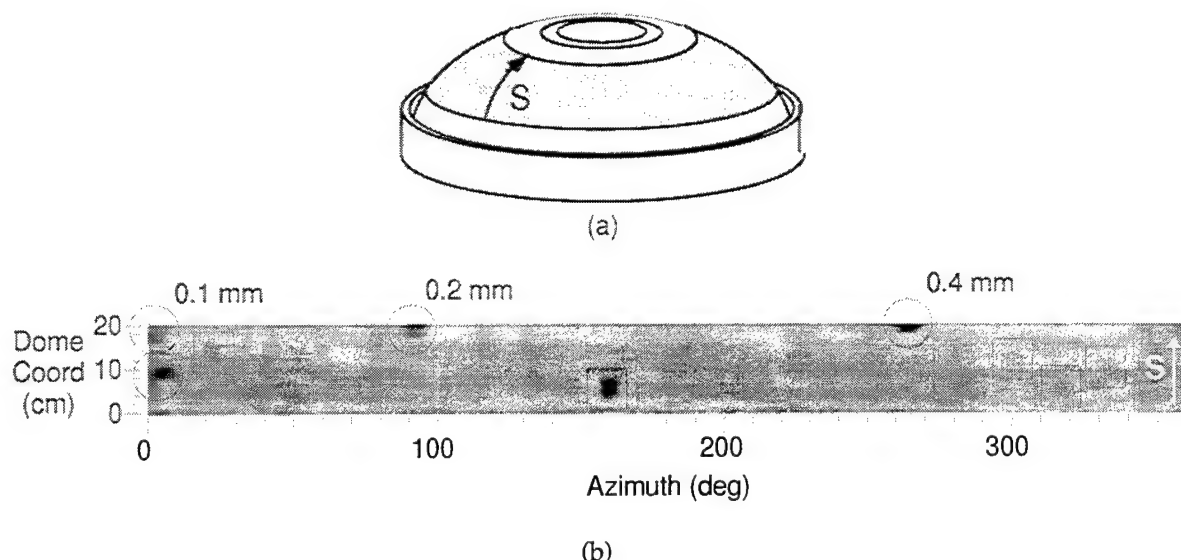


**Figure 22. Minuteman dome reconstruction.**

The upper diagram (a) shows in gray the surface which has been “unwrapped” in (b). To produce (b), the HR3DCT reconstruction volume was sampled along the interface between the case and propellant, revealing a number of bondline anomalies. Four of six circular artificial separations (shown circled) were clearly detected. The three farthest up the dome were 5-cm diameter Nalgene disk stacks, and one was a 2.5-cm diameter Millipore disk stack. Both materials are approximate simulations of air. The scan also detected five resin-rich areas (shown in squares). These are natural features of the Minuteman case. The scale is approximate.

### 6.3.3 Minuteman third stage dome phantom

This phantom was built using a third stage dome section from which propellant had been removed. Simulated unbonds were arranged inside the dome at the interface and the shell was then filled with propellant simulant (foundry sand). The section of the 3-D reconstruction shown in Figure 22 exhibits utter uniformity except in the region near the case, where each of the anomalies is found. This figure was reconstructed from the single data acquisition sequence. The geometry of the figure follows the contour of the Minuteman dome, so that each of the unbonds can be seen. The notion of following the geometry of the part is extremely important for unbonds and other bondline maladies that HR3DCT is likely to encounter. The inherent contrast is approximately 3% to 4%, consistent with our previous experience. Statistical accuracy does not seem to be the cause of this limitation, since a great deal of flux was available.



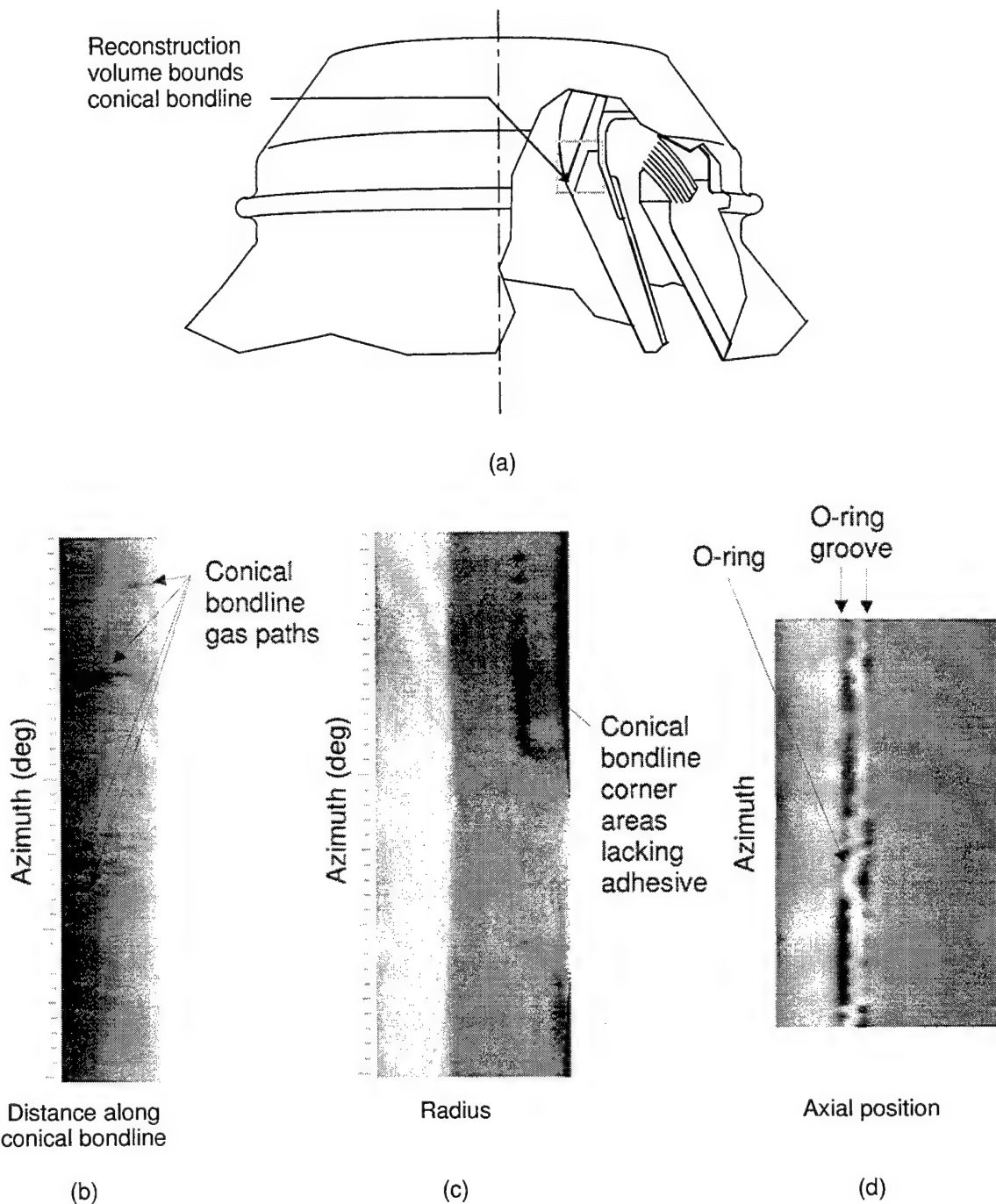


**Figure 23. Reconstructions through nozzle throat.**

This diagram presents three sections through a single HR3DCT reconstruction of the conical bond area of the nozzle whose cutaway diagram appears in (a). Section (b) is particularly significant, since it is actually a conical surface – an output natural for HR3DCT, but cumbersome for other modalities.

#### 6.3.4 Nozzle

The throat area of a nozzle from a medium-size SRM was scanned. The throat is made from three 3D carbon-carbon components, as shown in Figure 23 (a). Two of these components join on a truncated conical surface. Failures in adhesion between the two surfaces provide

paths for escape of hot gases. In such a scenario nozzle failure is a possible outcome. This nozzle included three intentionally-inserted bondline problems and (as this reconstruction definitively showed) several unintended anomalies.

The reconstruction volume contains the entire surface of this joint. Three images made from this reconstruction show aspects of the bondline in this joint. The first (b) is a surface along the conical portion of the joint. The second (c) includes the portion of the joint lying in the transaxial plane. The third (d) is a cylindrical surface that includes an O-ring at the outer end of the joint. Each of these sections reveal significant features difficult or impossible to assess in any other way.

In (a) the intentional gas paths enter the bondline from the left just over half way down the image. The paths appearing in the upper half of the image were not artificial. The advantage of this modality over alternatives is that the condition of the entire three-dimensional surface can be assessed at a glance.

In (b) the joint's circular corner is clearly seen. Areas lacking adhesive are clearly evident.

In (c) the O-ring, which should be tight and straight in its groove, is seen to be loose. Pieces of excess adhesive are also visible.

## **6.4 Overall conclusions**

### **6.4.1 Standard performance measures**

Table 11 incorporates the overall traditional measures of goodness of imaging. However, the table does not explicitly reflect many of the considerations that go into each calculation. For example, the *Expected Unbond Detection Capability* applies only within the context of the performed experiment, not to ultimate technique capability.

**Table 11**  
**Validation results in terms of standard measures.**

| Test specimen               | Number views<br>/<br>View interval<br>(deg) | Data<br>precision | Contrast<br>(percent) | Effective<br>resolution <sup>18</sup><br>element size<br>(mm) | Expected<br>unbond<br>detection<br>capability<br>(mm) | Critical<br>limitations |
|-----------------------------|---|-------------------|-----------------------|---|---|-------------------------|
| C4 phantom                  | 3600 / 0.1                                  | 0.0038            | 3-4                   | 0.4   | 0.03-0.08   | algorithm               |
| Graphite Titan              | 50 / 1.0                                    | 0.03              | 12-15                 | 1.0   | 0.08-0.3  | Isocon,<br># views      |
| Thin case Titan<br>phantom  | 1200 / 0.1                                  | 0.0038            | 4-5                   | 0.4   | 0.03-0.13   | algorithm,              |
| Thick case Titan<br>phantom | 1200 / 0.1                                  | 0.0038            | n/a                   | 0.4   | n/a   | MTF, dynamic<br>range   |
| Minuteman 3rd<br>stage dome | 720 / 0.5                                   | 0.0038            | 3                     | 0.4   | 0.01-0.03   | algorithm               |
| Nozzle                      | 720 / 0.5                                   | 0.0038            | 3-4                   | 0.4   | 0.05-0.1  | algorithm               |

Much of the range inherent in the detection capability has to do with the specific geometry, and the different densities on either side of the interface.

#### 6.4.2 Specific observations regarding techniques and limitations

As a result of the above experiments, we draw the conclusions described in the remaining paragraphs.

First, no matter how strong the X-ray flux, how efficient the X-ray detection, or how good the algorithm, we always seem to be limited to a fractional accuracy equal to a 3% standard deviation in the calculated material density. In examining the Minuteman third stage dome sample, the experiment provided more than sufficient flux, yet the standard deviation remained at nearly the same level as in some of the other, more difficult specimens. This result may have to do with a deficiency in the intrinsic HR3DCT process -- which is after all dealing with a very sparse data set.

Second, when the system choice allows it, always choose the camera system/screen with the better MTF, as long as the fall-off in total integrated X-ray photon dose falls within the parameters of the experiment. The experiment was done with a GOS screen and the special

---

<sup>18</sup> Effective spatial resolution in the radial direction. The circumferential spatial resolution is approximately a factor of 10-20 coarser, depending upon the geometry and the number of views obtained.

high density leaded faceplate. We believed that the faceplate would provide a better stopping power that would compensate for the slightly lower MTF. However the MTF was determined to be more important than the flux, at least down to the factor of two level of this experiment. The reason has to do with the fact that the transmission on the inside tangent of large cylindrical rocket motors and their simulants is so small compared to the main beam, that even the smallest component of MTF that extends the large central flux into the wings of the distribution can easily overwhelm the inside tangent signal.

Third, the best apparent place for an optically thin test specimen is as close to the screen as possible, consistent with generalized scattering mitigation. This is because the screen usually has a better effective element size than the X-ray source. If scatter is the dominant consideration, placing the test halfway between source and detector will act to reduce most scatter. The more attenuating the test specimen, the more likely that the specimen should be placed exactly half-way between source and detector.

Fourth, field-flatteners should be used only as a last resort, particularly if the features of interest are in very highly attenuated areas. The normalization that was required was difficult.

Finally, if there is any choice in the matter, *do not* use an Isocon, or other non-solid state device as the camera. While an image could be constructed from the limited Isocon data on the graphite Titan, the dynamic range of the final image was only a few bits. While impressive in displaying the data, the combination of temporal variations in the camera and the very low dynamic range – 100-200 was typical over the course of an experimental run – made data normalization difficult and limited the quality of the reconstructed output.

These conclusions are incorporated into the application guide and conceptual design, Sections 7.1 and 9 of this report.

## **6.5 Cost/benefit analysis**

The following cost/benefit analysis (comprising the remainder of Section 6.5) comprises excerpts from the analysis produced by Alliant Techsystems, a member of the project team, of the value of HR3DCT technology in Alliant production programs. Editorial changes inserted to clarify the original text are enclosed in square brackets.

### **6.5.1 Introduction**

High Resolution 3-Dimensional Computed Tomography (HR3DCT) offers manufacturers of advanced aerospace products a unique opportunity to image products which can be otherwise difficult to assess. Large objects such as space rocket motor boosters and nozzles have been evaluated successfully with this technology giving insight into the structure of these parts which cannot be evaluated in other ways. Not only does retrofitting an existing Real-Time-Radiography (RTR) system with a higher dynamic range camera system and computing hardware show to be a cost effective way of integrating a computed tomography system, it offers a way of imaging annular regions of objects which cannot be imaged using conventional CT.

We at Alliant Techsystems investigated the return on investment for implementation of HR3DCT using [three] different scenarios. [These scenarios include a traditional analysis which accounts for direct program costs only, and two analyses which account for cost avoidance and business loss] We feel that HR3DCT shows promise in each of the three mentioned cost/benefit analysis methods and we are currently evaluating insertion of this technology into a number of programs.

#### 6.5.2 Traditional cost/benefit analysis - Cost savings

The traditional cost/benefit analysis is based on determining cost in materials and labor for the existing inspection and then estimating cost for the proposed inspection including materials labor and capital equipment. In order to determine cost benefit we must show direct cost savings over the remainder of the production program.

Estimates show that implementation of HR3DCT on the Titan IV SRMU would offer a positive return on investment within two years in replacing existing RTR inspection technology.

[Having considered the replacement of the RTR inspection by HR3DCT, attention was turned to the portion of the existing inspection performed using film.] Present estimated cost for existing film shots is \$25,000 per motor in materials and labor to shoot the domes. Estimated cost for the HR3DCT inspection which eliminates the film is \$1,000. We then have a cost savings of \$24,000 per motor. At a flow-rate of 1 motor every 6 weeks, implementation of the HR3DCT system as a replacement for film in the Titan IV would pay for itself in the period of one year.

Traditional cost/benefit analysis of implementation of HR3DCT in the Delta II and Pegasus rocket motor programs did not show a return on investment in the lifetimes of the program. Cost/benefit analysis for nozzle programs also did not show return on investment in the lifetimes of the programs.

#### 6.5.3 Non-traditional cost/benefit analysis- Cost avoidance

A non-traditional cost/benefit analysis based on cost avoidance can be performed by determining the cost for one unit of the product that would be lost if the proposed technology was not in place. This might be due to insufficient inspection sensitivity or lack of understanding of the manufactured structure. The probability of loss to the program is then estimated and the cost computed. This cost is then compared to the estimated cost for the new inspection including material, labor and capital.

Again we first looked at the Titan IV SRMU program for cost/benefit analysis. Replacement costs from one Titan IV segment is multiple millions of dollars. Additional costs are incurred from the demilling of the lost segment. This adds approximately an additional million dollars. If the HR3DCT technique can save one segment then the system pays for itself with one segment. This scenario was almost played out in the Titan IV TAC026 segment with the barrier runs in the lining system being originally interpreted as rejectable unbonds. The Material Review Board (MRB) determined that the motor was acceptable based on experimental testing laboratory data simulating the bonding condition.

Preliminary HR3DCT images were generated late in the decision making process and corroborated the MRB decision. Subsequently we have not experienced any additional anomalies in the Titan IV SRMU program where HR3DCT would be beneficial in a diagnostic mode. Probability estimates are low for additional problems in the Titan IV bondlines for which HR3DCT would provide definitive information. Based on low probabilities in this scenario, implementation of HR3DCT has marginal savings to justify implementation. If the probabilities increase however, implementation would be justified.

Non-traditional cost/benefit analysis in the other motor and nozzle programs yielded insufficient savings to justify implementation costs.

#### **6.5.4 Very non-traditional cost/benefit analysis- Loss of product line**

The third cost/benefit analysis assumes that an entire product line is lost. This may be an existing program or a new program. Loss of a program might be due to insufficient inspection sensitivity or lack of understanding of the manufactured structure. The cost/benefit analysis compares the cost of implementation to the cost of the loss of an entire product line. Several programs were evaluated in this type of a cost/benefit analysis.

The first program is known as the F22 pivot shaft. The fiber-placed thick walled composite structure is designed as a primary control link for the F22 horizontal stabilator. The shaft is a cylindrical at one end and transitions into a tapered box beam on the other end. At the transition between the cylinder and boxbeam the shaft also has a bend. The transition region is difficult to inspect ultrasonically due to non-normal incidence layers in the structure. Due to structural loads in this region, identification and sizing of delaminations is critical. If this becomes impossible ultrasonically then the program could be placed in jeopardy and HR3DCT implementation could be cost justified.

The second program is the EELV program. This new low cost launch system requires new rocket motors which will require inspection. HR3DCT is presently in consideration for implementation in the program as an alternative to conventional RTR. Present costs estimates indicate that HR3DCT will be competitive with conventional RTR.

#### **6.5.5 Conclusions**

The following conclusions can be drawn from Alliant Techsystems experience in examination of HR3DCT in the inspection environment:

- HR3DCT is an effective engineering diagnostic tool
- HR3DCT is cost effective in replacing film inspections
- HR3DCT provides quantitative data in an orientation that the analyst can use in analysis
- HR3DCT is cost competitive with high energy RTR in a new program implementation
- HR3DCT provides data to the inspector in an un-ambiguous mode for interpretation

## 7. ALTERNATIVE RECONSTRUCTION ALGORITHMS AND RESULTS

High-resolution 3-D CT algorithms are not found in the literature. However, work has been published on *pieces* of the HR3DCT problem. For example, reconstruction from a limited data set is a broad and frequently-considered topic. Likewise, reconstruction of a solid volume from cone-beam projections has been studied. To insure that existing technology is fully utilized in our program, Dr. Todd Quinto of Tufts University reviewed current work in the field to find, evaluate, and summarize alternatives to portions of limited data reconstruction portion of the HR3DCT reconstruction algorithm. Cone-beam algorithms were not addressed, because a good cone-beam algorithm exists, because the limited data reconstruction seems to be the more difficult problem, and since few limited data algorithms admit 3D adaptation. Dr. Quinto's findings are summarized below.

Dr. Quinto's work was performed within public, international literature. Initially, it resulted in the paper, *Survey of Reconstruction Algorithms for Limited Data Tomography of Rockets* (included in the Interim Report's Appendix A). The survey describes the characteristics of large SRMs that restrict practical CT solutions to those requiring only projections along lines roughly tangent to the outside of the case. Such solutions are made possible by a class of CT reconstruction algorithms known as exterior data reconstructions. Six examples are mentioned; four are discussed in some detail. These include data completion algorithms, the Exterior Reconstruction Algorithm (ERA), regularization, and support minimization. Of these, the first two algorithms emerged as most promising. HR3DCT, which utilizes a data completion algorithm designed for the unique characteristics of large SRMs, is the primary focus of our project. The ERA underwent parallel evaluation by Dr. Quinto under this project, including the reconstruction of data obtained in the first two project phases. The results of this evaluation are discussed later in this section.

The above general work lead to a second effort, which is reported in *Survey of Data Completion Algorithms for Limited Data Tomography* (included in the Interim Report's Appendix B). This paper compares completion performed in projection-space with that performed in Fourier space. Of projection-space completion, Dr. Quinto points out that first-derivative continuity is essential across the boundary between the measured and synthetic projection data. When this condition is not observed, large artifacts will occur in the vicinity of large density gradients in the reconstruction. The HR3DCT algorithm is a projection-space completion algorithm. Its completion algorithm ensures first-derivative continuity. Fourier space completion algorithms include *simple completion* and *consistent completion*. These algorithms both operate in a sinogram space that has been Fourier transformed perpendicular to the sinogram's angle axis. The values in this transformed sinogram along the inner edge of the projection are then used to generate the missing transformed sinogram values. Simple and consistent completion algorithms differ in the approach to this problem.

The ERA algorithm mentioned above appeared to offer an interesting alternative to the data completion approach taken in our project — at least in the planer reconstruction case. As part of the final phase of this project, the ERA algorithm was used to reconstruct portions of the data. This effort is reported in detail in the remainder of this section, which contains the



initial portion of the Tufts University Final Report. Technical details of the ERA algorithm (the remainder of the Tufts final report) are submitted separately.

## 7.1 Overview.

The exterior reconstruction algorithm (ERA) collects data in a novel way to detect common defects in rocket motors and exit cones more efficiently than standard computed tomography. The algorithm is useful for large diameter rocket motors for which regular computed tomographic methods fail. Four reconstructions from the ERA have been done, and they all demonstrate the success of the algorithm with the Perceptics data. The reconstructions are clear and accurate.

Common defects in exit cones and rocket motors are of the same general shape. Many rocket exit cones are made up of 40 or more laminated layers, and delaminations, very thin separations that run between the layers, are typical defects. Separations in gaskets in outer regions of rocket motors or defects in rubber insulation between the rocket case and propellant are both common defects that occur along the outer circumference of the motor. For both rocket motors and exit cones, the most important sections to evaluate are typically the outer parts of the object, annular rings (as seen in cross section). Furthermore, the typical defects are separations with sharp boundaries in the radial direction<sup>19</sup>.

X-rays are attenuated so highly when traveling through the center of large diameter rocket motors that X-rays through the center provide little useful data. Even with small diameter rocket motors or with exit cones, data acquisition time can be quite long. Data acquisition through the center is a real limitation of standard tomography for such evaluation.

The ERA uses only data on X-ray paths that DO NOT go through the center of the object; these paths are more-or-less tangent to the outer ring of the object. Such data are ideally suited for the non-destructive evaluation of rocket motors and rocket exit cones: the unusable data through the center is not required, and the algorithm reconstructs only the area of interest--the outer part. This data are called 'exterior data' since the data are over lines 'exterior' to the inside of the object. Data acquisition time is much less than with standard CT methods because X-ray absorption paths that go through the center are not required.

Furthermore, high density objects and data artifacts that are inside the rocket do not affect reconstructions; although they do affect reconstructions using filtered back projection, since filtered back projection requires this data.

The ERA is already well developed. Its description is in the public domain and the numerical methods and programs for the algorithm were developed several years ago.

---

<sup>19</sup> L. A. Shepp and S. Srivastava, Computed tomography of PKM and AKM exit cones, A. T & T. T. Technical Journal, 65(1986), 78-88.

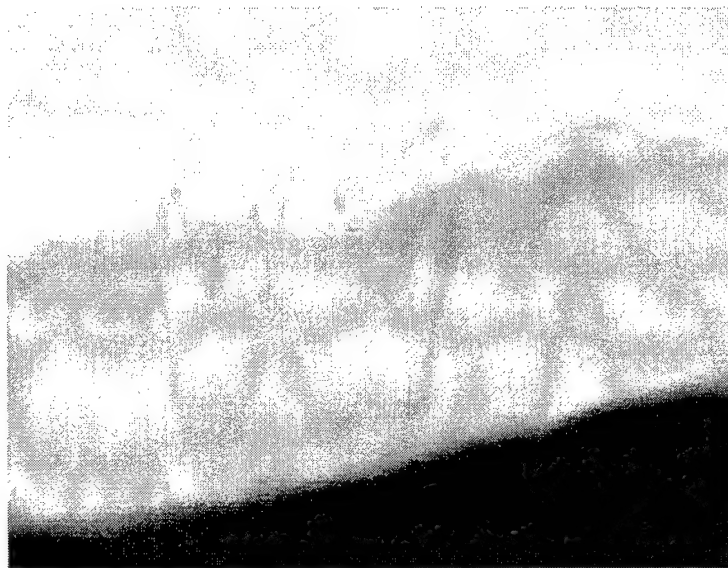


## 7.2 Analysis.

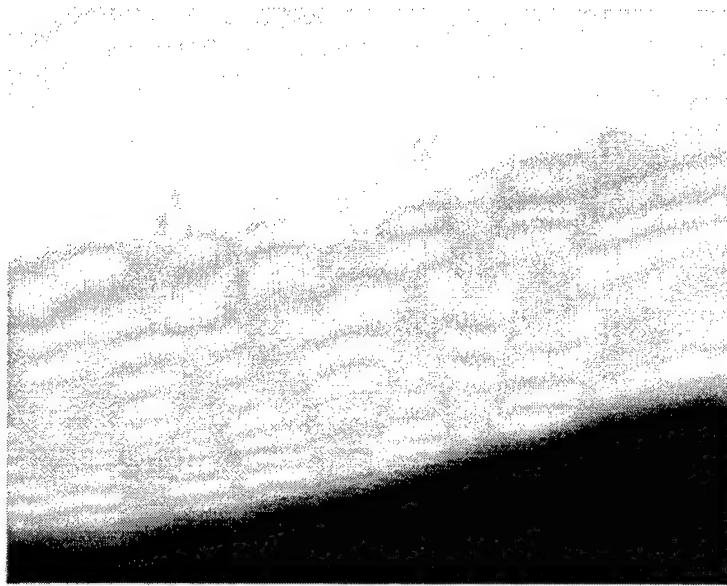
Four sets of reconstructions from Perceptics data are provided with this report. Two reconstructions are from the preliminary data that was provided by Perceptics in December, 1994, and two reconstructions are from the final C4 rocket data from June, 1995. Both sets of Perceptics data are exterior data since they include only data from X-rays over lines that are almost tangent to the outer shell of the rocket. Such data are ideal for the ERA. Both objects and the Perceptics data sets have intriguing challenges that tested the robustness of the algorithm.

### 7.2.1 Preliminary data (May 1993 experiment).

Reconstructions from this preliminary data are provided (Figure 24) so that the strengths of the algorithm with limited angular data can be shown. Two reconstructions are given to show the different resolution and "smoothness" of the reconstruction with 150 and with 400 Fourier coefficients. Boundaries are not quite as sharp with the reconstruction that uses 150 Fourier coefficients, but artifacts and "roughness" in the reconstruction are minimized.



(a)



(b)

**Figure 24. ERA reconstructions.**

Image (a) reconstructs 150 polar Fourier coefficients and then sums a Fourier Series in theta, the angular variable, up to order 150. Image (b) reconstructs 400 coefficients (a Fourier Series in theta, the angular variable, up to order 400, but with some smoothing). In both cases, 220 polynomials are summed for each Fourier coefficient.

Artifacts were limited by several means. The data were so noise-free that no additional smoothing was necessary before the algorithm reconstructed the data. For the reconstruction using 400 Fourier coefficients, a smoothing was done in the angular variable to correct for artifacts that appear because of these higher Fourier coefficients. The number of Fourier coefficients was chosen to give good resolution without distortion and the artifacts inherent in reconstructions that use too many Fourier coefficients.<sup>20</sup>

The reconstruction consists of two components, the *range component* and the *null-space component*. The range component is easy to reconstruct and the null-space component is hard to reconstruct for mathematical reasons. Therefore, the null space component was smoothed to get rid of dramatic oscillations. For the first 30 Fourier coefficients, the first 10 null space terms were summed and this was used as the null space. Without this smoothing (setting high frequency null space terms to zero), the reconstruction would oscillate so much so as to be useless.

The data included X-ray sources between  $0^\circ$  and  $135.3^\circ$ . Since the ERA needs data for sources all around the object (even if the data are made up), the given data were linearly interpolated in the missing range ( $135.3^\circ$  to  $360^\circ$ ). This interpolation was smoothed to the data in the first two degrees of the real data.

---

<sup>20</sup> Up to a point, the more Fourier coefficients one uses, the better resolution and sharper boundaries one sees. All data have some noise, and this noise causes inaccuracy in higher Fourier coefficients. So, if one uses too many Fourier coefficients in a reconstruction, this noise will cause artifacts, streaks, and oscillations in the reconstruction.

The preliminary data set sent to Tufts was missing the last few source positions (at around  $135^\circ$ ). This explains why the Perceptics reconstruction includes slightly more of the rocket than the ERA reconstruction.

*Discussion:* The preliminary Perceptics data were limited in angular extent. That is, data were given only for sources in a range of  $135.3^\circ$  of the outer shell, rather than the full  $360^\circ$ . Exterior data that is also of limited angular extent is much more limited than just exterior data, and reconstruction is more difficult.

The ERA itself had not been developed for data limited in angular extent and the original algorithm requires data around this complete circle, even if the data are made up. Despite this data limitation, the algorithm reconstructed the data as well as if it had not been limited in angular extent. This reconstruction contained no artifacts that were due to limited angular extent, and the reconstructions look as good as those from complete data given from the May 1995 experiment. The refinement to the algorithm that allowed it to work with this limited data will work with any data set that is limited in angular extent.

Overall, the boundaries are clear and the small blobs inside the propellant are quite clear with good density resolution. The shell and propellant densities are fairly uniform. The only feature of the object which is not completely clear is a possible separation near the boundary of the rocket at around 20 degrees. This is visible in both reconstructions, but it is smoothed out in both radius and angular extent. Rather than looking like a sharp separation, it looks like a small 'indentation.'

Improvements for such defects near the object boundary could require further refinement to the algorithm. Probably something simple, such as summing more polynomials, will work; more polynomials would provide more resolution in the radial direction (up to the point where the problems in footnote 1 occur); after all, only 220 polynomials are summed now, even though the algorithm reliably reconstructs 400 Fourier coefficients. Another, more elaborate solution would be to use limited data Lambda tomography along with the ERA. Limited data Lambda CT should image this specific type of defect well even though limited data Lambda tomography would not image the other defects nearly as well as the ERA (as demonstrated by current Lambda reconstructions by Kuchment<sup>21</sup>.) One could combine this ERA reconstruction with a limited data Lambda CT reconstruction that will clearly show such delaminations. Since Lambda reconstructions will not show the detail that the ERA does (for example, it would not show all of the little blobs inside the propellant), it could not be used alone<sup>22</sup>.

#### 7.2.2 Final data (May 1995 experiment).

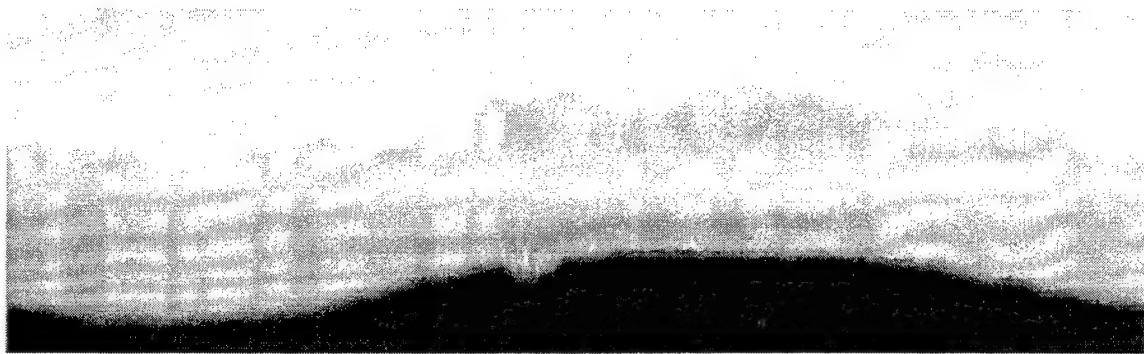
The data set from this experiment is from sources that go completely around the rocket. But, a limitation in data preprocessing created a band of high density that masked about 1/6 of the reconstruction. Therefore, two sets of reconstructions (Figure 25) are presented for that data.

---

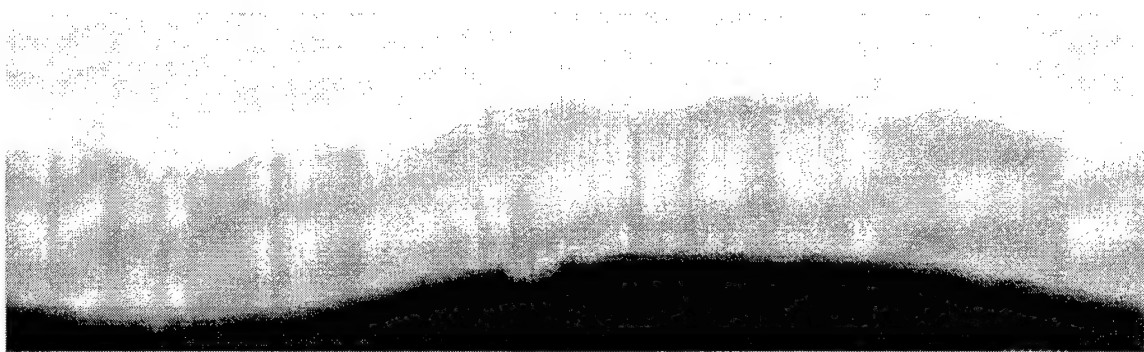
<sup>21</sup> A. Faridani, E.L. Ritman, and K.T. Smith, Local tomography, SIAM J. Appl. Math, 52(1992),459–484.

<sup>22</sup> See unpublished work of Kuchment for limited data Lambda CT

Image (a) is done with the data provided without further postprocessing, and image (b) is 'corrected' in a simple way that could be used on any such data set.



(a)



(b)

**Figure 25. ERA reconstructions.**

Image (a) reconstructs 400 polar Fourier coefficients (a Fourier Series in theta, the angular variable, up to order  $\infty$ ). Image (b) reconstructs then does some simple postprocessing to the zero Fourier coefficient. In both cases, 220 polynomials are summed for each Fourier coefficient.

Artifacts were limited by several means. The data was so noise-free that no additional smoothing was necessary before the algorithm reconstructed the data. Smoothing wasn't even necessary in the angular variable for this data. The number of Fourier coefficients, 400, was chosen to give good resolution without distortion and artifacts inherent in reconstructions that use too many Fourier coefficients<sup>23</sup>.

The reconstruction consists of two components, the *range component* and the *null-space component*. The range component is easy to reconstruct and the null-space component is hard to reconstruct for mathematical reasons. Therefore, the null space component was smoothed to get rid of dramatic oscillations. For all 400 Fourier coefficients, the first 10 null space terms were summed and this was used as the null space component (see the end of §2.2.3). Without this smoothing (setting high frequency null space terms to zero), the reconstruction would oscillate so much so as to be useless.

---

23

The processed reconstruction was altered in the zero Fourier coefficient. That is, a factor is added to the reconstruction that does not change in the angular variable. This factor is added in two places. First, the little ripples that occur for  $r$  near the inside radius of the object were straightened out. This can be done on any reconstruction. Such ripples occur because of Gibbs phenomenon; when one sums polynomials (or Fourier series), some overshoot can occur near the ends of the data. This change could easily be automated into the algorithm.

The second change occurs around the high density band.

*Discussion:* Both reconstructions clearly show the features inside the propellant, but the reconstruction with postprocessing shows outer features more clearly.

There are two high density objects in the rocket propellant at about radius  $r = 34$  in quadrants 3 and 4 that are visible in reconstructions that use the entire data. These will create streak artifacts in any reconstruction that uses all the data. Since the ERA reconstructions do not need this inside data that causes the streaks, these reconstructions do not suffer from such streaks.

The epoxy raceway adhesive track at the boundary of the rocket in quadrant two are a little distorted. This is a result of the fact that the data set itself is limited and this limitation makes these features hard to reconstruct. The mathematical reasons for this<sup>24</sup> are basically as follows. In general, boundaries between regions are easier to reconstruct from a tomographic data set if some lines in the data set are tangent to the boundary. For example, the outer boundary of the rocket is "good" for exterior data since lines tangent to it are in the data set. And, it is reconstructed well. However, tangents to the track go through the center of the object and aren't in the exterior data set. (Recall, that the exterior data set includes no lines through the center of the object.) Therefore, the track is harder to reconstruct from exterior data than the other features in the object.

The distortion at the epoxy slightly masks the separation within the epoxy. However, the density difference between the epoxy and the separation is greater in the ERA reconstructions than in the Perceptics filtered back projection reconstructions (the ratio of separation/surrounding density of around .88 or .79 versus .95, .91 in the filtered back projection reconstructions).

The Perceptics data are off the midplane, but the ERA assumes midplane data. However, this change causes no ill effects and there are no artifacts or distortions attributable to this. The algorithm recovered 400 Fourier coefficients with this data and did not need as much smoothing as the midplane data in the May 1993 experiment. Because of this encouragingly good preliminary result, the algorithm should be tested on data that are farther from midplane.

---

<sup>24</sup> E.T. Quinto 1993, Singularities of the X-ray transform and limited data tomography in  $R^2$  and  $R^3$ , SIAM J. Math. Anal., 24(1993), 1215-1225.

### 7.2.3 Reconstruction time.

The algorithm is now designed to be easy to debug and to test parameters, not to be efficient and fast, and it currently takes about 1.5 hours to reconstruct the 15 MB Perceptics raw data file on a DEC Alpha Station, the well-used university research computer. Ease of testing is much more important in this development stage than algorithm speed. So, for example, one program reads a 12MB data file between 150 and 400 times; if the programs were written for speed rather than experimentation, this file would be read once and the same program would do all the manipulations to this file rather than passing 200 partially processed files to other programs. Just having this large data file read once would save significant time, perhaps as much as 50%, and this would be an easy refinement to implement. Furthermore, over one third of the processing can occur as the data are being acquired, if the algorithm is programmed into the computer that records the data.

### 7.2.4 Minimizing the thin parabolic artifacts near the inside reconstruction boundary.

There are some thin parabolic artifacts near the inside boundary of the reconstructions. They look like thin curves making an arc from the inner boundary of the shell up to the inside boundary of the reconstruction. These could be data anomalies or algorithm artifacts. (Such curves were not visible on earlier simulations which had higher random noise (1/2-1%) but were less complicated.) They are clearly artifacts since they are thin, they have low density contrast, and they all look alike. The artifacts have densities close to that of the surrounding material, but they are noticeable because of their sharpness.

These artifacts will be decreased if one smooths the reconstruction more. First, one can use fewer polar Fourier coefficients in the reconstruction. The benefits can be seen from the two reconstructions from preliminary data. The reconstruction with 150 Fourier coefficients has fewer of these artifacts than the one with 400 Fourier coefficients. A reconstruction done with 100 coefficients had practically none of these curves. The trade off is that region boundaries are less sharp, but this effect can be decreased by summing fewer coefficients only near the inside of the reconstruction (where the effects occur).

Also, one can smooth the reconstruction more in the radial variable than is currently done. Here, too, if one smooths more near the inside boundary and less near the outside, one will decrease the ill effects of the boundary smoothing.

Both methods to minimize these artifacts are easy to implement and do not add at all to reconstruction time.

Reconstructions from the Perceptics data show the strengths of the algorithm as well as some minor limitations that provide directions for future research and development. The algorithm clearly shows shapes and locations of the defects in the propellant of the rocket, and it shows separations in the shell. It works with data that are limited in angular extend and it works with non-midplane data.

## 8. APPLICATION GUIDE

This section is intended to guide prospective HR3DCT implementers. Section 7.1 provides helps for deciding whether a particular application is feasible. Section 7.2 discusses equipment and software requirements. Section 7.3 presents information useful when optimizing the performance of an application.

### 8.1 Determining whether an application is feasible

Following is a checklist that should be evaluated to determine whether a prospective HR3DCT application is technically feasible. The HR3DCT algorithm's validity derives from a set of assumptions about imaging goals and object characteristics. When these assumptions are true, HR3DCT can provide diagnostic quality results. The checklist below facilitates evaluation of these conditions.

- ✓ The object shape is suitable for HR3DCT

HR3DCT data acquisition captures only a small fraction of the conventional edge-to-edge CT view (see Figure 2-4). HR3DCT reconstruction assumes that the *missing* portion of each projection contains virtually no information about features that are to be reconstructed. This is fundamental. Failures of this assumption result in artifacts whose severity is related to the degree of assumption failure. Questions about the suitability of HR3DCT to image a particular object can be answered by considering the validity of this assumption.

The ideal HR3DCT imaging subject is an object where, in any transaxial plane, the densities at a constant radius from the inspection axis are constant. Differently stated, the ideal HR3DCT subject can be specified entirely as a function of radial and axial location (no angular dependence). In practice, objects of this sort are uninteresting. Fortunately, HR3DCT works well when this ideal is not strictly met. For example, the natural axis of the object may be offset somewhat from the inspection axis. The object cross-section may not be precisely round. Constant-density components of the object may not be entirely homogeneous. In fact, HR3DCT is useful principally because can properly image these conditions.

One important situation where the HR3DCT assumption is nearly true is the case of constant-radius delaminations in an object comprised of concentric objects of rotation. Here, the delaminations are simply radial displacements that make a measurable difference only in near-tangent projections.

Finally, we note that as the HR3DCT projection encompasses a greater fraction of the conventional CT projection, HR3DCT behaves more like conventional CT, and the HR3DCT assumption becomes less difficult to satisfy.

- ✓ All targeted features fall within a tangent RTR projection



This requirement is easily evaluated. It is that all features of interest fall within the radial range imaged by the RTR screen. Figure 4 illustrates the region imaged by HR3DCT. The imaged annulus must include the entire outside edge of the subject.

✓ Radial resolution requirements can be achieved

Radial resolution limitations must be compared with requirements related to feature detection. The radial resolution achievable in HR3DCT is limited by three factors. First, the X-ray source beam spot shape and size combine with the imaging geometry to limit resolution. Second, X-ray and light interactions within the X-ray conversion screen typically spread signals, further limiting resolution. Finally, the camera optics and the digitization in the camera itself impose their own limits. The resulting resolution is (at best) the most limiting of these three factors. Each of these factors can be evaluated before undertaking design of a HR3DCT application.

$$R_s \approx \frac{SOD}{2 \cdot b \cdot (SDD - SOD)}$$

$$R_d \approx \frac{N}{2 \cdot W}$$

In the above,  $R_s$  and  $R_d$  are the resolution limits (in line pairs per mm) due to the source geometry and camera sampling, respectively. The beam spot diameter is  $b$ , and  $N$  is the number of samples used to represent the conversion screen dimension,  $W$ . The limitation imposed by the conversion screen is a set property of the screen that can be measured at a given energy. Note that, although two of the three resolution limits are subject to adjustment by modifying inspection geometry, such efforts may have unacceptable side effects, as discussed later in this section.

✓ Circumferential resolution requirements can be achieved

Circumferential resolution limitations must be compared with requirements related to feature detection. Two relationships bound circumferential resolution,  $R_c$ .

$$r \cdot \cos^{-1}\left(\frac{r-d}{r}\right) - r \cdot \cos^{-1}\left(\frac{r-d+R_r}{r}\right) < R_c < r \cdot \cos^{-1}\left(\frac{r-R_r}{r}\right)$$

Here,  $r$  is the distance of the feature from the inspection axis,  $d$  is the radial depth of the feature from the outside of the inspection annulus, and  $R_r$  is the realizable radial resolution described in the previous section. Actual resolution will be nearer the left expression for easily-detectable features. Subtler features (such as a delamination) whose radial size is a small fraction of the radial resolution will be less well resolved circumferentially (though still within the bound set by the right hand expression).

✓ View data reflects targeted information

Any subject feature that is intended for HR3DCT imaging should be represented (though perhaps not easily visible) in projections of the subject using the RTR equipment, geometry,



and exposure intended for the target HR3DCT application. In general, the feature should be visible in the data (though contrast stretching may be required). Note that HR3DCT, like conventional CT, will provide unit volume sensitivity far better than in component projections. However, neither algorithm can produce features that are absent from the data statistics. This criterion should be checked empirically when considering whether an application is feasible.

- ✓ Subpixel features will be unambiguously represented in reconstruction

Subject features with at least one dimension smaller than the corresponding system resolution are sometimes referred to as “subpixel” features. This term assumes that the reconstruction sample interval is similar to the resolution, so that the feature is also smaller than the volume element in the corresponding direction. The remarkable sensitivity of HR3DCT enables subpixel features to be unambiguously detected (though not resolved) in otherwise-homogeneous areas. However, when a feature occurs very near a steep change in subject density (e.g. a delamination of the interface between dissimilar materials) the delamination may masquerade as a *shift in position* of the steep change. Only when the feature is represented by values outside the range of values due to the gradient (or when shifts are impossible a priori) is the indication unambiguous. An application that relies on detection of subpixel features occurring on gradients should be avoided.

- ✓ Acquisition time is short enough

Due to the relative inefficiency of RTR imagers, high-quality data acquisition typically requires between a few and several seconds. This time, which can be measured empirically as a project is being considered, must be multiplied by the number of views and the number of scans to enable realistic assessment of HR3DCT’s viability in an application. The number of views,  $n$ , is typically greater than for conventional CT. It can be computed for a particular radial resolution,  $R_r$ , and object radius,  $r_{max}$ , as follows.

$$n \approx \frac{\pi \cdot r_{max}}{2 \cdot R_r}$$

This number is inexact, but it should be recognized that an inadequate number of views results in reconstruction artifacts.

The number of scans depends on the inspection geometry and the size and shape of the subject. Typically, the area covered by each scan is plotted on an axial-radial diagram of the subject so that the number of scans can be counted. The dimension,  $l$ , of a single square cross section scan can be determined as follows.

$$l \approx W \cdot \frac{SOD}{SDD}$$

## 8.2 Equipment and software requirements

In this section, we discuss issues pertaining to the selection of equipment and software for HR3DCT acquisition and reconstruction. The functions performed by this hardware and

software include X-ray generation, conversion of X-rays to optical image, rotation (and possibly axial translation) of the subject, digitization of the optical image, control of acquisition, reconstruction, and result display. Our objective is to guide the selection of equipment, with preference for existing equipment, wherever possible

### 8.2.1 The X-ray source

Not surprisingly, the rules governing X-ray source selection are virtually identical to those involved in making a good image for film or other X-ray imaging devices. Hence, existing source equipment will probably suffice. Essentially, the HR3DCT system should be reading the best X-ray photographs that can be made. The trade-offs are similar to those for conventional X-ray imaging applications.

- The energy must be high enough so that sufficient flux emerges from the test specimen in order to gather a statistically significant number of X-ray photons that will interact in the detection subsystem. At the same time, the energy must not be so high that there is insufficient contrast of the anomaly.
- The dynamic range of the attenuated X-rays interacting in the detector must be within the range of that detector.
- The focal spot size (and placement, as discussed in the geometric configuration section) must be within the spatial resolution guidelines.

Sometimes, we do not have the luxury of choosing the X-ray source energy level, and we are left with inspections where the dynamic range exceeds that of the detector. In such a case, we may be forced to use a field-flattener, which attenuates selectively the more transparent regions of the scene, so that such regions do not saturate the detector. While this is possible, our experience has been that the normalization required for successful field-flattening is very difficult. In particular, each data acquisition sequence requires calibrations with the field-flattener in position, without the field-flattener in position, with the test specimen and no field-flattener, as well as the conventional test specimen and field-flattener in position. Then data from various parts of the data acquisition sequence is re-normalized to extend the effective dynamic range of the detector. Robotic placement of the flattener and the test subject greatly facilitate the process of measuring normalization images.

### 8.2.2 The X-ray detector

Almost any X-ray area detector can be used to make some type of image that can be reconstructed according to a HR3DCT scheme. Our experience includes isocon-camera scans, high-end CCD-based camera scans, image-intensifier scans, and videotaped isocon imagery. In principle, digitized X-ray film can be used, provided that the geometry is well-measured. The reconstruction quality associated with these various sources can vary significantly. Thus, the camera is one place where existing equipment might best be upgraded for HR3DCT. We discuss the issues below.

Almost all X-ray detectors that are under consideration operate on the principle of an X-ray scintillating screen that converts interacting X-rays into visible light, which is eventually

collected as an image and amplified to signal levels appropriate for digitization and processing. The X-ray detector has two major parts, the screen and the camera.

We divided screens into two major groups: High intrinsic spatial resolution and high X-ray conversion efficiency. These two characteristics of screens are almost always incompatible with each other. One of the characteristics of high X-ray conversion efficiency is that the screen must be relatively thick, particularly if the X-ray source emits in the MeV range. A thick screen allows a relatively large amount of spreading of any visible light scintillation to adjacent regions of the screen compared with a thinner screen, which is engineered for higher spatial resolution (but less conversion efficiency). In addition, any X-rays interacting in the screen via scattering are more likely to interact within the thicker screen at a position farther from the original interaction site.

In all cases, we found that the higher spatial resolution screen offered superior performance. The more narrow spread of the point spread function offered better detection of features than the photon-rich thicker screen provided. We recommend choosing better spatial resolution at the expense of improved statistics. (This assumes, of course, that the type of anomaly for which we are searching is not a subtle density difference covering a very large region of pixels, but a sharp geometric feature having a local but major density discontinuity).

We divide the cameras into two groups, the analog group and the digital group. The analog group typically rely on high voltages, where electrons are accelerated and used to produce more electrons before digitization. These devices tend to be non-linear and temporally unstable. They include image intensifiers, videcons, and isocons, among others. Their great virtue is in tremendous amplification of even the smallest signals (as well as the noise). They tend to be very limited in dynamic range, usually in the range of 100-1000. In general, these cameras are not the best to work with because of the instability and the transfer curve calibration that must occur between signal level and actual radiation energy interacted. Given a choice, the experimenter should avoid using an analog detector, although it has been done successfully.

The digital group is composed of solid-state arrays, e.g., CCDs, which gather the light through a large lens that is focused directly onto the array. Charge is generated and collected in each solid state element until the CCD is read. Then the charge in each CCD element is read out through the same path with the same charge amplifier and digitized. This charge generation is both linear and temporally stable in the extreme. CCDs are extremely sensitive, and form the basis of most modern X-ray cameras. Commercially available CCDs have true dynamic ranges from 256 to 65,000. In certain special conditions, CCD cameras can provide a dynamic range of over 1,000,000, but it is unlikely that such a range would be necessary or useful.

The camera's dynamic range is a matter of prime importance in selecting the X-ray detection system. Dynamic range is simply the reciprocal product of (1) the attenuation of the X-ray signal as seen on the detector and (2) the fractional accuracy of the signal that needs to be measured by the HR3DCT process. If the attenuation is small, say a factor of 10-100, and the signal should be determined to an accuracy of 2% to 5% (as is typical), then the dynamic

range of the scene is 200-2000 if the 5% figure is used, and 500-5000 if the 2% figure is used.

The lower factors are easily within the range of virtually all commercially available CCD cameras (even the type that are used in consumer video cameras), while the 5000 factor is just barely out of the 12-bit camera, which can be procured for a few thousand dollars. The 16-bit cameras are somewhat more expensive, but even the most expensive CCD camera systems fall under the \$40K range, including some of the most sophisticated camera control and image processing hardware and software that has ever been available.

### 8.2.3 The motion system and position encoding system

At a minimum, the motion control system turns the test specimen about an axis. A position encoding system monitors that motion. Depending upon the usage, the motion control system may be free-running, or controlled separately in individual steps. The position encoding system may be used simply to monitor position, or it may be used in a feedback loop to help control the motion system. In the ideal system, the motion system is controlled, and the position verified automatically from the motion control system, which is ideally tied into the data acquisition system.

We recommend that a modern standard quality turntable be utilized whenever possible although an existing system may be useable if it is (or can be made to be) controllable to required accuracy. Azimuth must be controllable to within at worst one half the view indexing increment. Radial runouts in new equipment are typically specified at 0.003 inch (which would be the maximum error), but are usually within 0.0015 inch of nominal. Even old turntables have radial runouts of 0.003 inch. This is within the spatial resolution tolerance of approximately  $1/3 \times 0.010$  inch (typical<sup>25</sup> best case combined geometric unsharpness of focal spot and detector spatial resolution) necessary for unartifactual reconstruction. Modern turntables are relatively inexpensive (compared with the cost of the rest of the system and/or the labor required to assemble and test a table made from truly inexpensive components), and position feedback controls are very sophisticated.

The rotary mechanism should be arranged with its axis vertical, so that test specimens can be placed on the table, and the specimen rotated. With the specimen held in this fashion, there is no change in gravitational force on the specimen as it rotates. We note that while in principle, the rotary motion could actually be provided along a horizontal access, e.g., a large lathe mechanism, this is generally not recommended except for the stiffest of test specimens. Because of the net 2-g change in force over the course of a horizontal rotation, specimen sagging could be a significant problem, as we have verified for the large rocket motors that are held in a horizontal fixture.

### 8.2.4 The data acquisition system

The data acquisition system is intimately tied to the X-ray camera and to the encoder and rotary table motion control system. Typically a PC-based experiment controller sends

---

<sup>25</sup>This does not include experiments with microfocus X-ray sources.

commands such as X-ray exposure start, camera readout, etc., to the camera, and receives and provides storage space for the data that the camera is returning. If a camera does not support in-camera integration, this must be performed by the acquisition system on digitized images. Clearly, the accumulating buffer must provide adequate arithmetic depth. Camera software is frequently pre-packaged with modern cameras, greatly reducing software costs. In addition, the experiment control software must at least monitor the position of the rotator, if not control it. Again, such software is typically provided with motion control equipment, reducing implementation costs.

#### 8.2.5 The reconstruction and display

Reconstruction and display may be performed off-line, in the sense that these tasks are not driven by the acquisition. These tasks may also be overlapped with acquisition tasks, reducing the overall inspection time.

Reconstruction is typically accomplished on a workstation, e.g., a DEC alpha station, or a Silicon Graphics unit, or a Sun system. These systems have the capacity to process the data without resorting to specialized hardwired processors. Times for reconstruction can vary from minutes to hours -- but recall that this is accomplished for multiple slices worth of data simultaneously.

Another advantage of such engineering workstations is the ability to utilize graphical programming environments in reconstructing and analyzing data. It becomes a matter of simply connecting lines into and out of a new module so that a new function can be applied to the data. Whenever a new test specimen is inspected, the ability to respond quickly with such modular applications of specific functions, saves much time in obtaining optimized reconstructions.

### 8.3 Application optimization

The elements discussed in the previous section must be combined into a functioning system. This task entails decisions that can have significant effects on the cost to inspect and the quality of the inspection. Some of these decisions are complex. This section provides guidance for making these decisions.

The almost-universal goal in system optimization is to minimize inspection cost while maximizing quality. Key cost and quality parameters include time to inspect, reconstruction noise, resolution, scatter, and anomalies. These cost and quality parameters -- performance parameters -- are manipulated indirectly by adjusting the various tunable parameters appearing in the left column of Table 12. As shown in the table, most tunable parameters affect multiple performance parameters, so that improvement is made in one performance parameter only at the expense of another. Hence, as stated, optimization can be complex. The table provides a concise summary of these relationships. The ensuing paragraphs supply insight gathered through experience, as well as more detailed description of some of the issues involved in optimization. For purposes of these discussions, we have assumed that assumptions discussed in Section 8 are valid.

**Table 12**

**Relationships among tunable parameters and performance characteristics.**

The Effect of Increase columns show the numeric effects resulting on a numeric increase of the Tunable Parameter in the leftmost column. Wide arrows indicate stronger effects. The Effect of Increase column headings are Noise (N), Time (T), Resolution (R), Scatter (S), and Artifacts (A).

| Main Affected             |                        |   | Effect of Increase |    |    |    |    |
|---------------------------|------------------------|---|--------------------|----|----|----|----|
| Tunable Parameter         | Performance Parameters | Effect/Comments   | N                  | T  | R  | S  | A  |
| Source energy             | Noise (time)           | Increase of energy below optimum results in more penetration and therefore more flux, which reduces statistical noise.                              | ↓                  | ↓  | -  | -  | -  |
|                           | Noise (time)           | Increase of energy <i>in excess of optimum</i> typically decreases contrast among differing densities, increasing the relative effect of noise.     | ↑                  | ↑  | -  | -  | -  |
| X-ray focal spot diameter | Resolution             | Geometric unsharpness (one of the limitations to radial resolution) is directly proportional to focal spot diameter                                 | ↓                  | ↓  | ↓↓ | -  | -  |
|                           | Noise (time)           | Noise is inversely proportional to focal spot diameter  |                    |    |    |    |    |
| X-ray source flux         | Noise (time)           | Noise is inversely proportional to the square root of flux  | ↓                  | ↓  | -  | -  | -  |
| Flattening                | Noise (time)           | Interposing a flattener reduces projection's dynamic range, enabling the use of more flux and/or greater exposure, and hence less statistical noise | ↓↓                 | ↓↓ | -  | ↓↓ | ↑  |
|                           | Artifacts              | Imperfectly compensated flattening results in difficult constant-radius reconstruction artifacts  |                    |    |    |    |    |
|                           | Scatter                | Adding flattening greatly reduces X-rays that otherwise bypass the subject and scatter off the detector into the camera                             |                    |    |    |    |    |
| SOD (SDD constant)        | Resolution             | Increasing the SOD simultaneously decreases magnification at the detector, and geometric unsharpness  | -                  | -  | ↓  | ↑↑ | -  |
|                           | Scatter                | Since scatter reaching the screen (or the CCD) varies as the square of SDD-SOD, increasing the SOD greatly increases the scatter                    |                    |    |    |    |    |
| SDD (SOD/SDD constant)    | Noise (time)           | Noise is proportional to the SDD  | ↑↑                 | ↑↑ | -  | -  | ↓↓ |
|                           | Artifacts              | Axial cone-beam reconstruction artifacts associated with a too-short SDD can be eliminated by increasing the SDD                                    |                    |    |    |    |    |
| Collimation               | Scatter                | Source collimation is a very important way to reduce the amount of scattered radiation reaching the detector  | ↓↓                 | ↓↓ | -  | ↓↓ | -  |

|   |              |  |   |         |
|---|--------------|--|---|---------|
| screen; collimation has no negative side effect         |              |  |   |         |
| Shielding   | Scatter      | Detector shielding and filtering have little effect on detected scatter (especially at high energies)                                | ↓ | - - - - |
| View size<br>(total pixels<br>constant)                 | Noise (time) | Noise is inversely proportional to the detector dimension  | ↓ | ↓ ↑ - - |
|   | Resolution   | Resolution is proportional to view size  |   |         |
| Exposure<br>per scan                                    | Noise (time) | Noise is inversely related to the square root of the exposure time   | ↓ | ↑ - - - |
| Views per<br>scan<br>(exposure<br>per scan<br>constant) | Artifacts    | Some artifacts types are reduced by increasing the number of views (this can increase acquisition and reconstruction times)          | ↓ | ↑ - - ↓ |
| Camera gain   | Noise        | It is important to match the numeric range to the signal range to minimize quantization noise, especially in wide dynamic range data | ? | ? - - - |
| Reconstruct<br>resolution                               | Noise        | Reconstruction noise can be improved (at the expense of resolution) by low-pass filtering each view prior to backprojection.         | ↓ | ↓ ↑ - - |

### 8.3.1 Sufficient X-ray flux

Adequate X-ray flux is taken in two senses. The first is that for any single rotational position of the test specimen, the total number of X-rays being transmitted and interacting in the detector is statistically sufficient for the measurement to be made. Because most experimental configurations try to use the lowest possible energy, this implies that the source-to-detector distance be minimized.

The second sense of sufficient X-ray flux is in the total number of photons to be counted over all views in a scan, the total flux. Obtaining the requisite flux can be achieved by two overall methods: (1) counting longer at each view, either by integrating at each position, or taking multiple data sets at the same position, and adding the digitized signals, or (2) taking more views at intermediate angles between the required minimum adjacent views points. In general, the second approach is better, because it smooths the data. (One of the broad problems of reconstructive imaging is insufficient sampling of the test specimen, and the algorithms that are used to overcome sampling that is less than perfect. Virtually all reconstructive schemes involve some compromise in sampling density. The more samples acquired and the more densely sampled the test specimen is, the smoother the reconstructed image will appear.)

### 8.3.2 Scatter

If scattering dominates the situation, two choices mitigate its effects: The first is in choosing the source-object distance, consistent with appropriate coverage and an acceptable level of X-



ray flux at the detector. The best position for the test specimen is halfway between the source and detector. The second is in choosing the source-detector distance. The best distance is, "as large as possible" consistent with the acceptable X-ray flux levels.

For most inspection situations, where dynamic range intrinsic to the scene and to the detection level is not greater than 1:100 or 1:1000, and where the camera can accommodate these differences, scatter is not usually an issue, except for the usual considerations of X-ray imaging. However, when the dynamic range requirements become more severe, and the dynamic range approaches the 1:10,000 level or greater, significant care must be taken in analyzing the image. In particular, assuming that all instrumental changes that can be made have been made (e.g., utilizing a particularly thin conversion screen, maximizing distances, using appropriate anti-reflective coating optics), we may be forced to turn to the use of a field flattener. If the field flattener profile is steep and has effects that extend to the positions of significant radial features on the screen, and the dynamic range that must be removed is high, this is unlikely to result in a good image. The reason is that the subtraction and convolution of the field flattener data present their own set of artifacts that can overwhelm the features inherent in the image. Moreover, the slightest error in the adjustment of the received flux for the field flattener can cause a major misstatement in the signal of a feature that is at the low-point of the dynamic range (e.g., just inside the tangent).

Utilizing a field flattener requires that a series of calibration measurements be made. They are: (1) open field, (2) open field with flattener, (3) test specimen without flattener for overlapping region, (4) test specimen with flattener. In particular, the effects of the flattener(3) on the overlapping region where the dynamic range does not exceed that of the detector (4) must be compared to be certain that the flattener is not becoming a significant scatter source in and of itself. (It usually is.)

### 8.3.3 Coverage of the test specimen

Coverage of the test specimen will be required to some depth within the object. For a given X-ray source and detector, the coverage of the test specimen deepens as the ratio SDD/SOD approaches unity. In most cases, the spatial resolution improves, because it is usually the detector that has a smaller effective spatial resolution element. The downside of this arrangement is the increase in scatter (the optimum scatter reduction point places the test specimen halfway between the source and detector, a magnification of two on the detector).

For the standard arrangement, with the edge of the areal detector just overlapping the edge of the outside tangent beam, the coverage extends from the outside edge of the test specimen to the inner tangent point of the ray that strikes the in-board-most point of the detector. There will be a radial dependence on the degree of coverage within this zone, which is discussed below in the contrast section.

Axial coverage is largely a function of how many degrees off the central plane can the views be, and still conform with certain approximations in standard cone-beam reconstruction algorithms. For conservative rules-of-thumb purposes, five or six degrees on either side of the central plane should suffice.



#### 8.3.4 Spatial resolution and contrast of the resulting image

Spatial resolution is determined by a combination of the sampling frequency, the point spread function (see below), and details of the reconstruction scheme, including the reconstruction grid and the algorithm. The big difference from conventional CT is in the sparse coverage in the circumferential direction compared to the dense coverage in the radial direction. This lopsided distribution in sampling translates into radically different spatial resolutions in the different directions: radial, azimuthal, axial. For HR3DCT, the most critical spatial resolution is in the radial direction. We give up good spatial resolution in the azimuthal direction to pay for this radial resolution. *Radial spatial resolution is determined by conventional rules for line sampling with contiguous detectors.* The axial spatial resolution can actually be determined on a basis as fine as the radial spatial resolution, as long as there is sufficient X-ray flux in a reasonable time (defined by program requirements) for data acquisition. Circumferential spatial resolution is determined by the density of the views, and the smoothing algorithms that make the image appear as an image. The view density can be worked out according to conventional geometric principles, as a function of both the density of views and the radial resolution.

Clearly, the point on the test specimen that is closest to the edge receives the most coverage, since it appears in a number of views as the specimen rotates. By comparison, the inner tangent point is sampled only once as it just brushes by the extreme innermost detection element. Thus, for a uniform density test specimen, the statistics associated with the outside edge will always be better than those at the inside edge of coverage. Correspondingly, the contrast at the outside edge of the test specimen will be best. For a uniform test specimen, the contrast will decline as a function of decreasing radius within the test specimen. With a more absorbing (i.e., a higher mass absorption) outer layer, the statistical dependence of the contrast as a function of radius is much more complex, and almost needs to be determined experimentally. Details of performance and quantitative predictions are discussed in section 6.4, Projecting Performance.

We also discovered that the limiting contrast for our particular algorithm was approximately three percent. No matter how much data that we acquired, the limit seemed to be at this level. Perhaps with more refinement of the algorithm we could do better. We also note that three percent noise in a reconstructed image would easily allow the detection and identification of cracks and unbonds that are a small fraction of the spatial resolution element size.

#### 8.3.5 Data Acquisition time

Data acquisition time for HR3DCT follows the same rules as conventional CT and all other forms of two-dimensional reconstructive imaging. The main rule governing the relationship between spatial resolution, contrast, and data acquisition time is:

$$(\text{Contrast})^2 (\text{time}) / (\text{spatial resolution}) = \text{constant}$$

This relationship differs from the standard one in that we assume that we acquire data across the entire face of the RTR unit. Thus, as the spatial resolution figure becomes smaller, we

have a correspondingly larger number of elements in the data acquisition scheme. The effect of changes in both axial and circumferential spatial resolution will follow in the same way.

We also note that the axial extent of any cone-beam data acquisition sequence and also changes the nature of the data acquisition time per "conventional" CT slice.

In judging total time, the quality engineer is cautioned to include the times associated with loading/unloading the test specimen, and other overhead tasks.

### 8.3.6 The point spread function and its implications

The point spread function, PSF, of the system summarizes all the instrumental, geometric & configurational, and X-ray production and interaction effects. (The following discussion also applies to the modulation transfer function, MTF, which can be mathematically derived from the PSF and vice versa.) One way of looking of the PSF is literally as what happens to the image of a point. It is spread out across the imaging plane because the X-ray source has a finite size, the detector has a finite size, because X-rays can scatter within the detector interaction volume and produce light that is imaged in regions away from the interaction site, because the visible light itself is scattered before it leaves the interaction volume. All of these effects contribute to spreading the flux from its ideal image point into a larger region. The PSF can be determined by a number of techniques, including the edge response test to a stack of high-Z material, and other such textbook approaches. (See also *Numerical Recipes*, by Wm. Press et al., for an excellent discussion of how to do this mathematically.)

The ideal PSF is as a delta function -- which would mean no degradation of the imaging scene. All real-world and instrumental effects work to degrade that delta function into something less satisfying. In particular, the distribution becomes wider and can develop "wings" that extend very far from the original point. For most ordinary imaging purposes, this is not significant, but for many HR3DCT applications, the change in dynamic range over the scan region of interest can render a higher intensity signal's (from a region adjacent to the lower intensity signal's region) swamping the lower intensity signal, because of this effect of the "wings." This was true, for instance, in our reconstruction of the Titan 19 mm steel skin phantom. We had to resort to a field flattener, as discussed below, but we could not overcome the intrinsic wings in the distribution. The wings in a PSF can also spoil the intrinsic contrast in a low-intensity region, even if the imaging is well-understood.

## 8.4 Projecting performance

Performance can usually be estimated at a level that is adequate to decide whether a particular test specimen can be successfully scanned utilizing a HR3DCT approach. In some special cases, e.g., where MTF considerations dominate at the edge of a thick steel skinned rocket motor, one really needs to perform the experiment. In such instances (e.g., tremendous density discontinuities or very sharp gradients), local conditions overwhelm the overall gross performance numbers.

The basic performance characteristics of interest are only three: time for data acquisition, spatial resolution and contrast sensitivity, sometimes called CT contrast, or simply "contrast." In addition, artifacts play a key role in deciding the sensitivity of the system to certain types

of anomalies. We *choose* the spatial resolution based on initial considerations of the inspection problem, as demonstrated in earlier subsections of this section, and in Section 8. This spatial resolution is achieved by the combination of focal spot size, detector spatial resolution and geometry. It is then a matter of how long data must be acquired in order to reach a given level of contrast. (Of course, this assumes that the level of contrast can be achieved, i.e., that no intrinsic limits exist in the algorithm or in other systematic errors [e.g., artifacts]. Every algorithm, every system, and every measurement have systematic errors, which produce such limits. The idea is to keep these limits below the significance level for anomalies of worry.)

The overall approach presented here is to estimate the number of separate spatial resolution elements (NOT picture elements) in the reconstruction, apply conventional rules of cone-beam CT, and then de-rate the performance prediction on the basis of previous experience with this particular set of reconstruction algorithms. The experience factor is crucial, because different algorithms perform differently. For instance, algorithms that emphasize the high spatial frequency nature of the region near interfaces will provide better spatial resolution at the expense of contrast resolution. Our approach is completely heuristic in its application. The quality engineer who observes this procedure is likely to get proper answers. A more proper intellectual approach actually reconstructs dummy data and measures the contrast as a function of statistically generated noise on the inputs. However, it is our practical experience that real-world deviations from the ideal render the heuristic experimental data fit a better approach.

We project *average* performance for a conventional, cylindrically symmetric, uniform density specimen. Further assumptions include complete coverage (i.e., a full 360 degrees), an exterior annulus of reconstruction that is much smaller than the radius.

The number of spatial resolution elements in the image is given by the formula, below, where  $t$  is the width of the annulus,  $dr$  is the radial spatial resolution,  $R$  is the radius of the cylindrical system, and  $A$  is the ratio of circumferential spatial resolution to radial spatial resolution:

$$\frac{t}{dr} \frac{2\pi R}{A dr} = \frac{2\pi R t}{A dr^2}$$

The minimum number of rays per view,  $M$ , is equal to the number of resolution elements across the annulus:  $(t/dr)$ . The minimum number of views,  $N$ , is determined by the projection of the circumferential spatial resolution ( $A dr$ ), as a point on the test specimen rotates from one radial detection element to the next. At a nominal minimum,  $M$  is defined by the following equation (but could be larger).

$$M = \frac{1}{dr} \sqrt{\frac{8Rt}{A}}$$

The minimum noise-to-signal ratio,  $\sigma_{data}$ , in the absorption data can be defined in terms of the minimum acceptable noise-to-signal in the image data,  $\sigma_{image}$  as shown below.

$$\sigma_{data} \cong \sigma \mu L \sqrt{\frac{dr}{t}} \sigma_{image}$$

where  $\mu$  is the volume absorption coefficient and  $L$  is the typical absorption length through the specimen.

The minimum number of unattenuated photons per single unit measurement then  $N_0$ :

$$N_0 = \sigma_{data}^{-2} e^{\mu L}$$

The important point is that we define the flux necessary to achieve the required contrast at that spatial resolution for the test specimen. This analysis does not take into account systematic errors and artifacts that are peculiar to the configuration of the test specimen. We show some examples in Section 9.

## 9. CONCEPTUAL DESIGN EXAMPLES

In this section we apply the broad principles of Section 7.1 to a few specific application problems. Our objective is twofold. First, it is to show how a real problem might be addressed by HR3DCT, and second, it is to examine the cost-effectiveness of such an application.

We will present three examples of HR3DCT conceptual designs, each aimed at a different application, so that some of these issues that may be ancillary to the principles of HR3DCT, but practically important, are shown. The examples are: (1) a generic HR3DCT system, which is to be utilized for rocket motor nozzles approximately 45 to 75 cm in diameter, (2) a dedicated HR3DCT system for examining a 30-cm diameter hollow-core composite aerospace structural component that is wound about a steel mandrel, and a (3) a very seldom used HR3DCT system that is meant to inspect a very large solid rocket motor. Issues that are common to the three examples are discussed once, under the first example.

### 9.1 The generic HR3DCT system

This system is to be utilized in production NDE of a variety of objects, but most importantly for rocket motor nozzles approximately 0.50- to 0.75-m in diameter. The manufacturer has no specific rocket motor system that will solely benefit, but wants to spread the benefits and costs over a number of different propulsion programs. Typical materials are carbon and silicon phenolics; carbon-carbon throats; flex seals; some aluminum and titanium rings; greases, oils, and gels for fillable rubber boots. Typical absorption at 4 MeV ranges from 80% to 99% over the family of different chords and materials in the various nozzle programs.

#### 9.1.1 Requirements

The requirements for the generic hr3dct system are summarized in Table 13.

**Table 13**  
**Generic HR3DCT system requirements..**

| Aspect                  | Requirement  |
|-------------------------|--|
| Test specimen           | Nozzles 18-30 inches (45-75cm) in diameter   |
| Test specimen materials | Mostly carbon, silicon phenolics, carbon-carbon throats, flex seals, some aluminum and titanium rings; greases, oils, and gels for fillable rubber boots |
| Absorption              | Typically 80-99% at 4 MV.  |
| Anomaly sensitivity     | 10 mm x 10 mm x 0.1 mm (0.040 inch) detectability  |

While no hard requirements exist, the generic requirement is simple: Circumferentially-oriented 0.1-mm unbonds and delaminations of size 10 mm by 10 mm must be detected. For HR3DCT, this translates into a radial spatial resolution element size of 0.4 mm with a contrast of 0.05. This will yield a statistical four standard deviations above background for a feature that passes completely through the resolution element. We note that 0.4-mm spatial

resolution is usually achievable for most X-ray source/detector systems (whose typical limit is 0.2 mm).

For a HR3DCT element of size 0.4 mm by 5 mm by 2.5 mm (radial, circumferential, axial), unbonds would be clearly visible at this level, if the inspector were looking directly at the feature. A feature of size 10 by 10 mm, would be easily detectable because it extends through at least 8 resolution elements. If it straddles a boundary exactly, the feature would appear as a  $2\sigma$  variation through 16 contiguous pixels – also clearly detectable. The only other considerations are the artifact level and the density differences on either side of the interface that we should be sensitive to. If the density differences are extreme, e.g., a factor of three in density, then the appearance of the interface itself becomes crucial, because there will be a tendency for an unbond to appear as simply a slightly thinner amount of the denser material. In these cases, looking for differences in the radial profiles as a function of azimuthal position usually helps. The usual cautions about artifacts and pixelization apply.

#### 9.1.2 The X-ray source

The X-ray source of choice is a 4 MeV Linatron. A 2 MeV system will perform adequately, as would higher energy linac-based systems, but 4 MeV appears best for this application. Energies below 1 MeV will not penetrate through any significant interior dimension of 0.75 m diameter nozzle.

We assume an existing facility with appropriate existing X-ray source. The source and the facility, at least at these energies, are the single largest cost item, and the hardest from which to justify a change, especially if a suitable or almost-suitable facility exists. The available facility has a 4 MeV Linac-based X-ray source. A quick check reveals that a half-value layer at 4 MV in phenolics ranges between 125 and 150 mm. Titanium and aluminum have HVL's of 48 and 70 mm, respectively. Carbon-carbon's HVL is approximately 100 mm. Thus, the worst of the non-metals presents a direct chord of about 7 HVL, which corresponds to a transmission of 0.8%, if the nozzle were solid and made of carbon-carbon. The more likely situation is that the carbon-carbon is only in the throat, and that the worst case path through the carbon-carbon is 3 to 4 HVL. Thus, absorption for the non-metallic sections is probably on the order of no more than 90% to 95% – a perfect setting for radiographic measurements at 4 MeV. (A 450 kV source would not have done the job easily, requiring 15 HVL, by comparison.) The metal rings are very narrow, and the worst case path length through the inside tangent on the rings is usually less than 150 to 175 mm, which corresponds to 3 HVL. This plus the likely nozzle transmission of 2 to 3 HVL of phenolic and other material leads to a total of 5 to 6 HVL, a very comfortable absorption of 98 to 99%. For most purposes, the transmission will be on the order of 95% absorbed within the nozzle. Thus, a 4 MeV Linac source is an excellent choice.

#### 9.1.3 Imaging

The test specimen anomaly sensitivity implies a maximum spatial resolution element size of 0.2 mm. Utilizing a standard 2 mm x 2 mm spot size available on the 4 MeV Linatron yields the test specimen's being placed relatively close to the detector. In fact, the optimum position yields the ratio of source-object distance/source-detector distance = 0.9.

The detector is a standard CCD-based thin-screened GOS or equivalent system, providing the necessary 2.5 lp/mm resolution so as to be capable of imaging the scene at the 0.2 mm spatial resolution element level as seen at the test specimen.

The X-ray camera that is associated with our hypothetical 4 MeV facility is typically one where the screen is somewhat thicker (in order to achieve sufficient stopping power for the X-rays) than what an excellent spatial resolution would allow. The downside of this arrangement is the relatively poor spatial resolution that we must tolerate. Given that there will be plenty of flux — i.e., the transmission is not too low — the arrangement with the thinner screen is usually better.

The nominal spot size of the source is 2 mm by 2 mm. The spatial resolution on the screen is about 2.5 lp/mm, leading to a spatial resolution element size of approximately 0.2 mm. To a first approximation, the Rayleigh criterion or any other similar single parameter measure of spatial resolution will suffice. A more rigorous analysis would include a complete modulation transfer function definition and its projection at the edge of the test specimen.

In any case, the geometric unsharpness criterion for this system leads us to a geometry where the center of rotation of the specimen is much closer to the screen than to the source. In fact, a 0.4-mm spatial resolution element requirement places the test specimen 90% of the distance to the screen from the source. Had we been able to proceed with a smaller spot size, this would not have been so extreme a position. In particular, the scattering ramifications will have to be investigated on an individual specimen type-by-type basis.

#### 9.1.4 Positioning issues

We consider two types of position error: The first type involves the position of the specimen on the rotator (probably a turntable). The second type involves deviations of the mechanical moving apparatus from a perfect rotational motion. In both cases, the advantage that the HR3DCT approach provides lies in the slow change in projected position of the features of interest.

The first type is generally considered benign to the extent that the rotation is not that of a perfectly circular object, but more akin to that of an off-center phonograph record. This problem can be viewed as a tracking issue where the position of the specimen floats from frame to frame. Since HR3DCT marks the outside edge of the specimen very well, we can easily track this position from frame to frame. The test specimen and its associated features are “anchored” to the edge; thus, simply by adding the vectors representing the relative position of the features to the position of the edge, we can in principle obtain an accurate position for the features. Moreover, because of the way that HR3DCT works, the errors at the edge are not cumulative (as that they would be in conventional CT).

Deviations of the second type are part of the mechanical tolerance budget. These have been covered in the literature of conventional CT, but we mention them here for completeness and for a property that is unique to HR3DCT. In conventional CT, the tolerance build-up is such that radial and axial runouts of rotating mechanisms are severe, and can enter the tolerance build-up linearly. In HR3DCT, the nature of bearing runouts is such that they do not change rapidly in the *projected view*: The runouts change the circumferential scene significantly --



but not the tangential view. Thus, the actual mechanical tolerances for most rotators are less stringent than for conventional CT operating at similar levels of spatial resolution.

#### 9.1.5 Data acquisition

Data acquisition must permit sufficient number of samples per view, and sufficient number and density of views for given spatial resolutions. This is defined in precisely the same manner as in Section 7.1. For the case here, we require about 2000 views, with about 500 samples per view. Section 9.1.7, which discusses performance estimates, discusses this point.

#### 9.1.6 Data reconstruction and analysis

Data reconstruction, for the generic HR3DCT system, will require flexibility similar to that which exists in the breadboard system. While such flexibility enables the system to respond conveniently to a large variety of acquisition and reconstruction geometries, it also imposes an execution speed cost. This could be mitigated in part by special-coding certain time-efficient reconstruction cases. For example, in the event where axial resolution is less important (or when radiographic geometry permits) a parallel-fan version of HR3DCT could greatly accelerate volume reconstruction. A faster machine with more memory could also greatly speed up reconstruction processing.

The analysis, at least at the topmost level, analyzes three parameters: spatial resolution, contrast, and artifacts. At the secondary level, the analysis will involve the appearance of interfaces, the time required to see an anomaly of particular character at a particular location on the test specimen, and the algorithms that need to be developed to search for that particular type of anomaly.

We mention artifacts of the false radial gradient density profile (e.g., overshoot or undershoot variety) near interfaces and boundaries as being among the most difficult to overcome. These artifacts can mask the nature of the boundary. However, signature comparison and modeling work well in lowering the size of the unbond detection limit.

In measuring performance, one must be very careful to account for such artifacts. Thus, the contrast measurement must not be taken over an area where such a false radial density profile occurs. Rather, the contrast should be measured in thin strips that are parallel to the outside edge of the motor. In our experiments with HR3DCT, our contrast limit was about 3%.

#### 9.1.7 Performance predictions and parameters

**Table 14**  
**Generic HR3DCT system performance parameters**

|                       |   |
|-----------------------|---|
| Number of views       | 600-3000, depending upon diameter, spatial resolution, and coverage |
| Data acquisition time | 1-10 seconds per view   |
| Readout times         | Low dynamic range scenes (12-bit digitization) ~1 sec               |
|                       | High dynamic range scenes (16-bit digitization) ~ 10 sec            |



|                             |   |
|-----------------------------|---|
| Rotation mode               | Continuous or in steps; rotation time within 0.5 - 3 seconds per view   |
| Total time per view         | 1.5 -13 second per view   |
| Readout time <sup>26</sup>  | 0.5-1.0 sec   |
| Total time per view         | 2-13 seconds  |
| Total time on rotating data | = number of views x total time per view<br>= 600 x 2 = 1200 second, (small nozzles)<br>= (1800-3000) x (10-13) = 18000-39000 sec (large nozzles)<br>= 5-12 hr / 6-10 inches in axial coverage |

### 9.1.8 Cost

We have assumed that a 4 MeV Linac source and facility are available. In addition, the rotator is an existing piece of equipment. (Typical costs for such an X-ray source might be \$1/2 million, and another \$1-2 million for the facility. The rotator can range from \$25K to \$100K, depending upon weights and accuracies.) In addition, we have assumed that the HR3DCT algorithms are available and can be utilized with little customization. Moreover, we assume that the labor skills are not being developed on this job, but that the crew already has professional experience in assembling and integrating a HR3DCT system

The cost for this system includes the following items:

|  |           |
|--|-----------|
| camera (including CCD, control card, software, etc.) | \$40K     |
| remainder of X-ray box                               | 40K       |
| encoder and control                                  | 5K        |
| experiment control computer + software               | 5K        |
| workstation  | 30K       |
| <u>miscellaneous shielding, etc.</u>                 | <u>5K</u> |
| total hardware                                       | \$125K    |

<sup>26</sup>This analysis assumes that the data acquisition for frame j occurs simultaneously with the readout for frame (j-1). Thus, readout time as discussed here means the additional time required beyond the data readout that has occurred in parallel with previous activity, i.e., readout time that contributes to the critical path.

Include miscellaneous labor for initial set-up and run ~ 10 man-weeks.

## 9.2 A dedicated HR3DCT system for a 12" diameter sample

This section discusses a *dedicated* HR3DCT for examining a 30 cm diameter hollow-core composite aerospace structural component that is wound about a steel mandrel. Our approach is similar to that of Section 9.1. However, in this section we will only present the results, and discuss deviations from the previous example.

This sample is much smaller and generally less absorbing than the previous one. *The important point: for HR3DCT, the steel mandrel need not be penetrated.* In fact, we discover that a 420 kV source will easily accomplish the task, and a 300 kV source will probably do so. These X-ray sources are much preferred to the Linac-based sources because they are far cheaper, the facility requires much less shielding, and the spot size can be made very small. In the case of one X-ray tube, 0.3- to 0.5-mm spot size is possible. While this tube produces far less flux, the source and detector can be placed much closer together, closer to the specimen, and a much greater X-ray flux is possible.

The imager of choice is a standard 640 by 480 CCD-based optical imaging system that is at one conjugate focus of a large lens. The other conjugate focus is on the X-ray scintillation screen. While we could use a larger number of pixels on the CCD, the number of pixels is not justified by requirements. In addition, considerable hardware and software already exists and is already configured for this standard CCD arrangement.

The motion system is one where the component must be held at the ends of the long banana-shaped mandrel. The best way to do this with an adjustable offset holding mechanism for the component. In this way, the local region of examination can always be held so that the center of rotation is approximately coincident with the center of the mandrel.

The standard unbond anomaly size is 7.5 mm by 7.5 mm by 0.05 mm. The great advantage to this system is that the unbonds occur within laminates of the same material -- there is no density difference across any of the laminates where such an unbond might occur. This translates to 3% contrast, 0.4-mm spatial resolution element sizes, 2.5-mm axial resolution, and 2.5-mm to 5.0-mm azimuthal resolution element sizes. The nominal worst-case transmission varies from 0.8% with the 300 kV source to 1.4% with the 420 kV source. Thus, both sources are possible. We calculate that 10 seconds dwell time per view is necessary and that 600 views are necessary. Utilizing a small rotational time overhead leads to approximately two hours of time on the table with the 300 kV source, which will yield 150 mm of axial extent per scan. By applying the rules of Section 7.1, we find that a current of approximately 500 microamps will supply the X-ray photon flux necessary for this contrast level.

The cost estimate is as follows:

|  |            |
|--|------------|
| 300 kV source                                | \$75K      |
| deep dynamic range CCD + X-ray det.          | \$80K      |
| experiment control computer + software       | \$ 5K      |
| workstation for reconstruction/display       | \$30K      |
| motion system (Rotator + encoders)           | 100K       |
| <u>miscellaneous fixturing, shielding</u>    | <u>10K</u> |
| Total:                                       | ~\$300K    |
| + 12-15 man-weeks in set-up and integration. |            |

### 9.3 A seldom used HR3DCT system for inspecting a very large solid rocket motor.

The class of rocket motors to be inspected is the 10-foot diameter class and larger, similar to Titan and Space Shuttle Boosters and other heavy launch capacity motors. For such cases, there is almost always a 15 MeV generator available at the initial site of manufacture. Most such facilities utilize either film for sporadic or sparse checking and an RTR-based system for more common bondline inspections in accessible areas.

For composite case motors, the standard treatment with the largest available source, 15 MeV Linac-based source, is straight-forward. The desirable type of camera is a wide dynamic range CCD camera that can be chilled for long-term integration if necessary. On the other hand, as our earlier images indicate, an Isocon camera (or other analog imager) can provide good information at relatively low dynamic range on large scale anomalies.

The rotator is typically the motion system that is already in place. Usually, such systems do not provide sufficient rotator angle information. Moreover, a number of such systems maintain the rocket motor in a horizontal orientation. Thus, as the rocket motor turns, it is subject to a net change of 2 g's of force as it turns through 360 degrees. With conventional CT, such an arrangement can produce a disaster because the scene changes over the course of the scan. (This is one reason that, given a choice, CT system designers almost always choose a vertical spin axis.) However, for HR3DCT, with only a limited view, we can usually arrange the camera and source so that the narrow fan shoots in a horizontal direction, not a vertical one. Thus, the scene presented does not encounter the tremendous variation in net force as the rocket motor rotates. Typically the net change in force on that part of the motor is 0.1-0.2 g. In addition, because HR3DCT employs an edge-following space-location approach, any "jelly-rolling" or "hot-dogging" (slumps caused by the net g-forces) is mitigated. For most existing large-object rotators, either a better encoder should be added, or if the usage is *very* seldom, then the rotator position can be manually set for each exposure of the camera, or an optical set of fiducials employed and the rotator set remotely. Any number of such gerry-rigged rotator positioning solutions are possible for the one-time-only usage.

For metal-skinned rocket motors, as we have seen, the thick skinned specimens are very difficult to inspect. Our data were taken perpendicular to the axis of the rocket motor. We were defeated by a combination of insufficient camera dynamic range — which forced us to use a field flattener — and the resulting scattering that dominated the reconstruction. Most of these thick skinned regions are located close to the end of a section or near a dome. Had we taken our data at an angle that presents more skew to the beam, part of the attenuation might have been avoided, if that part of the data had been sampled at such a skewed angle. While the reconstruction algorithm tends to present more artifacts as we depart from the conventional CT plane, it is typically not till we reach 8-10 degrees off the plane that such effects truly interfere with our reconstructions.

Typical data acquisition times are 15-40 hours for 15 cm of axial dimension on 13-mm thick metal-skinned rocket motors. This allows detection to the 0.08-mm unbond extending approximately a few square centimeters. If we allow for larger unbonds, these times should decrease substantially. Times for composite case motors are lower.

The costs<sup>27</sup> for such a system include the following:

|  |              |
|--|--------------|
| deep dynamic range CCD + X-ray det.          | \$80K        |
| experiment control computer + software       | \$ 5K        |
| workstation for reconstruction/display       | \$30K        |
| motion system (encoders, etc)                | \$30K        |
| <u>miscellaneous fixturing, shielding</u>    | <u>\$10K</u> |
| Total:                                       | ~\$155K      |
| + 12-15 man-weeks in set-up and integration. |              |

---

<sup>27</sup>We assume that the rotator, the X-ray source, and the facility already exist.